

# **Subwavelength hole arrays, surface plasmons and quantum entanglement**

## **PROEFSCHRIFT**

ter verkrijging van  
de graad van Doctor aan de Universiteit Leiden,  
op gezag van de Rector Magnificus Dr. D. D. Breimer,  
hoogleraar in de faculteit der Wiskunde en  
Natuurwetenschappen en die der Geneeskunde,  
volgens besluit van het College voor Promoties  
te verdedigen op 22 september 2005,  
klokke 14.15 uur

door

**Erwin Altewischer**

geboren te Leiden, Nederland  
op 5 april 1975

**Promotiecommissie:**

Promotor:	Prof. dr. J. P. Woerdman	
Copromotor:	Dr. M. P. van Exter	
Referent:	Prof. dr. L. Kuipers	(AMOLF/Universiteit Twente)
Leden:	Dr. E. R. Eliel	
	Prof. dr. G. Nienhuis	
	Prof. dr. M. Orrit	
	Prof. dr. G. W. 't Hooft	(Philips Research/Universiteit Leiden)
	dr. R. J. C. Spreeuw	(Universiteit van Amsterdam)
	Prof. dr. P. H. Kes	

The work reported in this thesis is part of a research programme of 'Stichting voor Fundamenteel Onderzoek der Materie' (FOM) and was supported by the EU programme IST-ATESIT.

“Poets say science takes away from the beauty of the stars - mere globs of gas atoms.  
I, too, can see the stars on a desert night, and feel them. But do I see less or more?”

*Richard Feynman, The Feynman Lectures on Physics, Vol. 1*



---

## Contents

---

<b>1</b>	<b>Introduction</b>	<b>1</b>
1.1	Subwavelength hole arrays . . . . .	1
1.2	Surface Plasmons . . . . .	2
1.3	Quantum Entanglement . . . . .	2
<b>2</b>	<b>Characterization of nanohole arrays in metal films</b>	<b>5</b>
2.1	Production and visual analysis of hole arrays . . . . .	6
2.1.1	Samples made with e-beam lithography . . . . .	6
2.1.2	Samples made with ion-beam milling . . . . .	7
2.2	Optical measurement of the lattice period . . . . .	9
2.3	Spectral measurements . . . . .	10
2.4	Conclusions . . . . .	15
2.A	Hole arrays as diffraction gratings . . . . .	16
<b>3</b>	<b>Spontaneous parametric down conversion as a source of entangled biphotons, in theory and practice</b>	<b>19</b>
3.1	Introduction . . . . .	20
3.2	Theory of SPDC as a biphoton source . . . . .	21
3.2.1	The biphoton wave function . . . . .	21
3.2.2	Phase matching . . . . .	21
3.2.3	The angular distribution of type-II SPDC light . . . . .	22
3.2.4	The entangled state produced in type-II SPDC . . . . .	25
3.2.5	Coincidence detection rate for polarization entanglement . . . . .	25
3.3	The degree of polarization entanglement . . . . .	27
3.3.1	The concurrence and related measures . . . . .	27
3.3.2	Concurrence without walk-off compensation . . . . .	28
3.3.3	Concurrence with walk-off compensation . . . . .	29

## Contents

3.4	Experimental characterization of our SPDC source . . . . .	31
3.4.1	Setup and typical experimental numbers . . . . .	31
3.4.2	Measured count rates . . . . .	33
3.4.3	Measured degree of quantum entanglement . . . . .	35
3.5	Conclusions . . . . .	37
3.A	Phase matching in type-II SPDC . . . . .	37
<b>4</b>	<b>Plasmon-assisted transmission of entangled photons</b>	<b>41</b>
<b>5</b>	<b>Nonreciprocal reflection of a subwavelength hole array</b>	<b>49</b>
<b>6</b>	<b>Polarization analysis of propagating surface plasmons in a subwavelength hole array</b>	<b>55</b>
<b>7</b>	<b>Fano-type interference in the point spread function of nanohole arrays</b>	<b>65</b>
<b>8</b>	<b>Polarization tomography of metallic nanohole arrays</b>	<b>71</b>
<b>9</b>	<b>Analytic model of optical depolarization in square and hexagonal nanohole arrays</b>	<b>77</b>
9.1	Introduction . . . . .	78
9.2	Model . . . . .	79
9.3	Comparison with experiment . . . . .	82
9.4	Model extensions . . . . .	85
9.5	Conclusion . . . . .	87
<b>10</b>	<b>Quantum decoherence versus classical depolarization in nanohole arrays</b>	<b>89</b>
10.1	Introduction . . . . .	90
10.2	Theoretical comparison of classical depolarization and quantum decoherence	90
10.3	Experimental comparison of classical depolarization and quantum decoherence	94
10.4	Conclusions . . . . .	97
10.A	Degree of polarization for nonperfect arrays . . . . .	98
	<b>Bibliography</b>	<b>99</b>
	<b>List of publications</b>	<b>105</b>
	<b>Samenvatting</b>	<b>107</b>
	<b>Curriculum vitæ</b>	<b>111</b>
	<b>Nawoord</b>	<b>113</b>

### 1.1 Subwavelength hole arrays

In 1998, Ebbesen showed that arrays of subwavelength-diameter holes in metal films have extraordinary transmission properties [1]. Their transmission spectrum is strongly peaked, with peak intensities that can be an order of magnitude larger than expected from standard electromagnetic theory for subwavelength apertures, developed by Bethe and adapted by Bouwkamp [2, 3]. A typical transmission spectrum of a square nanohole array is shown in Fig. 1.1, together with the Bethe and Bouwkamp predictions [2, 3]. The extraordinary large peak transmission is commonly explained by resonant excitation of surface plasmons (SPs) on the hole array [1, 4–6]. However, there has been some debate on alternative explanations in the literature: one paper found an anti-correlation between optical transmission peaks and excitation of SPs in 1-D arrays of slits [7], another focussed on the role of phase singularities (optical vortices) [8], a third showed the non-negligible influence of the holes themselves through their shapes [9] and a fourth, coauthor of Ref. [1], in an interesting change of opinion, now advocates a diffracted evanescent wave model [10]. Most of this debate can probably be resolved by admitting that each of the viewpoints is a valid description of some part of the problem, and that SPs, however useful a concept to explain a number of the optical properties of the nanohole arrays, may fall short in other respects. It is interesting to note, that most of the optical properties of nanohole arrays can already be accounted for qualitatively by allowing for a (small) direct transmission through the holes, next to the indirect resonant-SP contribution; This explains, for instance, the typical asymmetric peaks in the hole array spectra, which are similar to Fano resonances occurring in atomic physics [11, 12].

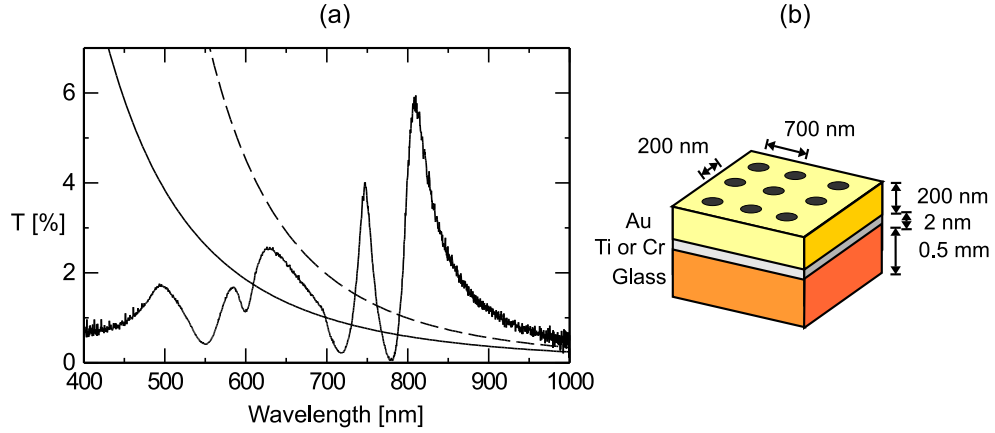


**Figure 1.1:** a) A typical transmission spectrum of a square hole array in gold, for nearly plane-wave illumination at normal incidence. The two smooth curves show the Bethe prediction (solid) and Bouwkamp's corrections thereof (dashed), where both curves are calculated using the hole filling factor for the square array of 0.064. b) A sketch of the investigated square array of holes.

## 1.2 Surface Plasmons

Surface plasmons have been intensively studied since a number of decades already [13]. They are surface charge density waves, with an associated electromagnetic field, propagating along the interface between a dielectric and a metal, see Fig. 1.2. They exist when  $\epsilon_d + \epsilon_m < 0$ , with  $\epsilon_d$  and  $\epsilon_m$  the electric permittivity of the dielectric and metal, respectively. The SP electric field decays exponentially in both directions orthogonal to the interface, with typical decay distances at optical wavelengths of a quarter wavelength into the dielectric and of 10 – 20 nm (the penetration depth) into the metal. Furthermore, SPs are damped exponentially in the propagation direction, due to losses in the metal, with typical propagation lengths of a few tens of  $\mu\text{m}$  for a flat surface; the energy flow associated with the propagating SP is mainly directed along the propagation direction but also slightly into the metal. The SP polarization is elliptical in the plane spanned by the surface normal and the SP propagation direction, which means that SPs also have a longitudinal electric field component. The momentum of a SP on a flat metal-dielectric interface is somewhat larger than that of a free-space photon. Therefore, in order to excite SPs with optical pumping, and fulfill conservation of momentum along the interface, additional momentum has to be provided, which can be done by a corrugation of the metal-dielectric interface. The periodic structures of nanohole arrays are one example of such a corrugation.

## 1.3 Quantum Entanglement

In 1935 Einstein, Podolsky and Rosen voiced their uneasiness with a certain consequence of the quantum theory, which made this theory incompatible with their view on nature [14]. The mentioned consequence is the possibility of two particles being in a state, such that a mea-



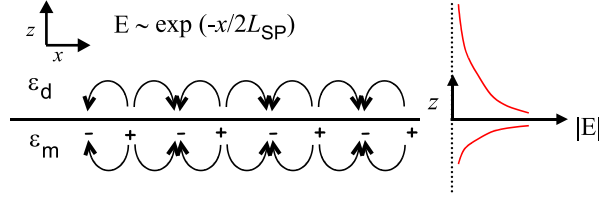


**Figure 1.2:** A sketch of the surface charge density wave and associated electric field of a surface plasmon. The field decays exponentially into the metal and dielectric. Furthermore, the SPs are damped in the propagation direction (denoted here by  $x$ ).

surement on one of the two immediately determines the outcome of a similar measurement on the other one, regardless of the distance between the two particles. This “non-locality” is an essential property of such an “entangled” quantum state. Entanglement was later realized to be a powerful tool, as it can in principle be used to make a “quantum computer” which can be exponentially faster in certain computations than the classical computer [15–17]. A number of experiments so far have focussed on demonstrating entanglement between photons [18–20]. A specific case, discussed in this thesis, is the entanglement between two photons with respect to their polarization. An example of a polarization-entangled state is the state:

$$|\Psi\rangle = \frac{1}{\sqrt{2}} (|H_1 V_2\rangle + e^{i\alpha} |V_1 H_2\rangle) , \quad (1.1)$$

which states that if a photon at position 1 is horizontally polarized, then its counterpart at position 2 is vertically polarized, and vice versa. In fact, for the singlet state with  $\alpha = \pi$ , the polarizations of the two entangled photons are always orthogonal, for every basis, so if photon 1 is polarized at  $45^\circ$  then photon 2 is polarized at  $-45^\circ$ , etcetera.

The main topic of this thesis is the extension of the research of quantum entanglement to the domain of SPs, out of fundamental interest, but also for potential applications using the solid-state medium on whose boundaries SPs can reside. To address this issue, we have studied the way the polarization-entanglement between two photons is affected when one of them is sent through a nanohole array, being coupled to SPs in the transmission process. This experiment is discussed in Chapter 4. In the adjoining chapters some of the classical optical properties of nanohole arrays are studied, with a strong accent on polarization. In the final chapter, Chapter 10, we combine the quantum and classical analysis to provide a model explaining the results of Chapter 4 in terms of the far-field transmission function of the nanohole array. We describe the contents of the chapters in more detail below:

- Chapter 2 describes the production processes we used to make our nanohole array samples, and experimental methods to characterize their optical properties and diagnose production errors. It also includes SP dispersion curves, and higher-diffraction-order reflection and transmission data of the nanohole arrays.
- Chapter 3 provides an in-depth theoretical analysis of a spontaneous parametric down-conversion source of polarization-entangled photons. The limitations to the attainable degree of entanglement are discussed and compared to experimental results.

## 1. Introduction

- Chapter 4 presents the pivotal experiment of this thesis, investigating the decoherence induced by nanohole arrays as they are placed in the paths of polarization-entangled photons. The degree of entanglement behind the arrays is found to be limited by the opening angle on the array, where focussing reduces the entanglement.
- Chapter 5 contains measured zeroth-order reflection spectra of a square nanohole array. The reflection from the two sides of the sample are found to be spectrally different. By comparing the amplitudes of the peaks in both spectra, the interface on which the SPs are resonantly excited can be determined, and a rough estimate of the coupling strength between the SPs on both interfaces can be obtained.
- Chapter 6 discusses polarization-resolved measurements of the far-field transmission function of a square nanohole array. It relates obtained far-field pictures to SP propagation.
- Chapter 7 describes the direct optical imaging of the transmission at the backside of a nanohole array. In the images so-obtained propagating SPs are visible separate from the direct transmission through the holes. The Fano-type interference between the two contributions to the transmission is analyzed to obtain their relative phase and amplitude.
- Chapter 8 investigates experimentally the optical depolarization induced by square and hexagonal nanohole arrays on a fully polarized input beam. The results are presented using the Mueller matrix formalism.
- Chapter 9 presents an analytic model of the far-field transmission function of square and hexagonal nanohole arrays. The model is based on a Fano-type interference between a resonant surface-plasmon contribution and a non-resonant contribution directly through the holes. The results of the model are compared to experimental results similar to those of Chapter 8.
- Chapter 10 discusses the relation between the quantum measurements of Chapter 4 and the classical measurements of Chapter 8. It demonstrates that both measurements depend in identical ways on the far-field transmission function of the nanohole array, discussed in Chapter 6.

There is some overlap between the chapters, as most of them are in fact published papers. Consequently, the chapters can be read separately.

## CHAPTER 2

---

### Characterization of nanohole arrays in metal films

---

*We discuss a number of experimental tools that can be used to characterize subwavelength hole arrays in metal films. We study samples made with two different techniques: electron-beam lithography and ion-beam milling.*

## 2.1 Production and visual analysis of hole arrays

There are currently two methods available to make periodic patterns of holes with diameters smaller than 300 nm in metal layers: i) electron-beam lithography and ii) ion-beam milling. In this chapter we will discuss both techniques and some of their limitations as observed from a number of hole array samples.

All hole array samples discussed in this thesis are of the form sketched in Fig. 1.1(b). They consist of a gold layer perforated with circular holes, which is attached to a glass substrate by a titanium or chromium bonding layer. To be able to observe effects which are dominantly due to SPs there are a number of criteria that a hole array has to obey: i) the gold layer has to be at least an order of magnitude thicker than the skin depth (negligible direct transmission through the metal layer), but ii) still sufficiently small compared to the optical wavelength to avoid excessive waveguide losses in the holes [21] and iii) the lossy bonding layer has to be as thin as possible if one wants to excite SPs at the metal-glass interface with the highest possible amplitude. To fulfill these conditions we choose the gold layer thickness to be 200 nm, which is much larger than the skin depth of  $\approx 12$  nm but still smaller than the typical wavelength of 800 nm, and the bonding layer thickness to be 2 nm. A further technical demand for the type of arrays that we are interested in is that the holes have to be sufficiently accurately spaced (to avoid spectral broadening of the resonance) and circularly shaped (to avoid dichroism). We will discuss the latter demands for both production techniques below.

### 2.1.1 Samples made with e-beam lithography

The electron-beam lithography that we used was developed by Arjan van Zuuk and Emile van der Drift at DIMES in Delft. It essentially comprises the following steps: first, an array of pillars is defined with an e-beam device, where (at least) the bottom part of the pillars is made of material that can be dissolved chemically. Then, in between (and on top) of the pillars the metal layers are deposited, and finally the pillars are removed (“lift-off”) by chemical etching. Table 2.1 gives the production steps in more detail. This somewhat intricate scheme is necessary because electrons cannot directly make holes in gold, due to their small mass.

The main difficulty of this production process proved to be the last lift-off step. The pillars, which consist of (from top to bottom) gold, titanium, electronresist and photoresist, must be dissolved and shaken loose in such a way that they will not “trip over” and stick to the bulk gold layer in between the holes by Van der Waals forces. This requires the right timing and concentration of the etching and a proper use of gravity. It also requires the right timing of all previous baking and plasma-etching steps to keep the pillars soft enough for the final lift-off. Figure 2.1 shows pictures of an array of which the pillars were not fully dissolved and became attached to the bulk gold. Figure 2.1(a) shows an overview optical microscope picture and Fig. 2.1(b) shows a detail scanning electron microscope picture.

Apart from this lift-off difficulty, we were able to successfully produce usable hole arrays with this method. Electron microscope pictures of one good sample are shown in Fig. 2.2, where (a) is a top view and (b) a view taken at a different angle. From the latter picture one can see that some residue material from the pillars remains attached to a few hole edges, but that the holes are generally quite clean.

The major advantage of the e-beam method is that relatively large area arrays ( $1 \times 1 \text{ mm}^2$ )

**Table 2.1:** *The e-beam production process in detail.*

1	Spin coating plus baking of a $\approx 1 \mu\text{m}$ photoresist (S1813) layer which serves as the bottom part of the pillars
2	Deposition by sputtering of approximately 20 nm Ge layer (conductive loss channel for scattered electrons in the e-beam step)
3	Spin coating of $\approx 120$ nm electroresist (SNR) on top of a thin photo resist (HMDS) bonding layer plus baking ( $\approx 2$ minutes at $60^\circ$ )
4	E-beam pattern definition of a square array of circles
5	Development of the electroresist in xylene (with cyclohexane as stopper) leaving the top part of the pillars clear
6	Cleaning in oxygen plasma
7	Plasma etching of the Ge layer
8	Chemical etching of the photo resist remaining in between the pillars
9	Deposition of 2 nm Ti bonding layer and 200 nm Au top layer
10	“Lift-off” of the pillars by chemically etching (with ultrasonic vibration) of the lower part consisting of photoresist

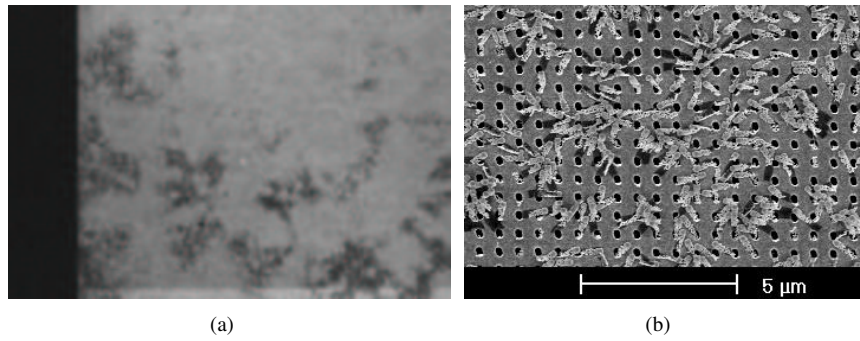


**Figure 2.1:** Pictures of dielectric pillars remaining on the metal surface after the “lift-off” process has been applied. The pictures are taken with (a) an optical microscope, picture roughly  $400 \mu\text{m}$  full width and (b) a scanning electron microscope, scale bar  $5 \mu\text{m}$ .

can be produced, with high accuracy of the lattice spacing and hole shapes. A disadvantage is the complexity of the process.

### 2.1.2 Samples made with ion-beam milling

In comparison with the previously discussed electron-beam lithography the focussed-ion-beam (FIB) production process is very simple. First, a small (2-3 nm thick) bonding layer of titanium or chromium is evaporated onto a glass substrate. Second, a 200-nm thick gold layer is evaporated onto the bonding layer. Finally, the desired hole pattern is etched into the metal layers by bombardment with gallium ions of sufficient momentum (a few keV). The last step was performed for us by Paul Alkemade at the Material Sciences department in Delft. The advantage of the FIB method is clearly its simplicity, resulting in a high production efficiency.

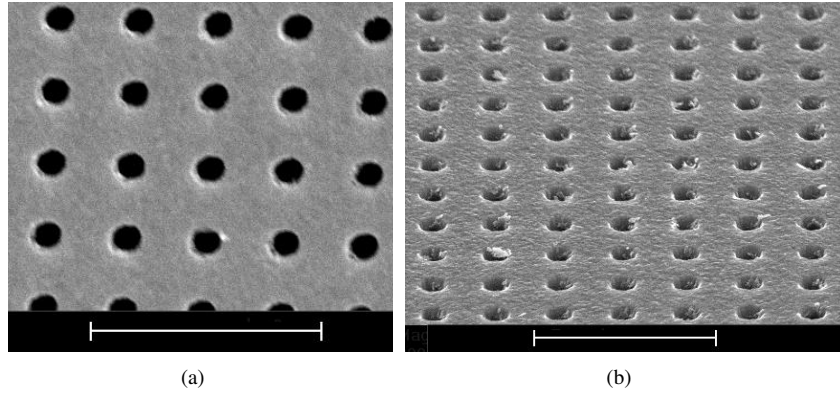


**Figure 2.2:** Scanning electron microscope pictures of a “clean” square hole array, (a) top view and (b) tilted view, with scale bars 2 μm.

However, due to limitations of the FIB we used, the dimensions of the arrays were maximally  $100 \times 100 \mu\text{m}^2$ , i.e., a factor 100 smaller in area compared to the e-beam arrays. This can be a limiting factor for measurements where the total transmitted power through the array is critical.

Figure 2.3 shows a SEM image of a hexagonal array produced with the FIB method. As can be seen in the picture, over small areas the array quality is very high, without surface contaminations. However, over larger areas deviations in symmetry and lattice spacing are generally visible in the arrays that were produced with i-beam (see Section 2.3). These deviations are probably caused by misalignment errors in the i-beam device, which we were unable to correct.

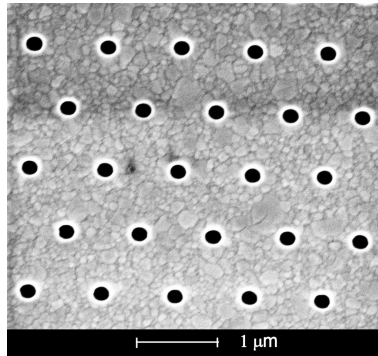


**Figure 2.3:** SEM picture of a hexagonal hole array made with ion-beam milling.

## 2.2 Optical measurement of the lattice period

The most important parameter for controlling the resonance wavelength of a nanohole array is the lattice period. To check the accuracy of the FIB device, we have measured the lattice period optically using diffraction orders in reflection. We use this optical method because it provides for an absolute-distance measurement, whereas, for instance, a scanning electron microscope gives results that depend on calibration. This is done with the setup shown in Fig. 2.4. By measuring the angles  $\alpha$ ,  $\phi$  and  $\theta_m$  with illumination at known  $\lambda$  we obtain the lattice constant

$$a = \frac{Cm\lambda}{[\sin(\alpha/2) + \sin \theta_m] \cos \phi}, \quad (2.1)$$

with  $C = 1$  for a square lattice and  $C = \frac{2}{\sqrt{3}}$  for a hexagonal lattice, respectively [27]. Here  $\theta_m = \arctan(y/x)$ , the angle of incidence on the array is  $\alpha/2$  and the factor  $\cos \phi$  arises because of a possible tilt between the array axis and the horizontal plane in which the distances  $x$  and  $y$  are measured.

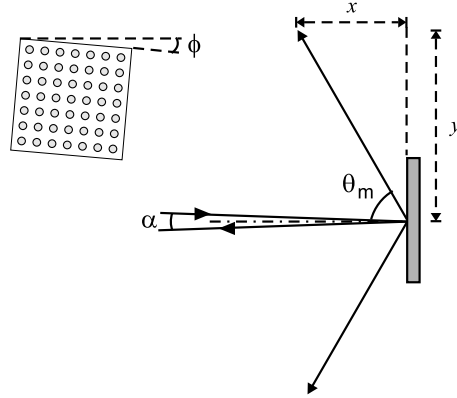


**Figure 2.4:** The experimental setup used to optically measure the lattice constant of a nanohole array. The array is illuminated by a coherent He-Ne beam incident at angle  $\alpha$ .

The error in the value for  $a$  obtained with this method is dominated by the errors in  $\alpha$  and  $\sin(\theta_m) = y/\sqrt{x^2 + y^2}$ , because  $\cos(\phi) \approx 1$  at the experimentally attainable  $|\phi| \leq 2 \times 10^{-3}$ . The total relative error  $\frac{\Delta a}{a}$  can be made as low as 0.3-0.4%, corresponding to an absolute error of only 2-3 nm, by setting  $\alpha = 0$  (easily done to within  $2 \times 10^{-3}$ ) and measuring the distances  $x$  and  $y$  accurate to within 2 mm and 1 cm, respectively.

Table 2.2 shows the lattice spacings as measured for a number of arrays. By comparing the specified spacing (middle column) with the measured spacing (rightmost column) we find that the i-beam device has a 0.7 to 1.0 percent deviation in its calibration, whereas the e-beam device has a negligible calibration error.

**Table 2.2:** Optically measured lattice spacings.

array type	specified $a$	measured $a$
square, e beam	700 nm	$699 \pm 2$ nm
square, i beam	765 nm	$759 \pm 4$ nm
hex, i beam	883 nm	$874 \pm 4$ nm

### 2.3 Spectral measurements

One of the most important tools to characterize nanohole arrays is the analysis of their transmission spectrum. This spectrum contains information about lattice spacings, array symmetry and SP propagation and dispersion. To extract this information we use a simple model, which is currently widespread [1, 4]. In this model, the resonance frequencies  $\omega_{SP}$  and resonance widths  $\Delta\omega_{SP}$  of the transmission maxima are determined by the SP dispersion in combination with the SP momentum  $k_{SP}$ . The SP dispersion relation is given by

$$k_{SP} = \hat{n}_{\text{eff}} \frac{\hat{\omega}_{SP}}{c}, \quad (2.2)$$

where the complex frequency  $\hat{\omega}_{SP} = \omega_{SP} + i\Delta\omega_{SP}$  [22] and the complex effective refractive index  $\hat{n}_{\text{eff}} \equiv \sqrt{\frac{\epsilon_1 \epsilon_2}{\epsilon_1 + \epsilon_2}}$ , and  $\epsilon_1$  and  $\epsilon_2$  are the dielectric constants of the metal and the dielectric, respectively; usually the values for the bulk materials are used. The momentum necessary for the excitation of SPs with momentum  $\vec{k}_{SP} = k_{SP} \vec{e}_{SP}$  (and  $k_{SP} > n_1 \omega/c$ ) is supplied by the component of the incident photon momentum projected on the array surface  $\vec{k}_{//}$ , plus a lattice component supplied by the reciprocal array vectors, which are labelled  $(N_1, N_2)$ . For square and hexagonal arrays with hole spacing  $a$  the SP momentum is thus given by

$$\vec{k}_{SP} = \vec{k}_{//} + (N_1 \vec{e}_1 + N_2 \vec{e}_2) \frac{2\pi C}{a}, \quad (2.3)$$

with  $C = 1$  for a square and  $C = \frac{2}{\sqrt{3}}$  for a hexagonal array. The normalized vectors  $\vec{e}_m$  ( $m = 1, 2$ ) are reciprocal lattice vectors, where for the hexagonal array  $C > 1$  because  $\vec{e}_1 \cdot \vec{e}_2 \neq 0$ . The incident photon momentum depends on the angle of incidence  $\theta$  via  $|\vec{k}_{//}| = k_{in} \sin \theta$ .

The spectra (at normal incidence) can be used to characterize the quality of the arrays. Information on the *homogeneity* of the lattice spacing of the arrays is gained by comparing the peak positions for fixed-polarized illumination for different transverse spot positions on the array. Information on the lattice *symmetry* is obtained by comparing the transmission-peak wavelengths and intensities for one linearly polarized input beam at normal incidence with an orthogonally polarized input beam. For ideal square and hexagonal arrays, the spectrum would be the same for the two polarizations and for each position. For arrays with a deformed lattice, or for instance a slightly rectangular instead of square symmetry, the transmission peaks will be at different wavelengths for a polarization along one of the array basis vectors as compared to a polarization along the other basis vector. Of course, apart from deviations of the lattice symmetry, also the holes themselves could be deformed (rectangular/elliptical instead of square/circular). Such deformations can be recognized in the spectra



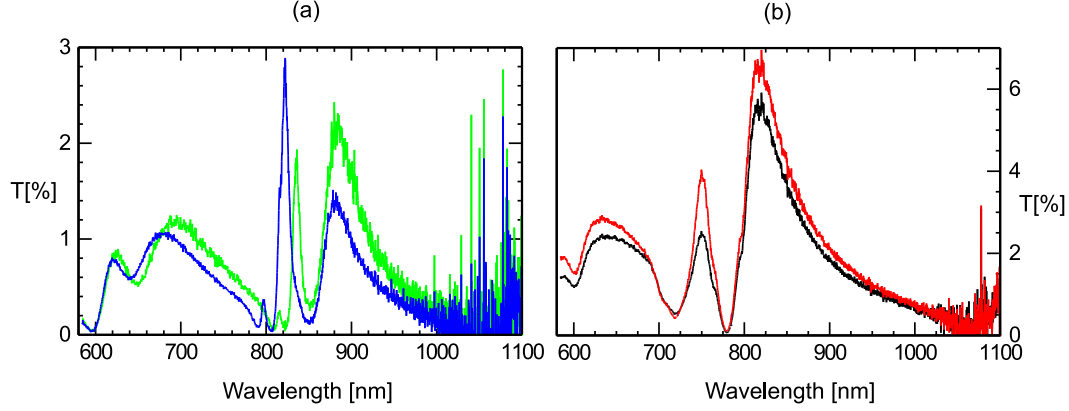


**Figure 2.5:** The transmission spectra of a square array made with a) ion beam and illuminated with two orthogonal polarizations, b) electron beam and illuminated at two different positions.

as the occurrence of different transmission peak powers, but equal resonance frequencies, for two orthogonal polarizations (dichroism).

We measure the transmission spectra with an incandescent light source that is focused onto the hole array in such a way that the numerical aperture (NA) of the beam is still limited (in practice we use a FWHM angular width of  $\approx 0.5^\circ$ ). The polarization of the illumination is set by a polarizer. The transmitted light is coupled into a fibre (core diameter 50 or 200  $\mu\text{m}$ ) which in turn illuminates a commercial grating spectrometer (Avantes Avaspec2048). The hole array can be positioned in the beam by a three-axis translation stage ( $\approx 5 \mu\text{m}$  resolution), and the illumination angle of incidence on the array can be controlled by a rotation stage ( $\approx 0.1^\circ$  resolution).

When applying the mentioned analysis to our arrays, we find that the e-beam arrays typically have much less symmetry defects and dichroism than the i-beam arrays. Figure 2.5(a) shows, as an example, the transmission spectrum of an i-beam square array measured with illumination at normal incidence with two orthogonal polarizations (gray and black curves), showing both dichroism (different peak powers) and symmetry errors (different peak wavelengths); the spectra of this array changed considerably as a function of the position of the illumination on the array. The e-beam arrays typically do show varying peak intensity as a function of illumination-spot position, as shown for a square array in Fig. 2.5(b). This is probably caused by the presences of rest material of the production process on these arrays. The e-beam-made square array that was used for most of the experiments discussed in this thesis showed no dichroism and no position-dependent resonance-frequency shifts. The i-beam-made hexagonal array discussed in a number of chapters did show both defects (see Chapter 8).

The (average) lattice spacing determined independently with the measurement of Section 2.2 can be used to compare the measured peak wavelengths to the model predictions. The precise “correction factors” between experimental and theoretical values are shown in Table 2.3. These factors are calculated using  $n_{eff}$  values obtained from Refs. [23, 24],  $n_{glass} = 1.51$  (BK7) for the first sample and  $n_{glass} = 1.453$  (fused silica) for the others. We

find that the measured peaks are always redshifted as compared to the theoretical ones, with shifts in the range of 2 to 5%. This redshift can be seen in Fig. 2.5(b), where the theoretical peak wavelengths [indicated by the dashed vertical lines in Fig. 2.5(b)] are 722 nm for the air-side  $(\pm 1, 0)$  and  $(0, \pm 1)$  modes and 785 nm for the glass-side  $(\pm 1, \pm 1)$  modes, whereas the observed peak wavelengths are 750 and about 815 nm, respectively. We can think of three explanations for these deviations. First, the dispersion relation for SPs on hole arrays differs from that for a smooth surface, which could cause a redshift of the peaks. A second explanation is that the model neglects the direct transmission of the optical field through the holes, which is small but not negligible. The interference between the direct and resonant-SP contributions to the transmission can generate asymmetric Fano-type lineshapes, which have peaks that are shifted by a fraction of the linewidth with respect to the peaks of the underlying Lorentzian resonances. Fano-type effects are discussed in more detail in Chapter 9 and 7 of this thesis. The foregoing limitations of the simple model behind Eqs. (2.2) and (2.3) have also been demonstrated recently in experiments on arrays with different hole diameters which were otherwise identical [25], where it was shown that, for the  $\{(\pm 1, 0), (0, \pm 1)\}$  and  $(\pm 1, \pm 1)$  modes, increasing the hole diameter increases the redshift. Other experiments have investigated the dependence on layer thickness [21] and hole shape [9], both of which are not taken into account in the simple model.

**Table 2.3:** Correction factors between measured and theoretical peak wavelengths. For all samples  $n_{\text{glass}} = 1.453$  unless otherwise specified.

array type	measured lattice spacing	correction factor air-side mode	correction factor glass-side mode
square, e beam ( $n_{\text{glass}} = 1.51$ )	$699 \pm 2$ nm	1.047	1.037
square, i beam	$759 \pm 4$ nm	1.026	1.044
hex, i beam	$874 \pm 4$ nm	1.045	-

From the transmission spectrum at a number of angles of incidence, for s- and p-polarized illumination, the SP dispersion can be determined [4]. By combining Eqs. (2.2) and (2.3) one can find the general expression for the resonance wavelength  $\lambda_{\text{res}}$  for illumination at an angle of incidence  $\vec{\theta} = (\theta_x, \theta_y)$ . To avoid lengthy equations, we will here give only the expressions for a square array (with basis  $\{\vec{e}_x, \vec{e}_y\}$ ), which we tilt around a diagonal, i.e.,  $\sin \theta_x = \sin \theta_y = \sin \theta / \sqrt{2}$ . For the  $(\pm 1, 0)$  and  $(0, \pm 1)$  modes we find:

$$\lambda_{\text{res}}/a = \sqrt{n_{\text{eff}}^2 - \frac{1}{2} \sin^2(\theta)} \pm \sin(\theta)/\sqrt{2}, \quad (2.4)$$

for the  $\pm(1, 1)$  modes, along the tilt axis (s-polarized):

$$\lambda_{\text{res}}/a = [n_{\text{eff}} \pm \sin(\theta)]/\sqrt{2}, \quad (2.5)$$

and for the  $\pm(-1, 1)$  modes, orthogonal to the tilt axis (p-polarized):

$$\lambda_{\text{res}}/a = \sqrt{n_{\text{eff}}^2 - \sin^2(\theta)}/\sqrt{2}. \quad (2.6)$$

From these equations we see that, to first order in the angle, the slope of  $\lambda_{\text{res}}(\theta)$  is purely determined by a numerical pre-factor and is not dependent on, for instance, refractive indices.

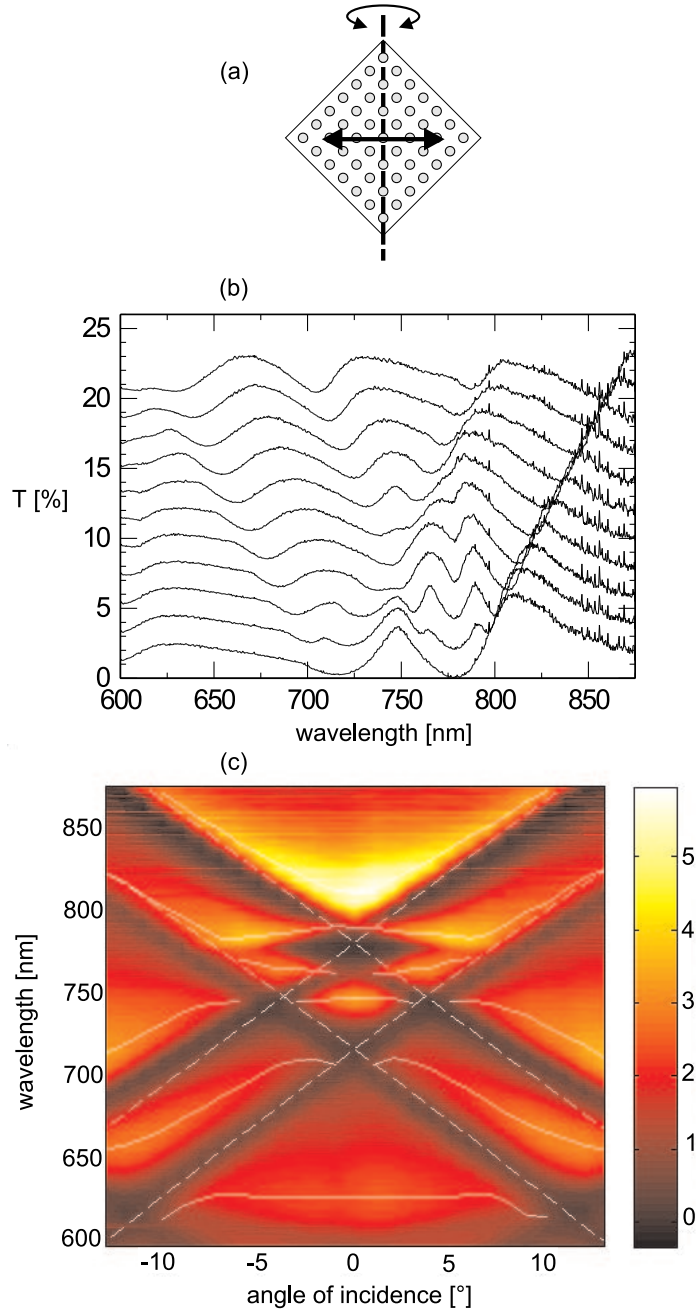


**Figure 2.6:** The SP dispersion on the square hole array for p-polarized input light, obtained by measuring (b) the transmission spectrum for a set of angles of incidence with a  $1^\circ$  interval. (a) The rotation axis (dashed line) was chosen along the array diagonals, with input light polarized along the solid arrow. The white solid lines in (c) indicate the approximate wavelengths of the transmission peaks and the white dashed lines indicate the theoretically expected peak wavelengths, based on Eq. (2.4) to (2.6).

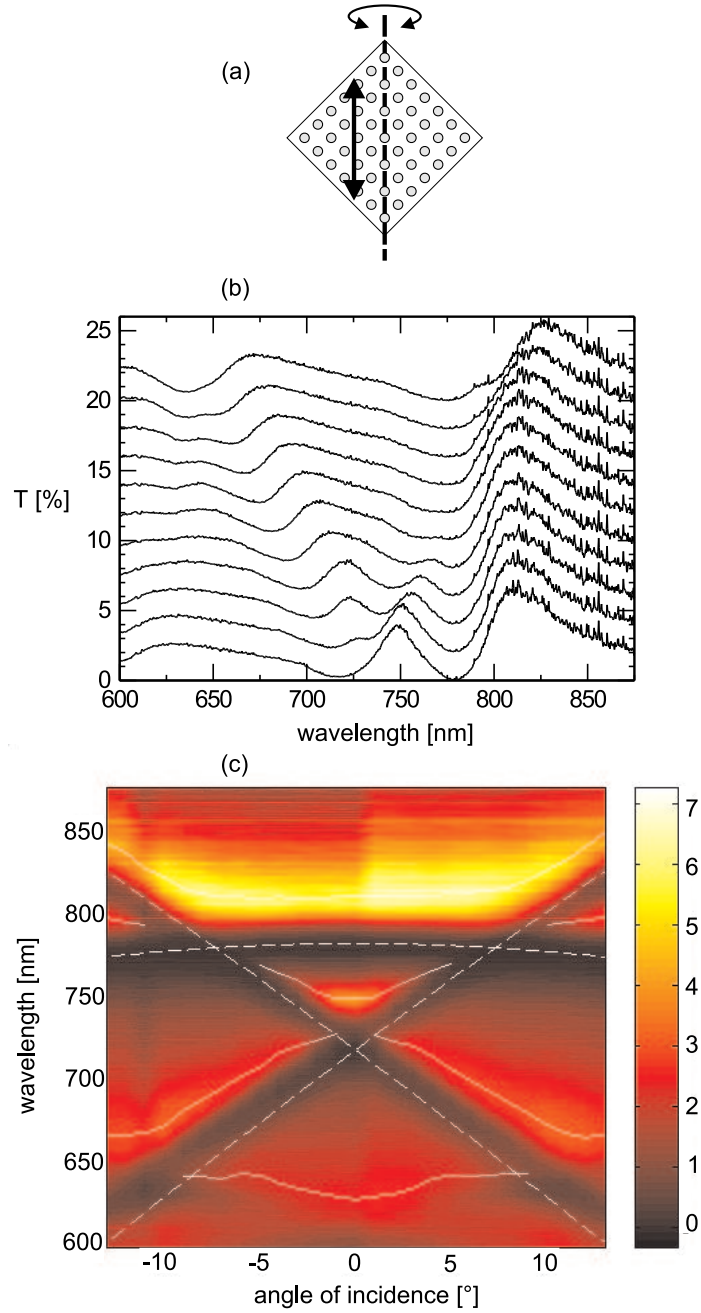


**Figure 2.7:** The SP dispersion on the square hole array for s-polarized input light, obtained by measuring (b) the transmission spectrum for a set of angles of incidence with a  $1^\circ$  interval. (a) The rotation axis (dashed line) was chosen along the array diagonals, with input light polarized along the solid arrow. The white solid lines in (c) indicate the approximate wavelengths of the transmission peaks and the white dashed lines indicate the theoretically expected peak wavelengths, based on Eq. (2.4) to (2.6).

Figure 2.6 and 2.7 show a typical measurement of the SP dispersion for a square array: in both figures, (a) shows the input polarization relative to the rotation axis, (b) shows the measured transmission spectra for  $1^\circ$  steps of the angle of incidence and (c) shows the (interpolated) dispersion. The scale bar on the right of subfigure (c) relates the gray values in the plots to the transmission intensity. The white solid lines are guides to the eye, indicating the measured peak positions. The white dashed lines indicate the theoretical angle-dependent resonance wavelengths for the  $(\pm 1, \pm 1)$  glass-side modes and the  $(\pm 1, 0)$  and  $(0, \pm 1)$  air-side modes, as given by Eq. (2.4) to (2.6).

The dashed lines in Fig. 2.6 and 2.7 do not match well to the experimental solid lines. First, the theoretical curves are much closer to the transmission minima than to the maxima. This deviation is the redshift as discussed above for normal incidence. Second, the slopes of the experimental and theoretical lines are (slightly) different. And third, “extra” peaks, not contained in Eqs. (2.4) to (2.6), appear in the experimental data (see e.g. Fig. 2.6 between 750 nm and 810 nm for angles of incidence of  $1 - 5^\circ$ ). Note, that these extra modes are absent for  $\theta = 0^\circ$ , as can be seen in the transmission spectra at the bottom of Fig. 2.6(b) and 2.7(b). The most probable explanation for these additional resonances is coupling between resonances on either sides of the metal layer, something that is not contained in the simple single-surface model we discuss here. This hypothesis has recently been confirmed in a paper that relates the additional resonances to subradiant modes (antisymmetric versus symmetric) [26].

Another indication for the coupling between different SP modes is the “avoided crossings” of the solid curves in Fig. 2.6 and 2.7, and consequently the occurrence of bandgaps at  $\theta = 0^\circ$ , noticeably for the modes in between  $\lambda \approx 750$  nm and  $\approx 820$  nm. We estimate the size of the bandgaps by measuring the peak-peak distance around  $\theta = 0^\circ$ , which gives gaps of 94 meV around  $\lambda = 730$  nm, 34 meV around  $\lambda = 757$  nm, 53 meV around  $\lambda = 778$  nm and 39 meV around  $\lambda = 800$  nm. These values are of the same order of magnitude as those reported for a 1-dimensional array of slits in Ref. [26].

## 2.4 Conclusions

We have discussed two different production schemes for hole arrays as well as several techniques which can be used to characterize them. Most information is contained in the polarization-resolved transmission spectra. When measured with illumination at normal incidence, these can be used to diagnose errors in the lattice structure as well as the hole shapes. When measured as a function of the angle of incidence, the surface plasmon dispersion on the nanohole array is obtained. We have also discussed a simple single-surface model that is standard in the literature. We find that this model, although useful to understand the basic features, does not satisfactorily describe the detailed structure of the measured surface plasmon dispersion. An improved model would need to describe a coupling mechanism between different SP modes.

## Appendix

### 2.A Hole arrays as diffraction gratings

Apart from the zeroth-order transmission discussed in Section 2.3, hole arrays also exhibit other diffraction orders, both in reflection and transmission, as hole arrays are just a special type of two-dimensional gratings. By illuminating our array (lattice spacing  $a = 700$  nm) with laser light (wavelength  $\lambda_0 = 672$  nm) at approximately normal incidence, we observe four additional reflection and transmission orders, of first order and emitted in directions along the array basis vectors  $(+x, -x, +y, -y)$ . We have measured the intensity of all observable transmission orders  $T_j$  and reflection orders  $R_j$  of a square hole array as a function of the angle of incidence  $\theta$ , at the fixed wavelength  $\lambda_0$ . Note, that  $T_0(\theta, \lambda_0)$  obtained in this way is directly related to the SP dispersion discussed in Section 2.3:  $T_0(\theta, \lambda_0)$  is a cross section of the SP dispersion, such as plotted in Fig. 2.7 and Fig. 2.6, along the line  $\lambda = \lambda_0$ . Unfortunately, at present we are unable to provide a rigorous theoretical analysis of the results, for the same reason that we are unable to accurately describe the SP dispersion: at this moment we lack a model that describes the coupling between different SP modes, that causes the avoided crossings and bandgaps in the dispersion plots of Fig. 2.7 and Fig. 2.6. Nevertheless, we have included the measurements here for didactic purposes and to stimulate future discussions.

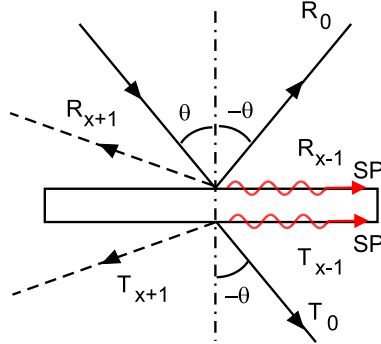


**Figure 2.8:** A sketch of a one-dimensional grating with its zeroth- and first-order transmission and reflection. In this case, the  $m = -1$  orders are past grazing incidence and have become SPs (wiggly lines).

As a qualitative and simplified description, we consider a one-dimensional grating consisting of lines with spacing  $a$  in a perfect conductor of small thickness. When illuminating such a grating with light of wavelength  $\lambda$  and incident at angle  $\theta_i$ , reflection and transmission maxima occur at output angles  $\theta_o$  given by [27]:

$$a(\sin \theta_i + \sin \theta_o) = m\lambda, \quad (2.7)$$

where  $m$  labels the order of the maxima. Note, that this one-dimensional treatment is also applicable to two-dimensional array of square symmetry for small angles of incidence, as in this case the array can be decomposed into two independent one-dimensional gratings. Figure 2.8 shows the grating with its diffraction orders and the convention we use to name

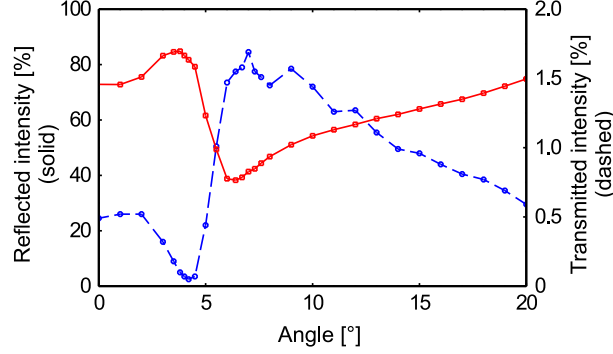


**Figure 2.9:** Zeroth-order intensity reflection (solid) and transmission (dashed) versus angle of incidence on a square array of 672 nm-wavelength light. The rotation axis is orthogonal to the linear input polarization and lies along one of the array axes.

them. In this figure the input angle  $\theta > 0$ , and consequently, the reflections on the right correspond to  $m \leq 0$ , while on the left they correspond to  $m > 0$ . Figure 2.8 provides a nice intuitive explanation of SP excitation: at a certain angle of incidence  $\theta_i$ , one of the reflection orders (in this case  $m = -1$ ) becomes “grazing”, i.e., the  $\theta_o$  of this order becomes equal to  $\pi/2$ . If we further increase  $\theta_i$ , this order so-to-say “disappears” into the metal and can become a SP (wiggly line in Fig. 2.8) if  $\theta_i$  is close to some critical angle determined by material properties.

The measurements shown in Figs. 2.9 to 2.11 were performed with a collimated diode-laser beam ( $\lambda = 672$  nm) illuminating a square hole array (lattice spacing 700 nm) on a rotation stage. For each input angle (tilt axis along one of the array basis vectors) the reflected and transmitted powers of the observable orders were measured with a photodiode (15 mm<sup>2</sup>-surface area). Figure 2.9 shows the intensity of  $R_0(\theta)$  (solid curve) and  $T_0(\theta)$  (dashed curve) for 672-nm wavelength input. The two curves have an opposite trend: where  $R_0$  has a maximum,  $T_0$  has a minimum and vice versa. However, both have an asymmetric shape familiar from measurements on SP resonances in the so-called Kretschmann configuration [13]. As mentioned above, the  $T_0(\theta)$  curve is directly related to the previously discussed SP dispersion of Fig. 2.6 and 2.7, and is just a cross-section along the line  $\lambda = 762$  nm. Indeed, the transmission minimum in Fig. 2.9 agrees well with the minimum for  $\lambda = 672$  nm in the dispersion plots: an angle of  $4.3^\circ \pm 0.5^\circ$  compared to  $5.6/\sqrt{2} = 4.0^\circ \pm 0.4^\circ$  (average of the two dispersion plots), where the factor  $\sqrt{2}$  arises because of the tilting along an array axis instead of along one of the diagonals. Note, that the oscillations present in  $T_0$  for angles larger than  $7^\circ$  are caused by Fabry-Perot type interference effects in the glass substrate of the array.

Figures 2.10 and 2.11 show  $T_j(\theta)$  and  $R_j(\theta)$ , for  $j = \{0, x \pm 1, y \pm 1\}$ . In both measurements the rotation axis was oriented along the  $y$  direction. The order labelled  $x - 1$  becomes grazing at an angle of around  $2.3^\circ$ , which is in agreement with the value calculated from Eq. (2.7) for  $a = 700$  nm and  $\lambda = 672$  nm. The  $y - 1$  order could not be measured due to the mounting of the array, but should behave identical to that of the  $y + 1$  order because of symmetry arguments. The  $T_j(\theta)$  all show a zero at an angle of  $4.3^\circ$  and are all of similar

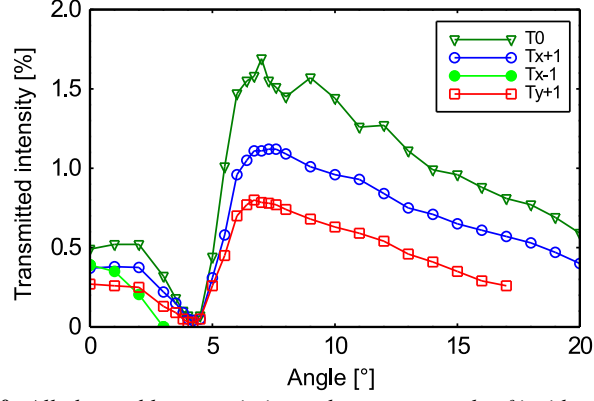


**Figure 2.10:** All observable transmission orders versus angle of incidence on a square hole array of 672 nm-wavelength light ( $T_{y-1} = T_{y+1}$ ). The rotation axis is orthogonal to the linear input polarization and lies along one of the array axes.

magnitude. The reflection curves on the other hand have a much larger absolute difference, where  $R_{x+1}$  (along the polarization direction) is larger than  $R_{y+1}$  (orthogonal to the polarization). Also, the zeroth-order has an opposite trend as compared to the other reflection orders, and to all transmission orders as well. It is obvious that the foregoing observations contain a lot of information about the (optical) physics of the nanohole array, however it seems that, currently, the right theoretical tool to handle the discussed measurements, other than pure numerical modeling, is not available.

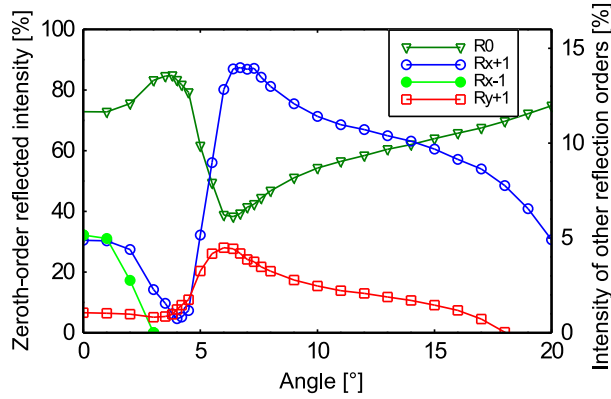


**Figure 2.11:** All observable reflection orders versus angle of incidence on a square hole array of 672 nm-wavelength light ( $R_{y-1} = R_{y+1}$ ). The rotation axis is orthogonal to the linear input polarization and lies along one of the array axes.



## CHAPTER 3

---

### Spontaneous parametric down conversion as a source of entangled biphotons, in theory and practice

---

*We present a theoretical description of the generation of polarization-entangled photon pairs via type-II spontaneous parametric down-conversion. The limitations occurring in an experimental realization of such a source based on BBO crystals are discussed in detail.*

### 3.1 Introduction

The process of spontaneous parametric down conversion (SPDC) and its inverse of sum-frequency generation are well-known in nonlinear optics since the 1960s [28]. In the former process an incident photon of given energy is split (“down-converted”), inside a suitable non-linear medium, into two photons of less energy, such that the total energy and momentum is conserved; in the latter reverse process a single photon with the sum energy of its incident counterparts emerges. It was realized in the 1980s that the down-conversion process can, under certain conditions to be discussed below, efficiently produce quantum-entangled biphoton pairs [20, 29]. Currently, SPDC is the standard way of producing entangled photons for all types of experiments in the domain of quantum information. The basic setup for such an experiment is sketched in Fig. 3.1: a photon of a pump beam is split inside a nonlinear crystal into two entangled photons that travel to detectors 1 and 2. A counter measures the number of coincident detections of 1 and 2, from which a suitable measure for the degree of entanglement can be obtained.

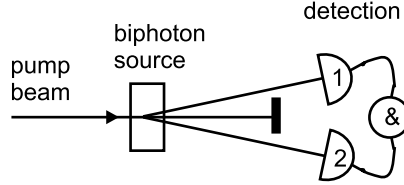


**Figure 3.1:** The basic setup of an entangled biphoton experiment.

The photon pairs generated in type-II SPDC are simultaneously entangled in three sets of variables. The generated two-photon function is nonseparable in i) the polarization, ii) momentum and iii) frequency degrees of freedom. This triply-joint entanglement is seldom taken into account explicitly; one often limits the discussion to entanglement in a single set of variables and ignores the others. For instance, in the case where polarization is considered as the important set, one usually describes the photon pair produced in Fig. 3.1 by the pure “polarization-entangled” state

$$|\Psi\rangle = \frac{1}{\sqrt{2}} (|H_1 V_2\rangle + e^{i\alpha} |V_1 H_2\rangle) , \quad (3.1)$$

where the state  $|H_1 V_2\rangle$  represents the simultaneous emission and propagation of a  $H$ -polarized photon in beam 1 and a  $V$ -polarized photon in beam 2, the  $H$ - and  $V$ -directions being defined by the birefringent axis of the generating nonlinear crystal. The coarse spatial information is implicitly contained in the beam labelling 1 and 2, but the finer details are neglected. The frequency information is removed completely.

In this chapter, we will describe the full produced SPDC wave function in the paraxial approximation, and discuss the conditions under which the simplified version of Eq. (3.1) holds experimentally. In Section 3.2 we determine the spatial distribution of the SPDC photons and give the polarization-entangled state that is obtained using suitable selection. In Section 3.3 we introduce the so-called concurrence, a quantity that measures the degree of entanglement of the produced biphoton state, and discuss some of the experimental requirements for a high

efficiency and quality of the source. In Section 3.4 we present measurements made with a real SPDC setup and compare these to the theory.

## 3.2 Theory of SPDC as a biphoton source

### 3.2.1 The biphoton wave function

In a description distilled from Ref. [30, 31] the biphoton part of the total field generated in type-II SPDC can be written in the paraxial approximation as:

$$|\Psi\rangle = \int d\vec{q}_o d\vec{q}_e d\omega_o d\omega_e \Phi(\vec{q}_o, \omega_o; \vec{q}_e, \omega_e) |\vec{q}_o, \omega_o; \vec{q}_e, \omega_e\rangle. \quad (3.2)$$

Here

$$\Phi(\vec{q}_o, \omega_o; \vec{q}_e, \omega_e) \propto \tilde{E}_p(\vec{q}_o + \vec{q}_e; \omega_o + \omega_e) \times L \text{sinc}(\phi) \times e^{i\phi}, \quad (3.3)$$

where  $\tilde{E}_p(\vec{q}, \omega)$  is the spatial and frequency spectrum of the (classical) pump beam,  $\text{sinc}(x) \equiv \sin(x)/x$ ,  $L$  is the thickness of the nonlinear crystal, and the function  $\phi = L\Delta k/2$  quantifies the so-called phase mismatch for propagation over half the crystal thickness (the average phase mismatch). The sets  $(\vec{q}_o, \omega_o)$  and  $(\vec{q}_e, \omega_e)$  are the transverse wavevector and optical frequency of the ordinary and extra-ordinary photons, respectively. The biphoton wave function  $|\Psi\rangle$  contains integrals over all these variables. The subscripts  $o$  and  $e$  label the ordinary and extra-ordinary polarization, respectively.

### 3.2.2 Phase matching

Most of the properties of the SPDC light are contained in the functional dependence of the phase mismatch  $\phi(\vec{q}_o, \omega_o; \vec{q}_e, \omega_e)$  on its variables. This function determines both the combined spatial and spectral distribution of the SPDC light as well as the maximally attainable degree of polarization entanglement. For a plane-wave pump at normal incidence and fixed frequency  $\omega_p$ , the (longitudinal) wavevector mismatch  $\Delta k = k_{p,z} - k_{o,z} - k_{e,z}$  (sketched in Fig. 3.2) can be written in the following dimensionless form:

$$\frac{c}{\Omega} \Delta k = -C + (n_{o,gr} - n_{e,gr}(\Theta_c)) \frac{\delta\omega_e}{\Omega} + \langle 1/n \rangle \theta_{e,x}^2 + \langle 1/n \rangle (\theta_{e,y} - \theta_{\text{off}})^2. \quad (3.4)$$

A complete derivation of this formula, which is basically a rewritten form of Eq. (37) in Ref. [32], can be found in the Appendix. In this equation, we have introduced the following variables (see also the Appendix for a complete list of symbols): SPDC center frequency  $\Omega = \omega_p/2$ , the frequency mismatch  $\delta\omega_e \equiv \omega_e - \Omega = \Omega - \omega_o$  ( $\delta\omega_e \ll \Omega$ ), and the external angles  $(\theta_{o,x}, \theta_{o,y})$  and  $(\theta_{e,x}, \theta_{e,y})$ , where the  $x$  and  $y$  directions are chosen along the  $o$  and  $e$  polarizations, respectively. Furthermore, we define the constant  $C = n_o(\Omega) + n_e(\Theta_c, \Omega) - 2n_e(\Theta_c, \omega_p) + \langle 1/n \rangle \theta_{\text{off}}^2$ , where  $n_{o,gr}$  and  $n_{e,gr}(\Theta_c)$  are the group refractive indices and  $\Theta_c$  is the crystal cut angle, the average inverse refractive index  $\langle 1/n \rangle \equiv \frac{1}{2n_o} + \frac{1}{2n_e(\Theta_c)}$ , the external offset angle  $\theta_{\text{off}} \equiv \frac{1}{2\langle 1/n \rangle} \rho(\Theta_c)$  and the internal walk-off angle  $\rho(\Theta_c)$  (see Appendix).

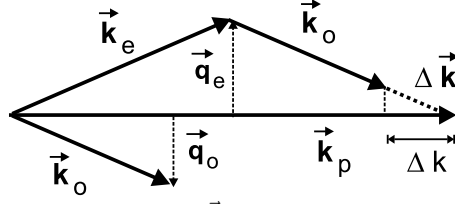


**Figure 3.2:** The wavevector mismatch  $\Delta \vec{k}$  is the vectorial difference  $\vec{k}_p - \vec{k}_o - \vec{k}_e$ . The scalar  $\Delta k$  is the component of  $\Delta \vec{k}$  along  $\vec{e}_z$  (for simplicity  $\vec{k}_p \parallel \vec{e}_z$  was drawn). The transverse components of the wave vectors for the  $o$ - and  $e$ -polarized photons are indicated as  $\vec{q}_o$  and  $\vec{q}_e$ , respectively.

### 3.2.3 The angular distribution of type-II SPDC light

The angular distribution of the SPDC light is found by determining the angles in the far field for which the generated “biphoton state amplitude function”  $\Phi$  (Eq. (3.3)) differs from zero. Because  $\Phi \propto \text{sinc}(\Delta k L/2)$  the SPDC emission peaks around  $\Delta k = 0$  and is zero for  $L\Delta k = \pm 2\pi$ . A closer inspection of Eq. (3.4) shows that the  $e$ -polarized SPDC light is emitted in a ring (in the far field) centered around  $\theta_x = 0$  and  $\theta_y = \theta_{\text{off}}$ . The radius of this ring is determined by the various refractive indices and the angle between pump beam and optic axis through  $\theta_{\text{off}}$  (both contained in the parameter  $C$ ), and the frequency mismatch  $\delta\omega_e$ . The  $o$ -polarized SPDC light is emitted simultaneously in a similar ring, which is a mirror-flipped image of the  $e$ -ring around the line  $\theta_y = 0$ . The reason for this reversal is the conservation of transverse momentum, which (close to frequency degeneracy) translates into  $\theta_{o,i} = -\theta_{e,i}$  for  $i = x, y$ . The resulting pair of rings in the far-field are shown in Fig. 3.3, where (b) is a measured version and (c) a sketch showing the coordinate system used below.

Figure 3.4 shows what happens to the emitted far field at frequencies different from  $\Omega = \omega_p/2$ . For a negative birefringent crystal ( $n_e < n_o$ ) like BBO, an increase of the detection frequency decreases the  $e$ -polarized ring diameter and increases the  $o$ -polarized ring diameter, leading to an effective upward shift of the crossings (see Fig. 3.4). Away from frequency degeneracy the rings are unequal in size because they correspond to different emission conditions:  $\delta\omega_e > 0$  and  $\delta\omega_e < 0$ , respectively.

Because the generated biphoton state amplitude is proportional to  $\text{sinc}(\Delta k L/2)$  the theoretical zeros of the SPDC rings are determined by the relation  $\Delta k = \pm 2\pi/L$ . This relation provides for two useful parameters. First of all, for a fixed detection angle, the emitted light will have a finite SPDC-spectral width  $\Delta\omega_{\text{SPDC}}$  equal to

$$\Delta\omega_{\text{SPDC}} = \frac{2\pi c}{(n_{o,\text{gr}} - n_{e,\text{gr}}(\Theta_c)) L} = \frac{2\pi}{\tau_{o,\text{gr}} - \tau_{e,\text{gr}}(\Theta_c)}, \quad (3.5)$$

where  $\tau_{o,\text{gr}}$  and  $\tau_{e,\text{gr}}(\Theta_c)$  are the transit times through the generating crystal of a (frequency-degenerate)  $o$ - and  $e$ -polarized optical wave packet, respectively. The spectral width  $\Delta\omega_{\text{SPDC}}$  is Fourier-related to the so-called *longitudinal* walk-off, which quantifies the time delay  $\tau_{o,\text{gr}} - \tau_{e,\text{gr}}(\Theta_c)$  between  $o$ - and  $e$ -polarized wave packets that are produced simultaneously near the input facet and propagate through the entire generating crystal.

A second consequence of the relation  $\Delta k = \pm 2\pi/L$  is that it determines the “thickness” or

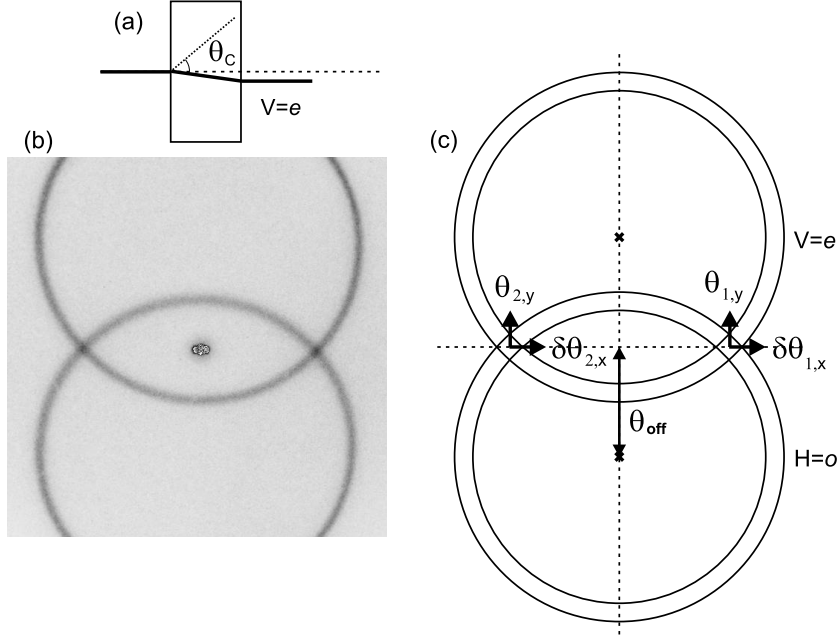


**Figure 3.3:** (a) A side view of a (negative-birefringent) crystal showing the optic axis (dashed line) and the downward vertical beam walk experienced by  $e$ -polarized light. (b) Far-field profile of the frequency-degenerate type-II SPDC emitted from a 2 mm-thick BBO crystal and measured with an intensified CCD (full view  $5.6^\circ \times 5.6^\circ$ ). Frequency selection was achieved with interference filters of a 5-nm spectral width centered around the double pump wavelength. The central spot is a residue of the pump light. (c) Sketch of the far-field profile of the emitted SPDC light, showing two intersecting rings of orthogonal polarization (labelled  $H$  and  $V$ ), centered at the offset angle  $\theta_{\text{off}}$ . Only the photon pairs at the crossings of these rings, which define the general directions of beam 1 and 2, can be polarization entangled, because the polarization of these photons is not known in advance, whereas it is known for photons originating from outside the intersections. For convenience, we introduce two local angular coordinate systems  $(\delta\theta_{i,x}, \theta_{i,y})$  [ $i = 1, 2$ ] that have their origin exactly at the mentioned crossings.

angular width  $\Delta\theta_{\text{SPDC}}$  of the SPDC rings at fixed emission frequency. From an experimental point of view it is convenient to work under conditions where the  $o$ - and  $e$ -polarized SPDC rings intersect at right angles; the reason is that such intersections have the highest symmetry and are best compatible with circular apertures, so that one expects the best compromise between coincidence rate and degree of entanglement in this geometry. At frequency degeneracy ( $\delta\omega_e = 0$ ) this condition of perpendicular intersection is met for  $C = 2 \langle 1/n \rangle \theta_{\text{off}}^2$ , where the intersection coordinates  $\theta_{e,x} = -\theta_{o,x} = \pm\theta_{\text{off}}$  and  $\theta_{e,y} = -\theta_{o,y} = 0$  both correspond to  $\Delta k = 0$ . In this case the SPDC angular width  $\Delta\theta_{\text{SPDC}}$ , as measured in either  $x$  or  $y$  direction, is

$$\Delta\theta_{\text{SPDC}} = \frac{\pi c}{\Omega \langle 1/n \rangle L \theta_{\text{off}}} = \frac{\lambda_0}{L \rho(\Theta_c)}, \quad (3.6)$$

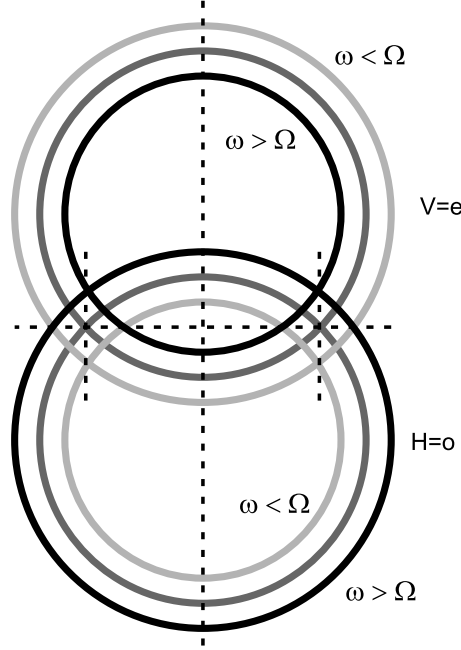


**Figure 3.4:** The far-field profile of the emitted SPDC light changes with detection frequency. At the frequency-degenerate point, where  $\omega = \Omega \equiv \omega_p/2$ , it consists of two rings of equal size depicted in dark-gray. At larger detection frequency ( $\omega > \Omega$ , black), the radius of the *o*-polarized ring increases, while the *e*-polarized ring decreases in size. At smaller detection frequency ( $\omega < \Omega$ , light-gray), the reverse applies. Note that a detuning of the detection frequency away from frequency degeneracy results in a vertical shift of the ring crossings, whereas their horizontal position remains unchanged up to first order.

where  $\lambda_0 = 2\pi c/\Omega$  is the degenerate SPDC wavelength. The angular ring width in the radial direction is a factor  $\sqrt{2}$  smaller at  $\Delta\theta_r = \Delta\theta_{\text{SPDC}}/\sqrt{2}$ . The angular width  $\Delta\theta_{\text{SPDC}}$  is Fourier-related to the so-called *transverse* walk-off, which quantifies the transverse displacement  $\Delta y$  of the *e*-ray with respect to the *o*-polarized ray. For rays starting at the input facet this displacement is  $\Delta y = L\rho(\Theta_c) = 2L\langle 1/n \rangle \theta_{\text{off}}$ .

The natural spectral width  $\Delta\omega_{\text{SPDC}}$  and natural angular width  $\Delta\theta_r$  or  $\Delta\theta_{\text{SPDC}}$  are both defined as the distance between the peak value and the first minimum of the sinc-function. These values are therefore slightly ( $\approx 1.13\times$ ) larger than the full width at half maximum (FWHM) of the SPDC intensity profile with its accompanying  $\text{sinc}^2$  shape. Because the angular width is inversely proportional to its diameter, due to the quadratic dependence in Eq. (3.4), the ring area and the related angular-integrated SPDC power are virtually independent of the ring diameter.

In further discussions on phase matching we will rely heavily on the expanded form of Eq. (3.4), which we have already linearized around the frequency-degenerate point (via  $\omega_e = \Omega + \delta\omega_e$ ), but will now also linearize around either one of the two (frequency-degenerate and

right-angle) crossings of the SPDC rings. Using  $\theta_{e,x} \equiv \pm\theta_{\text{off}} + \delta\theta_{e,x}$ , we find

$$\frac{L\Delta k}{2\pi} = \frac{\phi}{\pi} = \frac{\delta\omega_e}{\Delta\omega_{\text{SPDC}}} + \frac{\pm\delta\theta_{e,x} - \theta_{e,y}}{\Delta\theta_{\text{SPDC}}}, \quad (3.7)$$

where the plus sign is for intersection 1 and the minus sign for intersection 2. As a sign check, we note that linearization around the intersection  $\theta_{e,x} \approx +\theta_{\text{off}}$  corresponds to a plus sign in front of the  $\delta\theta_{e,x}$ -term and therefore to a  $+45^\circ$  orientation of this part of the  $e$ -polarized ring. This is consistent with the earlier remark that the  $e$ -polarized SPDC ring is centered around the positive angle  $\theta_y = \theta_{\text{off}}$  (see Fig. 3.3).

### 3.2.4 The entangled state produced in type-II SPDC

Equation 3.2 gives a complete description of the biphoton wave function produced in type-II SPDC. It is, however, generally not the most convenient representation, because the quantum entanglement is hidden in the symmetry properties of  $\Phi$  [33]. In a typical experimental setup, detection takes place behind two apertures that are centered around the crossings of the SPDC rings to single out polarization-entangled photon pairs. When we apply this spatial filtering to Eq. (3.2) there are obviously only two relevant angular integration ranges: where the  $o$ -polarized photon passes either through crossing region 1 or through region 2, and where the  $e$  photon uses the other crossing. Substitution of these two cases ( $\vec{q}_o = \vec{q}_1$  and  $\vec{q}_e = \vec{q}_2$ ) and ( $\vec{q}_o = \vec{q}_2$  and  $\vec{q}_e = \vec{q}_1$ ) in Eq. (3.2) produces what might be called the “truncated biphoton wave function”

$$|\Psi\rangle = \int d\vec{q}_1 d\vec{q}_2 d\omega_1 d\omega_2 \{ \Phi_{\text{HV}}(\vec{q}_1, \omega_1; \vec{q}_2, \omega_2) |H_1, \vec{q}_1, \omega_1; V_2, \vec{q}_2, \omega_2\rangle + \Phi_{\text{VH}}(\vec{q}_1, \omega_1; \vec{q}_2, \omega_2) |V_1, \vec{q}_1, \omega_1; H_2, \vec{q}_2, \omega_2\rangle \}, \quad (3.8)$$

where the integration over the wave vectors  $\vec{q}_1$  and  $\vec{q}_2$  is now confined (“truncated”) to the two mentioned crossing regions. The two different photon paths introduced above can be clearly distinguished via the threefold labelling of the photon states, with forms like  $|H_1, \vec{q}_1, \omega_1\rangle$ . The corresponding subscripts HV and VH of the function  $\Phi$  [defined in Eq. (3.3)] are necessary, because of a generally different phase mismatch  $\phi$  of the two paths; this so-called “walk-off” is described in more detail in Section 3.3.3. The polarization directions  $H$  and  $V$  are defined with respect to the axes of the generating crystal and correspond to  $o$  and  $e$  polarizations, respectively.

We have chosen the notation of Eq. (3.8) to resemble the “simplified” state of Eq. (3.1). If the biphoton state amplitude functions obey the simple proportionality  $\Phi_{\text{HV}}(\vec{q}_1, \omega_1; \vec{q}_2, \omega_2) \approx \exp(i\alpha)\Phi_{\text{VH}}(\vec{q}_1, \omega_1; \vec{q}_2, \omega_2)$  within the detection area and bandwidth, the integration in Eq. (3.8) can be factorized and the state can effectively be described by Eq. (3.1). This happens in the so-called thin-crystal limit, where the phase mismatch  $\phi = \Delta kL/2$  is simply set to zero.

### 3.2.5 Coincidence detection rate for polarization entanglement

To determine whether the state Eq. (3.8) is an entangled state experimentally, using a setup like in Fig. 3.1, one measures the coincidence rate  $R(\{\chi_i\})$  of simultaneous detection of

two photons by detectors 1 and 2 as a function of some parameters  $\{\chi_i\}$ . In the case of polarization entanglement, where the frequency and wave vectors are fixed within a certain bandwidth, the parameters are the angles  $\varphi_1$  and  $\varphi_2$  of two polarizers in front of the detectors. To derive the theoretical coincidence rate for polarization-sensitive detection, it is convenient to first introduce the “biphoton amplitude function”

$$A_{ij}(\vec{q}_1, \omega_1; \vec{q}_2, \omega_2) \equiv \langle 0 | E_{1,i}^+(\vec{q}_1, \omega_1) E_{2,j}^+(\vec{q}_2, \omega_2) | \Psi \rangle, \quad (3.9)$$

where  $i, j = H, V$  are labels for the optical polarization in the beams 1 and 2, respectively [34]; the coincidence rate will be proportional to the absolute square of  $A_{ij}$ . Furthermore, we define the  $2 \times 2$  biphoton polarization density matrix as

$$\hat{\rho} = \text{Tr}_{\vec{q}_1, \vec{q}_2, \omega_1, \omega_2} (|\Psi\rangle \langle \Psi|) = \begin{pmatrix} \langle\langle |A_{HV}|^2 \rangle\rangle & \langle\langle A_{HV} A_{VH}^* \rangle\rangle \\ \langle\langle A_{VH} A_{HV}^* \rangle\rangle & \langle\langle |A_{VH}|^2 \rangle\rangle \end{pmatrix}, \quad (3.10)$$

where the symbols  $\langle\langle \rangle\rangle$  denote the frequency and spatial integration of the trace operation. Noting that the optical fields transmitted by a polarizer are projected via

$$E_{\text{projected}} = E_H \cos \varphi + E_V \sin \varphi, \quad (3.11)$$

we can write the polarization-projected coincidence rate  $R(\varphi_1, \varphi_2)$  in terms of the polarization density matrix as

$$R(\varphi_1, \varphi_2) = \begin{pmatrix} \cos \varphi_1 \sin \varphi_2 \\ \sin \varphi_1 \cos \varphi_2 \end{pmatrix} \hat{\rho} \begin{pmatrix} \cos \varphi_1 \sin \varphi_2, \sin \varphi_1 \cos \varphi_2 \end{pmatrix}. \quad (3.12)$$

In the above description the complications associated with the six-fold integration over the frequency and spatial coordinates  $(\vec{q}_1, \omega_1; \vec{q}_2, \omega_2)$  are neatly hidden in the double brackets  $\langle\langle \rangle\rangle$ . For further calculations we first have to specify the exact meaning of this symbol, which operates on combinations of the form  $A_{ij}(\vec{q}_1, \omega_1; \vec{q}_2, \omega_2) A_{kl}^*(\vec{q}_1, \omega_1; \vec{q}_2, \omega_2)$ , but for convenience will be specified only for the shorthand form  $|A(\vec{q}_1, \omega_1; \vec{q}_2, \omega_2)|^2$ . We assume that the spatial selection in both beams is performed with apertures positioned in the far-field of the SPDC source that are fully imaged onto the detectors. This allows us to interpret the variables  $\vec{q}_i$  either as a transverse momentum or as an angular position. Furthermore, the frequency selection is performed by interference filters with intensity transmissions  $T_i(\omega)$  in front of the detectors. In this case the double bracket should be interpreted as

$$\langle\langle |A(\vec{q}_1, \omega_1; \vec{q}_2, \omega_2)|^2 \rangle\rangle = \int \int d\omega_1 d\omega_2 \int \int d\vec{q}_1 d\vec{q}_2 T_1(\omega_1) T_2(\omega_2) |A(\vec{q}_1, \omega_1; \vec{q}_2, \omega_2)|^2, \quad (3.13)$$

where the spatial integrals run only over the angular coordinates of the two apertures. In case of continuous-wave excitation, it is convenient to introduce the combined transmission function  $\mathcal{T}(\delta\omega_1) \equiv T_1(\Omega + \delta\omega_1) T_2(\Omega - \delta\omega_1)$ . If the two filters are identical ( $T_1(\omega) = T_2(\omega)$ ),  $\mathcal{T}(\delta\omega_1)$  is symmetric even if the filter characteristics themselves are not.



### 3.3 The degree of polarization entanglement

#### 3.3.1 The concurrence and related measures

In the literature various different parameters are used to quantify the degree of entanglement of mixed states [35]. We will use the so-called concurrence  $P$  as the "degree of polarization entanglement" [35]. This parameter lies between 0 and 1, where a state with  $P = 1$  is perfectly entangled, and a state with  $P = 0$  is nonentangled, i.e., a product state. If the biphoton amplitude functions  $A_{ij}$  obey the relation  $\langle\langle |A_{HV}|^2 \rangle\rangle = \langle\langle |A_{VH}|^2 \rangle\rangle$  (see below), we can express the concurrence as:

$$P = \frac{|\langle\langle A_{HV} A_{VH}^* \rangle\rangle|}{\langle\langle |A_{HV}|^2 \rangle\rangle}, \quad (3.14)$$

and the polarization density matrix as

$$\hat{\rho} = \langle\langle |A_{HV}|^2 \rangle\rangle \begin{pmatrix} 1 & P e^{-i\bar{\alpha}} \\ P e^{i\bar{\alpha}} & 1 \end{pmatrix}, \quad (3.15)$$

with the average phase  $\bar{\alpha} = \text{Arg} \langle\langle A_{HV} A_{VH}^* \rangle\rangle$ . This expression for  $\hat{\rho}$  has the form of the expected density matrices for pure and mixed states, for corresponding values of  $P$  [35].

The relation  $\langle\langle |A_{HV}|^2 \rangle\rangle = \langle\langle |A_{VH}|^2 \rangle\rangle$  is certainly valid in the ideal experimental setup, where (i) the pump beam is planar or symmetrically focused, (ii) spatial selection is centered around the two crossings of the frequency degenerate SPDC rings, and (iii) frequency selection is performed with identical filters in both beams. It is, however, also valid under less stringent symmetry conditions, such as spatial selection in a way that is invariant under reflection in a plane through the (center of the) pump beam and the crystalline optic axis.

Note that, even in the ideal experimental setup, the SPDC state of Eq. (3.8) generally has  $P < 1$ , because the functions  $A_{HV}$  and  $A_{VH}$  are not identical. The most important difference between these functions is a phase factor in the approximate form  $\Phi_{HV} \approx e^{i\beta} \Phi_{VH}$ , with in general  $\beta = \beta(\vec{q}_1, \omega_1; \vec{q}_2, \omega_2)$ . The physical explanation for this phase factor is the birefringence of a type-II SPDC crystal, which is a consequence of the crystal symmetry that is necessary for the SPDC process to occur. This birefringence causes the so-called walk-off, both longitudinal (a relative shift in time) and transverse (a relative shift in position), between the  $o$  and  $e$ -polarized photons as they emerge from the crystal. In an intuitive picture, the walk-off provides for an additional labelling of the individual photons in a pair, which causes a reduction of the degree of polarization entanglement. There is a way to compensate for this walk-off, using additional birefringent optical elements, that will be discussed in the next section.

An experimentally used measure for the degree of entanglement is the so-called biphoton fringe visibility  $V_{\varphi_1}$ , defined as

$$V_{\varphi_1} \equiv \frac{R_{\max} - R_{\min}}{R_{\max} + R_{\min}}. \quad (3.16)$$

This quantity expresses the relative modulation depth of the sinusoidal interference fringe in the biphoton coincidence rate  $R(\varphi_1, \varphi_2)$  that is measured when the polarizer of detector 1 is kept fixed at  $\varphi_1$  while  $\varphi_2$  is varied. The quantities  $R_{\max}$  and  $R_{\min}$  are the maximum and minimum observed rates, respectively. Note that for the state of Eq. (3.8)  $V_{0^\circ} = V_{90^\circ} = 1$ ,

because for the corresponding settings of polarizer 1 there is no interference between the  $A_{HV}$  and the  $A_{VH}$  terms, cf. Eq. (3.12). The visibilities  $V_{45^\circ}$  and  $V_{135^\circ}$  are however in general smaller than 1. Furthermore, when the average phase  $\bar{\alpha} = 0$  or  $\bar{\alpha} = \pi$ , these visibilities are equal to the concurrence, i.e  $V_{45^\circ} = V_{135^\circ} = P$ . Note, that the average phase  $\bar{\alpha}$  can be set experimentally using the same additional birefringent optical elements that are used to correct walk-off effects; this will be discussed in the next section.

Another parameter that is sometimes used to characterize the quality of entangled-photon sources is the Bell parameter  $S$  [20]. However, this quantity is much more than a measure for the degree of entanglement alone, because it can provide, via the associated Bell inequality, a distinction between (nonlocal) quantum-mechanical behavior from (local) classical behavior [14, 20, 36]. We discuss the Bell parameter here because we use it in Chapter 4. In the CHSH variant, and using the fair-sampling assumption, the Bell parameter is given by [20, 37, 38]

$$S = |E(\varphi_1, \varphi_2) - E(\varphi'_1, \varphi_2) + E(\varphi_1, \varphi'_2) + E(\varphi'_1, \varphi'_2)|, \quad (3.17)$$

with

$$E(\varphi_1, \varphi_2) \equiv \frac{R(\varphi_1, \varphi_2) + R(\varphi_1^\perp, \varphi_2^\perp) - R(\varphi_1, \varphi_2^\perp) - R(\varphi_1^\perp, \varphi_2)}{R(\varphi_1, \varphi_2) + R(\varphi_1^\perp, \varphi_2^\perp) + R(\varphi_1, \varphi_2^\perp) + R(\varphi_1^\perp, \varphi_2)}, \quad (3.18)$$

and where we immediately expressed the measurement probabilities in terms of the coincidence rate  $R$  as defined above. For systems conforming to local-realistic theories (including hidden-variable theories)  $0 \leq S \leq 2$ . For the quantum system described by the entangled (and therefore nonlocal) state of Eq. (3.1), the strongest violation of the Bell inequality occurs for settings of the polarizers at  $\phi_1 = -\pi/8$ ,  $\phi'_1 = \pi/8$ ,  $\phi_2 = -\pi/4$  and  $\phi'_2 = 0$  [20]. In this case, the Bell parameter is equal to  $S = \sqrt{2}(V_{0^\circ} + V_{45^\circ}) = \sqrt{2}(1 + V_{45^\circ})$ , which shows that here  $S$  is just a sort of “average” visibility [39]. It has a maximal value of  $2\sqrt{2}$  for a perfectly entangled state. Note, that the second equality holds for the state of Eq. (3.2), but the first equality holds as well for the most general state which also has  $|HH\rangle$  and  $|VV\rangle$  pairs.

We will now calculate the concurrence for the case of monochromatic plane-wave pumping, both without and with walk-off compensation.

### 3.3.2 Concurrence without walk-off compensation

For monochromatic plane-wave pumping conservation of energy (=frequency) and transverse momentum introduce  $\delta$ -functions in the equations for the four elements of the polarization density matrix:

$$A_{ij}A_{kl}^* \propto L^2 \text{sinc}(\phi_{ij}) \text{sinc}(\phi_{kl}) \times e^{i(\phi_{ij} - \phi_{kl})} \delta(\vec{q}_1 + \vec{q}_2) \delta(\omega_1 + \omega_2 - \omega_p), \quad (3.19)$$

where  $ij, kl = HV$  or  $VH$ . Here the pump, at frequency  $\omega_p \equiv 2\Omega$ , enters the crystal at normal incidence with transverse momentum  $\vec{q}_p = \vec{0}$ . Close to frequency degeneracy we can write  $\vec{q}_i \approx \vec{\theta}_i(\Omega/c)$ , where we define  $\vec{\theta}_i \equiv (\theta_{i,x}, \theta_{i,y})$ , and use the  $\delta$ -relations by taking  $\vec{\theta}_2 \approx -\vec{\theta}_1$  and  $\delta\omega_1 \approx -\delta\omega_2$ . In the absence of compensating birefringent optical elements the concurrence [Eq. (3.14)] can then be written as

$$P = \frac{|\int \int \int d\delta\theta_{1,x} d\theta_{1,y} d\delta\omega_1 \mathcal{T}(\delta\omega_1) \text{sinc}(\phi_{HV}) \text{sinc}(\phi_{VH}) \exp(i\{\phi_{HV} - \phi_{VH}\})|}{\int \int \int d\delta\theta_{1,x} d\theta_{1,y} d\delta\omega_1 \mathcal{T}(\delta\omega_1) \text{sinc}^2(\phi_{HV})}. \quad (3.20)$$

Note, that we again assumed  $\langle\langle |A_{HV}|^2 \rangle\rangle = \langle\langle |A_{VH}|^2 \rangle\rangle$ , which is equivalent to  $\langle\langle \mathcal{T}(\delta\omega_1) (\text{sinc}^2(\phi_{HV}) - \text{sinc}^2(\phi_{VH})) \rangle\rangle = 0$ . This holds when  $\mathcal{T}(\delta\omega_1)$  and the  $\delta\omega_1$ -integration range are symmetric around  $\delta\omega_1 = 0$ , and when the  $(\delta\theta_{1,x}, \theta_{1,y})$ -integration range is inversion-symmetric in either  $\theta$  axis, as mentioned before.

The 3-fold integrals in Eq. (3.20) are in general hard to solve. They are manageable, however, in the limit of good entanglement  $P \approx 1$ , where we can perform a Taylor expansion of the exponential and sinc functions around  $\phi_{ij} = 0$ . Furthermore, we can use the linearization of the phase mismatch functions given in Eq. (3.7) to write:

$$\phi_{HV}(\vec{\theta}_1, \vec{\theta}_2; \delta\omega_1) \equiv \Delta k_{HV} L/2 = -\frac{\pi\delta\omega_1}{\Delta\omega_{\text{SPDC}}} + \frac{\pi}{\Delta\theta_{\text{SPDC}}} (\delta\theta_{1,x} + \theta_{1,y}), \quad (3.21)$$

$$\phi_{VH}(\vec{\theta}_1, \vec{\theta}_2; \delta\omega_1) \equiv \Delta k_{VH} L/2 = \frac{\pi\delta\omega_1}{\Delta\omega_{\text{SPDC}}} + \frac{\pi}{\Delta\theta_{\text{SPDC}}} (\delta\theta_{1,x} - \theta_{1,y}), \quad (3.22)$$

where we substituted  $(1 = H = o)$  and  $(1 = V = e)$  in Eq. (3.7), respectively.

Using the foregoing expansions, we calculate the concurrence, valid up to second order in the variables, for filters with a “top-hat” spectral transmission profile, of full width  $\Delta\omega_{\text{filter}}$  centered around  $\Omega$ , and for square spatial-selection apertures, which span full angles  $\Delta\theta_{\text{aperture}}$  in both  $x$  and  $y$  direction. This yields

$$P \approx 1 - \frac{\pi^2}{6} \left( \frac{\Delta\omega_{\text{filter}}}{\Delta\omega_{\text{SPDC}}} \right)^2 - \frac{\pi^2}{6} \left( \frac{\Delta\theta_{\text{aperture}}}{\Delta\theta_{\text{SPDC}}} \right)^2. \quad (3.23)$$

Note, that the terms in this expansion originate from the phase factor of Eq. (3.19); the sinc terms cancel each other and contribute only in fourth and higher order. For other types of filters and apertures the general form of Eq. (3.23) remains intact, but the pre-factors change. For instance, for matched filters with Gaussian transmission profiles of full width  $\Delta\omega_{\text{filter}}$  and circular apertures of diameter  $\Delta\theta_{\text{aperture}}$  one finds

$$P \approx 1 - \frac{\pi^2}{8 \ln 2} \left( \frac{\Delta\omega_{\text{filter}}}{\Delta\omega_{\text{SPDC}}} \right)^2 - \frac{\pi^2}{8} \left( \frac{\Delta\theta_{\text{aperture}}}{\Delta\theta_{\text{SPDC}}} \right)^2, \quad (3.24)$$

Note that  $8 \ln 2 \approx 5.5$  is close to the value of 6 found for top-hat filters. Also note that spatial labeling is less severe with circular apertures than with square apertures as  $\pi^2/8 < \pi^2/6$ .

The obtained expansions quantify some of the practical limitations of using type-II SPDC as a polarization-entanglement source. Although it is in principle possible to generate perfectly polarization-entangled photons, the required limits  $\Delta\omega_{\text{filter}} \rightarrow 0$  and  $\Delta\theta_{\text{aperture}} \rightarrow 0$  are not very practical because they will nullify the biphoton yield. An experimentalist will therefore always search for a compromise between biphoton yield and the degree of polarization entanglement.

### 3.3.3 Concurrence with walk-off compensation

As discussed in Section 3.2.4, the physical reason for the reduced degree of entanglement  $P$  with increased detection bandwidth or increased aperture size lies in the possibility (if only theoretically) to determine the photon polarization from either its time of arrival, via the

longitudinal walk-off, or its position at the exit facet of the crystal, via the transverse walk-off. From this perspective, the frequency filters and apertures both act as quantum erasers; narrow filters and tight apertures are able to erase both the time and position “labelling” that was originally present in the generated biphoton field.

The mathematical reason for the entanglement reduction with increased detection bandwidth or aperture size is the different dependence of the amplitude functions  $\Phi_{HV}$  and  $\Phi_{VH}$  on frequency and angle. This argument is of course Fourier-related to the time and position labelling mentioned above. In the Taylor expansion of Eq. (3.20) we noted that the exponential factors change more rapidly than the sinc-factors. The degree of entanglement  $P$  would thus increase considerably if we could remove the exponential factors, or at least make them equal for the  $HV$  and  $VH$  combinations. Experimentally, this is not too difficult: in a standard compensation scheme, both SPDC beams are first passed through a  $\lambda/2$  plate oriented at  $45^\circ$ , to swap the emitted  $H$  and  $V$  polarizations. The beams 1 and 2 are then passed through birefringent crystals of length  $L_1$  and  $L_2$ , which we will consider, for ease of calculation, to be of the same material and orientation as the generating crystal. The crystals add frequency- and angle-dependent phase factors in the relation between the biphoton wave function  $\Phi_{ij}$  and the detected biphoton fields  $A_{ij}$ :

$$A_{ij}(\vec{q}_1, \omega_1; \vec{q}_2, \omega_2) \propto \Phi_{ij}(\vec{q}_1, \omega_1; \vec{q}_2, \omega_2) \times e^{-i\beta_{ij}(\vec{q}_1, \omega_1; \vec{q}_2, \omega_2)}. \quad (3.25)$$

For the concurrence of the compensated state only the phase difference  $\beta_{HV} - \beta_{VH}$  is important. In a first-order Taylor expansion of the frequency  $\omega_1 = \Omega \pm \delta\omega$  and the momentum  $\vec{q}_1 = (\Omega/c)\vec{\theta}_1$  of the incident SPDC light (and  $\delta\omega_2 = -\delta\omega_1$  and  $\theta_2 = -\theta_1$  for the other beam), we can write:

$$\beta_{HV} - \beta_{VH} \approx (\beta_1^0 - \beta_2^0) + (\beta_1^\omega + \beta_2^\omega)\delta\omega_1 - (\beta_1^\theta + \beta_2^\theta)\theta_{1,y} \quad (3.26)$$

where we used again  $\delta\omega_2 = -\delta\omega_1$  and  $\delta\theta_{2,y} = -\delta\theta_{1,y}$ .

This first-order expansion explicitly shows the presence of three contributions. The “constant” term  $\beta_j^0 = [n_o - n_e(\Theta_C + \theta_{\text{tilt}}/n_e(\Theta_C))]\Omega L_j/c$  is the birefringent phase delay at  $\theta_y = 0$  and  $\delta\omega = 0$ . It dominantly determines the average phase  $\bar{\alpha}$  in Eq. (3.15) [or  $\alpha$  in the approximate state Eq. (3.1)], because  $\beta_j^0 \gg 1$  for many practical crystal lengths. By varying the tilt angle  $\theta_{\text{tilt}}$  slightly,  $\alpha$  can be easily set to any desired value from 0 to  $2\pi$ . The other terms  $\beta_j^\omega = [n_{o,gr} - n_{e,gr}(\Theta_C + \theta_{\text{tilt}}/n_e(\Theta_C))]\Omega L_j/c$  and  $\beta_j^\theta = \Omega \rho(\Theta_C + \theta_{\text{tilt}}/n_e(\Theta_C))L_j/c$  quantify the frequency- and angle-dependence of the phase difference. Both these terms are crucial for the compensation scheme because they can be used to “erase” the differences in frequency and angular-dependence of the biphoton fields  $A_{HV}$  and  $A_{VH}$ . A Fourier transformation of Eq. (3.26) shows more clearly the physical principle behind this compensation. The frequency-dependent phase introduced by  $\beta_j^\omega$  corresponds to a time delay of one polarized field component with respect to the other. The angle-dependent term  $\beta_j^\theta$  corresponds to a spatial shift in the  $y$ -direction of one polarized field component with respect to the other.

When the combined length of the compensating crystals  $L_1 + L_2 = L$  the compensation is perfect and the phase factors of  $A_{HV}$  and  $A_{VH}$  become identical. When  $L_1 + L_2 \neq L$  a fraction  $1 - (L_1 + L_2)/L$  of the original relative phase factor remains. When we single out the effect

of this remaining phase factor on the degree of polarization we have to modify Eq. (3.24) into

$$P \approx 1 - \frac{\pi^2}{8 \ln 2} \left( \frac{L - L_1 - L_2}{L} \right)^2 \left( \frac{\Delta \omega_{\text{filter}}}{\Delta \omega_{\text{SPDC}}} \right)^2 - \frac{\pi^2}{8} \left( \frac{L - L_1 - L_2}{L} \right)^2 \left( \frac{\Delta \theta_{\text{aperture}}}{\Delta \theta_{\text{SPDC}}} \right)^2. \quad (3.27)$$

The two pre-factors that originate from imperfect compensation can be fine-tuned somewhat via the refractive index  $n_e(\Theta)$  and walk-off angle  $\rho(\Theta)$  by tilting the compensating crystals in the y-direction. The compensation for longitudinal walk-off can be fine-tuned pretty easily because  $n_{e,gr}(\Theta)$  changes considerably with angle (see Appendix, Eq. (3.29)). The compensation for transverse walk-off changes much less rapidly because we are generally close to an extremum of  $\rho(\Theta)$  at typical angles of  $\Theta \approx 45^\circ$  (see Appendix, Eq. (3.30)).

Even if the birefringence compensation is perfect and the phases of  $A_{HV}$  and  $A_{VH}$  are identical, the concurrence can be nonideal ( $P < 1$ ). This occurs when the integrated amplitudes  $\langle |A_{HV}|^2 \rangle \propto \langle \text{sinc}^2(\phi_{HV}) \rangle$  and  $\langle |A_{VH}|^2 \rangle \propto \langle \text{sinc}^2(\phi_{VH}) \rangle$  differ, i.e. when the aperture sizes are large enough to observe the different shapes of the H and V rings. In this case the positions of the detected photons give partial information on their polarization (spatial labelling), which translates in the inequality  $|A_{HV}| \neq |A_{VH}|$  at these positions. These differences are fourth and higher order in  $\delta \omega_1$  and  $\delta \vec{\theta}_1$ .

### 3.4 Experimental characterization of our SPDC source

#### 3.4.1 Setup and typical experimental numbers

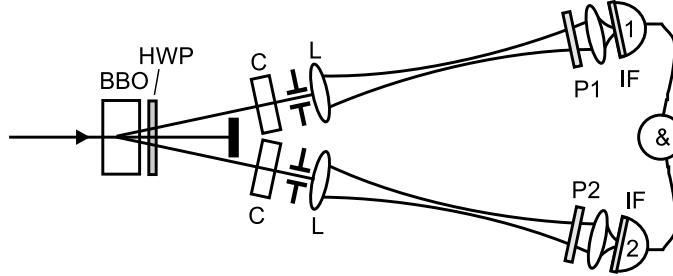


Figure 3.5: *Experimental setup.*

Figure 3.5 shows the detailed experimental setup that was used to generate the polarization-entangled photon pairs. A continuous-wave Kr-ion pump laser, operating at  $\lambda_p = 406.7$  nm, illuminates a  $\chi^{(2)}$ -nonlinear generating crystal made of  $\beta$ -Barium Borate (BBO), typically 1 mm thick and cut at an angle of  $\Theta_c = 41.2^\circ$ . It is followed by the standard quantum eraser that compensates for the birefringent walk-off in the crystal. It comprises a half-wave plate HWP, oriented at  $45^\circ$  with respect to the crystal axes, and two BBO crystals (C) with a thickness equal to approximately half of that of the generating crystal. Spatial selection of the frequency-degenerate crossings is performed by two circular apertures of variable diameter, which are situated in the far field of the generating crystal at approximately 80 cm from the generating crystal. After passing through two adjustable polarizers (P1 and P2), frequency

**Table 3.1:** Experimental numbers for 1 mm-thick BBO

Quantity	Value	Quantity	Value
$\lambda_p$	406.7 nm	$n_{gr,o}(\lambda_{SPDC})$	1.686
$\lambda_{SPDC} = \lambda_e = \lambda_o$	813.4 nm	$n_{gr,e}(\Theta_C, \lambda_{SPDC})$	1.627
$\Theta_C$	41.9°	$\rho(\Theta_C, \lambda_{SPDC})$	4.10°
$n_o(\lambda_{SPDC})$	1.661	$\rho(\Theta_C, \lambda_p)$	4.38°
$n_e(\lambda_{SPDC})$	1.546	$\theta_{off}$	3.35°
$n_e(\Theta_C, \lambda_{SPDC})$	1.607	$\Delta\omega_{SPDC}/\Omega$	0.0138
$n_e(\Theta_C, \lambda_p)$	1.633	$\Delta\theta_{SPDC}$	11.4 mrad
$\langle 1/n \rangle^{-1}$	1.633		

selection is performed by narrow-band interference filters (IF) with a top-hat transmission spectrum centered at  $\lambda_{SPDC} = \lambda_o = \lambda_e = 813.4$  nm. Finally, the two beams are focused onto single-photon counting Avalanche Photo Diodes (PerkinElmer SPCM-AQR-14), which act as bucket detectors, imposing no further transverse mode selection. The signals from the two detectors are combined electronically in a coincidence circuit with a time window that is sufficiently short to isolate individual twin photons, but much longer than the inverse optical bandwidth of the interference filters so that twin photons are practically never separated from one another by the temporal resolution. The lenses L serve to refocus the SPDC light to be able to accommodate further experiments.

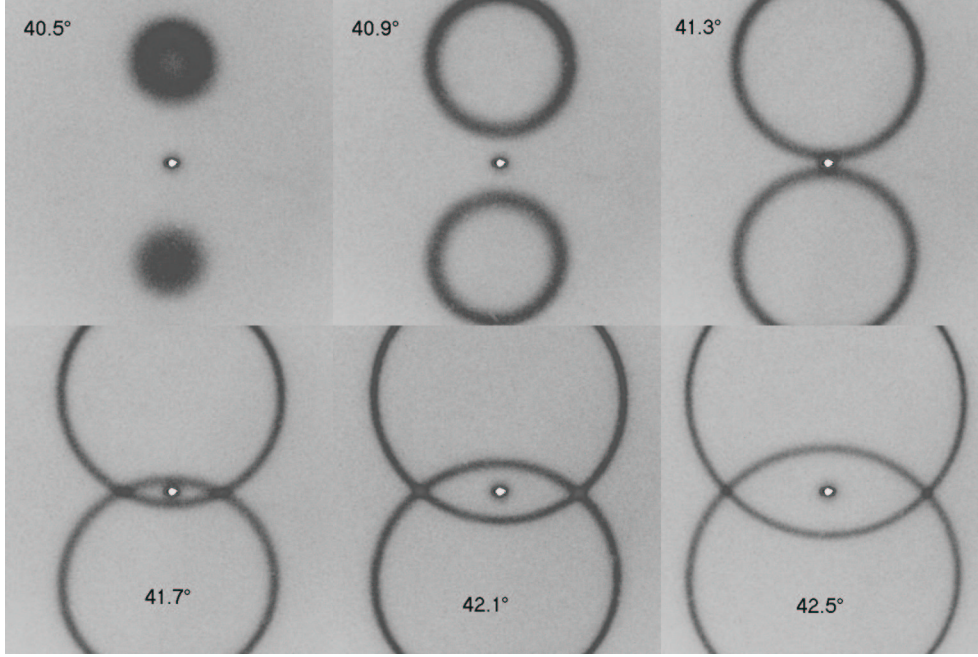
Crucial parameters for the efficiency of this setup and the quality of the produced photon states are, on the generating side, the thickness (and orientation) of the nonlinear crystal, the size of the pumped area, and the amount of compensation. Crucial parameters on the detection side are the amount of frequency selection (filter bandwidth) and the amount of spatial selection (aperture diameters). For optimum performance, the spatial selection should of course be properly centered around the two crossings of the frequency-degenerate SPDC rings.

Table 3.1 gives the relevant optical constants for the setup. From these numbers, we see that the crystal is indeed phase-matched at external angles close to normal incidence. Slight angle tuning of the BBO crystal allows one to fine-tune the SPDC rings for perpendicular crossing, at which point the crossings are positioned at  $\theta_{i,x} = \pm\theta_{off} = \pm 3.35^\circ = \pm 58$  mrad from the pump beam. The SPDC spectral and angular widths are calculated using Eq. (3.5) and Eq. (3.6), respectively. Note that these widths applies only to the case of plane-wave pumping and monochromatic detection. If detection takes place over a finite frequency bandwidth the SPDC rings will be broadened via

$$\Delta\theta_{SPDC} = \left( \frac{d\theta}{d\lambda} \right) \Delta\lambda_{SPDC} = \left( \frac{n_{o,gr} - n_{e,gr}(\Theta_C)}{\rho\lambda_0} \right) \Delta\lambda_{SPDC}. \quad (3.28)$$

A spectral integration over a 10 nm bandwidth will for instance already add 9.1 mrad to the SPDC angular width.

Figure 3.6 a) shows far-field pictures of the SPDC rings as a function of the angle of



**Figure 3.6:** The spatial intensity distribution of the SPDC light as a function of the internal angle of the pump beam with the optic axis of a 2 mm BBO crystal. The pictures span  $5.6^\circ \times 5.6^\circ$  each. The gray scales are different for each picture. The central spot is a residue of the pump laser beam.

incidence of the pump beam on the crystal, observed with an intensified CCD (Princeton Instruments PI-MAX 512HQ with 4-th generation intensifier). A blue-reflecting laser mirror and an interference filter (spectral width 5 nm centered around 813 nm) were used to select the SPDC light. Note how the two SPDC rings change shape considerably over the relatively small angular interval of  $2^\circ$ . This justifies the small-angle approximations used in the preceding theoretical discussions. The rings intersect perpendicularly at a measured internal angle of  $42.3^\circ \pm 0.5^\circ$  with a corresponding offset angle  $\theta_{\text{off}} = 54 \pm 3$  mrad, agreeing nicely with the calculated values of  $41.9^\circ$  and 58 mrad. From a cross section through the observed rings the radial width of the SPDC rings was measured to be  $\approx 5.4$  mrad (FWHM). This value is close to the expected value of  $(5.6 + 4.9)/\sqrt{2}/1.13 = 6.6$  mrad for a 2-mm thick crystal and a 5-nm wide spectral filter. The two terms in the sum reflect the natural width (at fixed frequency) and the extra width due to frequency spreading, and the two correction factors arise from the conversion from  $x/y$  to radial width and from  $\theta_{\text{SPDC}}$  to FWHM.

### 3.4.2 Measured count rates

To characterize the efficiency of our setup, we now discuss the count rates that were typically achieved. These rates depend on the size of the apertures used to select the ring crossings, the bandwidth of the frequency filters and the pump power and pump beam waist at the crystal.

The aperture dependence of the count rates for a mildly-focussed pump beam (FWHM-pump diameter  $280\text{ }\mu\text{m}$  inside the crystal) is shown in Fig. 3.7, where open triangles denote single count rates (s.c.) and open circles denote coincidence count rates (c.c.). A 1 mm thick BBO crystal and 10 nm wide interference filters were used. Note that the coincidence rates have been multiplied by a factor 4 to fit on the same scale. Also shown in Fig. 3.7 is the quantum efficiency (q.e.; open squares) or relative biphoton detection efficiency, which is defined as the conditional probability to detect the second photon out of a pair when the first photon has been detected. The quantum efficiency rises steeply for small apertures to a value of  $\approx 25\%$ . This steep rise is associated with the divergence of the pump laser, which is slightly less than 1 mrad for this case of mild focusing. The gradual decrease in quantum efficiency for larger apertures is probably due to spatial limitations of the imaging optics and bucket detectors.

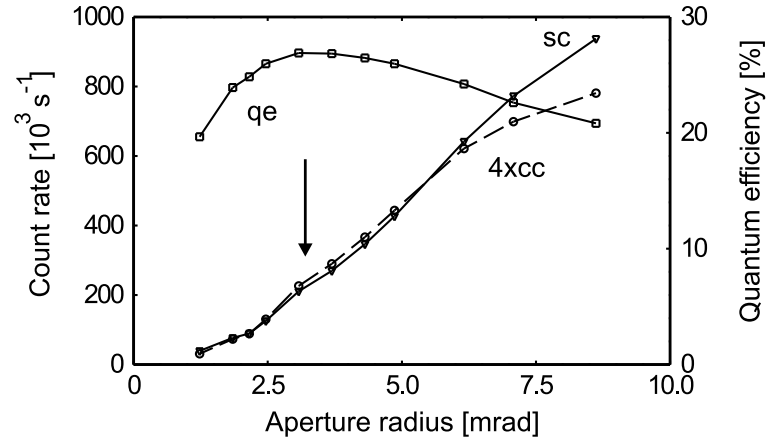


**Figure 3.7:** Measured single count rate (s.c.), coincidence count rate (c.c.), and quantum efficiency  $\eta = \text{c.c.}/\text{s.c.}$ , as a function of the diameter of two apertures situated in the far-field at 80 cm away from the 1 mm thick generating BBO crystal. We used interference filters of 10 nm spectral width and 240 mW of cw pump power at  $\lambda_p = 406.7\text{ nm}$ . The pump laser was mildly focused to a (FWHM) diameter of  $280\text{ }\mu\text{m}$  inside the crystal, corresponding to a far-field angle of slightly less than 1 mrad.

To illustrate the dependence of the count rates and quantum efficiency on the crystal thickness, Fig. 3.8 shows measurements with a 2-mm thick generating BBO crystal and 5 nm wide filters under the same mild-focusing condition used for Fig. 3.7. The coincidence count rate is again multiplied by a factor 4. In spite of the reduced detection bandwidth (from 10 nm to 5 nm, in correspondence with the reduced SPDC bandwidth), the count rates for small apertures are larger for the 2-mm thick BBO than for the 1-mm thick crystal, due to the increased crystal thickness. Note how the turnover from a quadratic to a linear dependence of count rate on aperture size (marked by the arrow) occurs much earlier, thus showing that the angular width of the SPDC rings produced by a 2-mm thick crystal is roughly a factor 2 smaller than that of the 1-mm thick crystal.



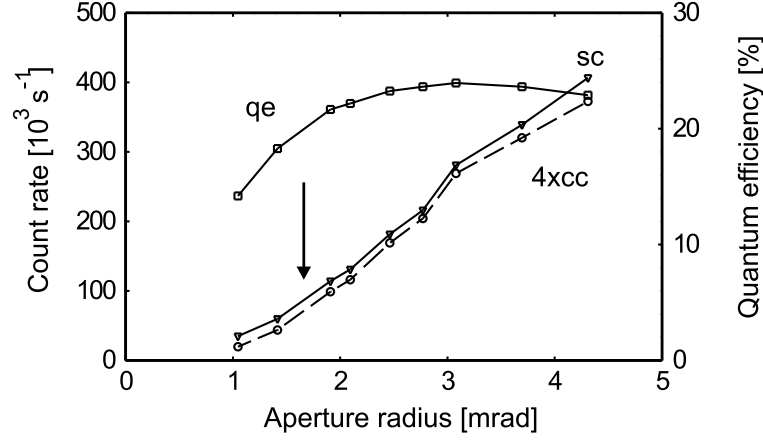


**Figure 3.8:** Similar measurement as in Fig. 3.7, but now for a 2 mm BBO crystal, 5 nm wide filters and (again) a mildly-focused pump laser. The single count rate, coincidence count rate (multiplied by 4), and deduced quantum efficiency are shown as a function of the aperture diameter.

### 3.4.3 Measured degree of quantum entanglement

To illustrate the effects of the birefringent walk-off in the crystal, we give some typical count rates from the setup without the quantum eraser components. For effectively plane-wave pumping (pump focus  $\approx 280 \mu\text{m}$  FWHM) at 240 mW power, in combination with detection behind apertures with 5-mrad diameter ( $\approx 4 \text{ mm}$  at 80 cm from the BBO), we measured a large biphoton visibility in the HV basis ( $V_{0^\circ} > 99.0 \%$ ), but a generally modest visibility in the  $\pm 45^\circ$  basis. For a 1-mm thick BBO crystal we typically obtained  $V_{45^\circ} = 37 \%$  and  $75 \%$  for a detection bandwidth of 10 nm and 5 nm, respectively. For the aperture diameter of 5 mrad that we used, these visibilities are dominantly limited by longitudinal walk-off. Numerical evaluation of the integrals in Eq. (3.20) gives  $P = 36.4 \%$  and  $64.3 \%$ , respectively, for the two spectral bandwidths; the experimental result for the 5-nm filters is probably so large because the center wavelength of these filters was slightly misplaced, making the combination of two filters effectively narrower [40]. Increasing the aperture diameter decreased the visibility only mildly from the mentioned  $37 \%$  at 5 mrad to  $\approx 20 \%$  at 19 mrad apertures, using the 10-nm wide spectral filter. A 2-mm thick BBO crystal gave  $V_{45^\circ} = 49 \%$  for 5-nm wide detection bandwidth [40]. For a crystal as thin as  $50 \mu\text{m}$  we found  $V_{45^\circ} = 99.3 - 98.9 \%$  (upon an increase of aperture diameter from 5 to 19 mrad) even for the 10 nm interference filters, in nice agreement with the calculated values of  $P = 99.6 - 98.9 \%$ . This is consistent with the statement that walk-off effects are very small in such a thin crystal. Typical coincidence rates for detection behind the 10 nm filters were  $3 \times 10^4 \text{ s}^{-1}$  and  $90 \text{ s}^{-1}$  for the 1 mm and  $50 \mu\text{m}$  thick BBO, respectively, a difference of roughly a factor  $20^2 = 400$ . This shows that thin crystals, although they intrinsically have small walk-off effects, are unpractical as a source because they have too low a yield.

By inserting the quantum eraser components, namely the half-wave plate and the two other crystals C, we are able to compensate for the walk-off (i.e., eliminate the second-order

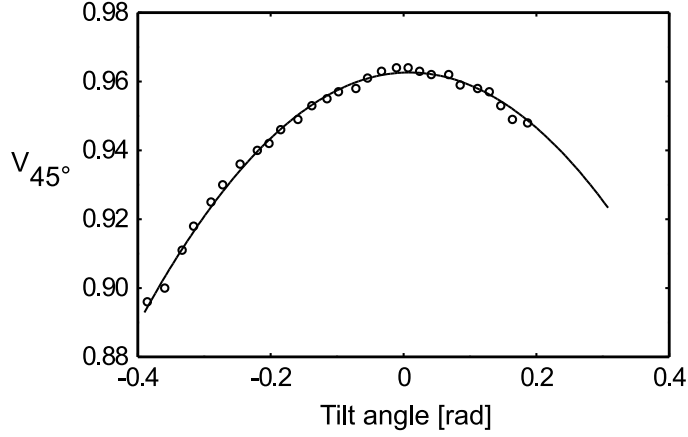


**Figure 3.9:** Measured visibility  $V_{45^\circ}$  as a function of the tilt angle of one of the compensating crystals.

terms of Eq. (3.27)) and to approach  $V_{45^\circ} = 1$  (and  $P = 1$ ). Because the thicknesses of the compensating crystals were not precisely half that of the generating crystal, we had to fine-tune the (horizontal) angle of their optic axis with respect to the incident SPDC beams. The result of this angle tuning is depicted in Fig. 3.9, which shows the measured visibility  $V_{45^\circ}$  as a function of the angle of one of the compensating crystals for 5-mrad diameter apertures and 10-nm bandwidth frequency filters. The fitted curve is based on a sixth-order expansion of Eq. (3.20), including as a variable the compensating-crystal tilt angle (or effective length mismatch  $L - L_1 - L_2$ ). From the transverse walk-off observed under a microscope we estimate  $L = 1.0$  mm,  $L_1 = 0.50$  mm and  $L_2 = 0.46$  mm (within 10%). The coefficients correspond to values of  $\Delta\omega_{\text{filter}} = 11$  nm,  $\Delta\theta_{ap} = 6.7$  mrad, which are in reasonable agreement with the experimental values; the peak visibility of 96.2 % is less than the theoretical maximum of 100 % due to the finite size of the apertures. (In a second run we were able to achieve  $V_{45^\circ} = 97.8\%$  as a maximum for the same aperture diameter and filters). The performance of the total system is not extremely sensitive to the exact orientation of the compensating elements, being the half-wave plate (oriented at  $45^\circ$ ) and the two compensating crystals (oriented in the same direction as the generating crystal). The visibility  $V_{45^\circ}$  was found to change quadratically with the various misorientation angles, where a rotation of the half-wave plate over  $1^\circ$  lead to a reduction of  $V_{45^\circ}$  by only 0.6 %.

Even for perfect birefringent compensation the degree of entanglement  $P$  can be smaller than 1 if the apertures are opened up. This is illustrated in Fig. 3.10, which shows the visibility  $V_{45^\circ}$  and  $V_{135^\circ}$  as a function of the diameter of two apertures centered around the frequency-degenerate crossings of the SPDC rings produced by a 1 mm thick BBO crystal and detected in a 10 nm bandwidth around frequency degeneracy. The solid data points show the results for two different 1 mm thick crystals under mildly-focused pumping, while the open symbols show the results for stronger focusing ( $\Delta\theta_p = 8$  mrad). Note that focused pumping hardly changes the visibility, while it does have a strong effect on the coincidence rate and quantum efficiency (see Fig. 3.7). The solid curve is a theoretical fit (through the solid dots) based on a simple quadratic dependence with equation  $V = -2.84 \times 10^4 (\Delta\theta)^2 + 0.993$ . For a 2-mm

thick crystal we measured a similar quadratic behavior within half the angular range. We understand this scaling, but do not yet understand why the quadratic fit is so good.

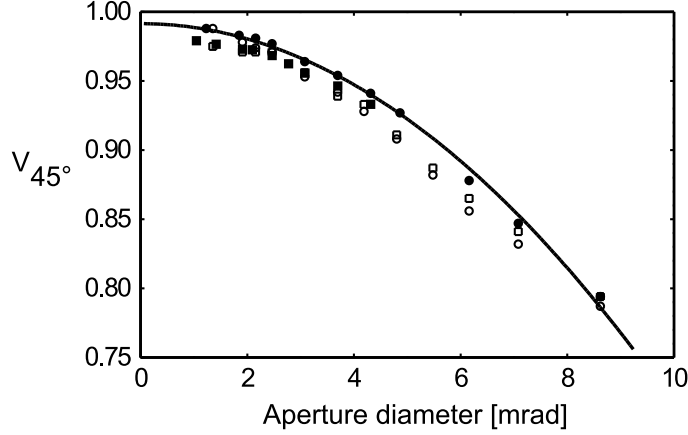


**Figure 3.10:** Visibility  $V_{45^\circ}$  and  $V_{135^\circ}$  versus the aperture diameter, under conditions similar to Figs. 3.7 and 3.8. The solid symbols correspond to mildly-focused pumping, the open symbols correspond to strong focusing. The solid curve is a theoretical fit (through the solid dots) based on a simple quadratic dependence.

### 3.5 Conclusions

We have given a theoretical and experimental description of a SPDC source for polarization-entangled photons. We have shown that quantum states with almost perfect entanglement can be produced if the proper correction for the birefringence of the source is applied and if the spatial- and frequency- detection bandwidths are kept small enough. As a convenient compromise between entanglement quality and biphoton yield we often worked with a 1-mm thick BBO crystal, a 10-nm wide detection bandwidth and 5-mrad diameter apertures. Under these conditions we typically obtain  $V_{0^\circ} = 99.6$ ,  $V_{45^\circ} = 97.4$  at a coincidence rate of  $30 \times 10^3 \text{ s}^{-1}$  for a 200-mW pump power.

## Appendix

### 3.A Phase matching in type-II SPDC

In this appendix we consider the issue of “phase matching” that governs the generation of SPDC light in crystals of finite length. Phase matching is determined by the geometry and the optical properties of the generating crystal. The linear optical properties of uniaxial bire-

fringent crystals are basically contained in a single equation [41]:

$$\frac{1}{n_e(\Theta, \omega)} = \sqrt{\frac{\sin^2 \Theta}{n_e^2(\omega)} + \frac{\cos^2 \Theta}{n_o^2(\omega)}} , \quad (3.29)$$

which denotes the refractive index of  $e$ -polarized rays propagating in the plane containing the optic axis of the crystal, at an internal angle  $\Theta$  with respect to the optic axis. In this equation  $n_o$  and  $n_e$  are the principal refractive indices at optical frequency  $\omega$  for  $o$  and  $e$  polarization, respectively. Note, that we will mostly suppress the  $\omega$  dependence in our notation.

For the  $e$ -polarized rays, the Poynting vector  $\vec{S} \propto \vec{E} \times \vec{H}$  (= direction of energy flow) is oriented in a different direction than the wavevector  $\vec{k} \propto \vec{D} \times \vec{H}$ , which is along the propagation direction of  $o$ -polarized rays. The angle between  $\vec{S}$  and  $\vec{k}$  is the so-called (internal) walk-off angle, which is given by [41] as

$$\rho(\Theta) = -\frac{1}{n_e(\Theta)} \frac{\partial n_e(\Theta)}{\partial \Theta} = \arctan\left(\frac{n_o^2}{n_e^2} \tan \Theta\right) - \Theta = n_e(\Theta)^2 \left(\frac{1}{n_e^2} - \frac{1}{n_o^2}\right) \sin \Theta \cos \Theta . \quad (3.30)$$

The associated external offset angle is given by

$$\theta_{\text{off}} \equiv \frac{1}{2\langle 1/n \rangle} \rho(\Theta) , \quad (3.31)$$

$$\langle 1/n \rangle \equiv \frac{1}{2n_o} + \frac{1}{2n_e(\Theta)} . \quad (3.32)$$

For negative uniaxial crystals ( $n_e < n_o$ ) the beam walk-off is away from the optic axis as  $\rho_{\text{off}}(\Theta) > 0$  (see Fig. 3.3).

We now consider a geometry in which a monochromatic, but not necessarily planar, pump laser is incident on a uniaxial crystal that is cut in such a way that the optic axis makes an angle  $\Theta_c$  with the surface normal [denoted as the  $z$ -axis, see Fig. 3.3(b)]. To evaluate the wavevector mismatch along the surface normal, we use the paraxial approximation to expand the  $z$ -components of the various wave vectors to first order in the optical frequency  $\omega$  and to second order in the *external* angles of incidence  $\theta_x$  and  $\theta_y$  ( $\theta_x, \theta_y \ll 1$ ). Because the planar pump is allowed to make a small angle with the surface normal, the ( $z$ -component of the) wavevector mismatch is generally a complicated function of the form  $\Delta k(\vec{q}_o, \omega_o; \vec{q}_e, \omega_e; \vec{q}_p, \omega_p) = k_{p,z} - k_{o,z} - k_{e,z}$ .

For the  $o$ -polarized SPDC ray, at optical frequency  $\omega = \Omega - \delta\omega_e$  ( $\delta\omega_e \ll \Omega$ ), expansion yields

$$k_{o,z} \approx n_o(\omega) \frac{\omega}{c} \cos\left(\frac{\theta_{o,x}}{n_o}\right) \cos\left(\frac{\theta_{o,y}}{n_o}\right) \approx n_o(\Omega) \frac{\Omega}{c} - n_{o,gr}(\Omega) \frac{\delta\omega_e}{c} - \frac{\Omega}{c} \frac{1}{2n_o(\Omega)} (\theta_{o,x}^2 + \theta_{o,y}^2) , \quad (3.33)$$

where  $\Omega = \omega_p/2$  is the SPDC center frequency, being half the pump frequency, and where  $n_{o,gr}$  is the group refractive index of the  $o$ -polarized SPDC ray (at the optical frequency  $\Omega$ ).

For the  $e$ -polarized SPDC ray, at frequency  $\omega_e = \Omega + \delta\omega_e$ , the expansion is slightly more complicated, because it involves both the frequency and the angle dependence of the

associated refraction index  $n_e(\Theta, \omega)$ . For the geometry of Fig. 3.3, with the crystalline optic axis in the  $yz$ -plane, we find

$$\begin{aligned} k_{e,z} &\approx n \left( \Theta_c - \frac{\theta_{e,y}}{n_e(\Theta_c, \omega)}, \omega \right) \frac{\omega}{c} \cos \left( \frac{\theta_{e,x}}{n_e(\Theta_c, \omega)} \right) \cos \left( \frac{\theta_{e,y}}{n_e(\Theta_c, \omega)} \right) \\ &\approx n_e(\Theta_c, \Omega) \frac{\Omega}{c} + n_{e,gr}(\Theta_c, \Omega) \frac{\delta \omega_e}{c} + \rho(\Theta_c, \Omega) \frac{\Omega}{c} \theta_{e,y} - \frac{\Omega}{c} \frac{1}{2n_e(\Theta_c, \Omega)} (\theta_{e,x}^2 + \theta_{e,y}^2). \end{aligned} \quad (3.34)$$

For type-II SPDC in a negative birefringent crystal, the pump laser also has the  $e$  polarization. Because the pump beam is assumed to enter close to the surface normal, and  $\theta_{p,x}, \theta_{p,y} \ll \theta_{\text{off}}$ , we can decompose it in plane-wave components and consider only the transverse walk-off in the expansion

$$k_{p,z} \approx n \left( \Theta_c - \frac{\theta_{p,y}}{n_e(\Theta_c, \omega_p)}, \omega_p \right) \frac{\omega_p}{c} \approx n_e(\Theta_c, 2\Omega) \frac{2\Omega}{c} + \rho(\Theta_c, 2\Omega) \frac{2\Omega}{c} \theta_{p,y}. \quad (3.35)$$

Combining Eqs. (3.33), (3.34), and (3.35) yields the dimensionless equation for the wavevector mismatch

$$\begin{aligned} \frac{c}{\Omega} \Delta k \equiv \frac{c}{\Omega} (k_p - k_{o,z} - k_{e,z}) &\approx -C' + (n_{o,gr} - n_{e,gr}(\Theta_c)) \frac{\delta \omega_e}{\Omega} + \\ &\rho(\Theta_c) (2\theta_{p,y} - \theta_{e,y}) + \frac{1}{2n_o} (\theta_{o,x}^2 + \theta_{o,y}^2) + \frac{1}{2n_e(\Theta_c)} (\theta_{e,x}^2 + \theta_{e,y}^2), \end{aligned} \quad (3.36)$$

where the constant  $C' = [n_o(\Omega) + n_e(\Theta_c, \Omega) - 2n_e(\Theta_c, \omega_p)]$ , and where we assumed identical walk-off angles at SPDC and pump frequencies, via  $\rho(\Theta_c, \Omega) \approx \rho(\Theta_c, 2\Omega) \equiv \rho(\Theta_c)$ .

We can apply the transverse-wave-matching condition  $\vec{q}_o + \vec{q}_e = 2\vec{q}_p$  to each of the individual plane-wave components of the (nonplanar) pump laser, which translates into the two equations  $\omega_o \theta_{o,y} + \omega_e \theta_{e,y} = 2\omega_p \theta_{p,y}$  and  $\omega_o \theta_{o,x} + \omega_e \theta_{e,x} = 2\omega_p \theta_{p,x}$ . If we assume frequency degeneracy ( $\delta \omega_e \approx 0$ ) and normal incidence of the pump, we get the relations  $\theta_{o,y} \approx -\theta_{e,y}$  and  $\theta_{o,x} \approx -\theta_{e,x}$ . Using these we find the geometrical shape of the SPDC light in the far field of the crystal: it consists of two rings with frequency-dependent diameters, as determined by the phase-matching condition  $\Delta k < 2\pi$  (see Figs. 3.3 and 3.4). As a side remark, we note that for  $\delta \omega_e \neq 0$  we get  $\vec{\theta}_o + \vec{\theta}_e \neq 0$ . The resulting difference in the spectral bandwidth of  $e$ - and  $o$ -polarized rings has been observed experimentally to be as large as 13% [42].

For plane-wave pumping at normal incidence, we can further simplify the above expressions for the phase mismatch, by setting  $\theta_{p,y} = 0$  and enforcing strict conservation of transverse momentum to convert the  $o$  angles into  $e$  angles. This yields

$$\frac{c}{\Omega} \Delta k = -C + (n_{o,gr} - n_{e,gr}(\Theta_c)) \frac{\delta \omega_e}{\Omega} + \left\langle \frac{1}{n} \right\rangle \theta_{e,x}^2 + \left\langle \frac{1}{n} \right\rangle (\theta_{e,y} - \theta_{\text{off}})^2, \quad (3.37)$$

where  $C = C' + \langle 1/n \rangle \theta_{\text{off}}^2$ .

**Table 3.2:** Definition of symbols used in this chapter

Symbol	Definition
<i>subscript 1, 2</i>	with respect to beams defined by aperture 1 and 2
<i>subscript p</i>	with respect to the pump beam
$o, e$	ordinary- and extraordinary polarization
$x, y$	real-space transverse coordinates
$z$	paraxial optical propagation direction and crystal surface normal
$\mathbf{q} \approx \frac{2\pi}{\lambda} \vec{\theta}$	transverse momentum vector
$\varphi$	angle of polarizer with respect to $o$ (horizontal) polarization
$\theta$	external angle with the crystal surface normal
$\theta_x, \theta_y$	external angle with the crystal surface normal, in the $xz$ or $yz$ plane
$\theta_{\text{off}}$	external (far-field) walk-off angle between $o$ - (or $e$ -)polarized beam and the pump.
$\Theta$	internal angle with the optic axis of the crystal
$\Theta_c$	crystal cut angle (between the optic axis and the surface normal)
$\omega$	optical frequency
$\Delta\omega_{\text{SPDC}}$	spectral width (peak-to-zero) of the SPDC light in frequency units
$\Delta\lambda_{\text{SPDC}}$	spectral width (peak-to-zero) of the SPDC light in wavelength units
$\Delta\theta_{\text{SPDC}}$	angular (far-field) width (peak-to-zero) of the SPDC rings
$n, n(\omega)$	refractive index, function of frequency only
$n_e(\Theta), n_e(\Theta, \omega)$	refractive index for an $e$ ray propagating at angle $\Theta$ inside crystal, function of both angle and frequency
$\langle 1/n \rangle$	inverse average refractive index.
$L$	crystal thickness
$E$	electric field
$\phi = \Delta k L / 2$	average phase mismatch
$\beta$	birefringent phase delay
$T(\omega)$	intensity transmission function of spectral filter
$\hat{\rho}$	density operator
$\Psi$	state vector
$\alpha$	phase in the approximate, simplified state
$\tilde{\alpha}$	average phase in the full state
$\Phi, \Phi_{ij}$	biphoton state amplitude function, for $i$ polarization in beam 1 and $j$ polarization in beam 2
$A_{ij}$	biphoton probability amplitude
$R$	number of coincident photon detections per time unit
$V$	fringe visibility
$P$	concurrence

## CHAPTER 4

---

### Plasmon-assisted transmission of entangled photons

---

*The state of a two-particle system is said to be entangled when its quantum-mechanical wave function cannot be factorized into two single-particle wave functions. This leads to one of the strongest counter-intuitive features of quantum mechanics, namely non-locality [43, 44]. Experimental realization of quantum entanglement is relatively easy for photons; a starting photon can spontaneously split into a pair of entangled photons inside a nonlinear crystal. Here we investigate the effects of nanostructured metal optical elements [13] on the properties of entangled photons. To this end, we place optically thick metal films perforated with a periodic array of subwavelength holes in the paths of the two entangled photons. Such arrays convert photons into surface plasmon waves, optically excited compressive charge density waves, which tunnel through the holes before reradiating as photons at the far side [1, 4, 5, 45]. We address the question of whether the entanglement survives such a conversion process. Our coincidence counting measurements show that it does, so demonstrating that the surface plasmons have a true quantum nature. Focusing one of the photon beams on its array reduces the quality of the entanglement. The propagation of the surface plasmons makes the array effectively act as a which way detector.*

*E. Altewischer, M.P. van Exter, and J.P. Woerdman, Nature **418**, 304-306 (2002).*

Light can potentially couple to surface plasmons (SPs) if the surface in which the SPs reside shows a periodic structure to satisfy conservation of energy and momentum. The samples that we have studied are two metal hole arrays. Each array is  $1\text{ mm} \times 1\text{ mm}$ , and comprises a 200-nm-thick gold layer (on glass) perforated with a square grid of 200-nm-diameter holes spaced with a 700-nm lattice constant; Figure 4.1(a) inset shows a typical scanning electron microscope picture. This figure also shows transmission spectra of the two arrays, measured with a spectrometer using normally incident white light. We can clearly see the resonances due to excitation of SPs on either of the metal-dielectric boundaries. At these resonances, the measured transmission can be orders of magnitude larger than the value obtained from classical diffraction theory for subwavelength holes [1, 2]. In a simple picture, the surprisingly large transmission is due to the coupling of a photon to an SP on one side of the metal, subsequent tunnelling of the SP through the holes to establish an SP at the other side, and final reradiation into a photon [5]. Other prominent features in the spectra are the transmission minima associated with Wood anomalies [4]. The theoretical description of the full transmission spectrum is incomplete at present, but the role of the SP is well established [4, 5, 45]. The resonance used in our experiment is centered at 809 nm, and has a width of  $\approx 40\text{ nm}$ ; a calculation based on the geometry of the array and the optical constants of gold and glass shows that it is associated with the  $(\pm 1, \pm 1)$  SP mode on the glass-metal interface. The label  $(\pm 1, \pm 1)$  denotes any of the four diagonal directions that are frequency degenerate for excitation under normal incidence. Peak transmissions of the two arrays at 813 nm are typically 3% (dashed curve) and 5% (solid curve); these values are much larger than the value of 0.55% obtained from classical theory [2]. The difference in transmission between the two nominally identical hole arrays is ascribed to production imperfections.

Because an SP is a mainly longitudinal, compressive electron density wave, its propagation direction depends on the polarization axis of the incident light, following a certain dispersion relation [46, 47]. In order to confirm this for our samples, we have measured polarization-resolved transmission spectra of one of the hole arrays for various angles of incidence  $\theta_{inc}$  of plane-wave radiation [Fig. 4.1(b) and (c)]. Angle tuning is expected to shift the various resonances in the transmission spectrum in different ways. As we have theoretically associated the peak at 809 nm with a  $(\pm 1, \pm 1)$  SP, we have varied the angle of incidence by tilting the samples along the diagonal axis of the square hole array. For incident light polarized orthogonal to this tilting axis [Fig. 4.1(b)], the 809-nm peak splits and shifts for increasing  $\theta_{inc}$ ; for incident light polarized along the tilting axis [Fig. 4.1(c)], the 809-nm peak remains at approximately the same spectral position. These results confirm the association of the 809-nm peak with the  $(\pm 1, \pm 1)$  SP.

We generate polarization-entangled twin photons at a wavelength of 813 nm with the standard method of type II spontaneous parametric down-conversion [20, 48] depicted in Fig. 4.2. The twin photons travel along two “beam lines” defined by pinholes, pass through polarizers P1 and P2, and are detected by single-photon counters. The photodetectors act as “bucket detectors”, that is, they impose no further transverse mode selection (this is only done by pinholes). To provide the two-photon coincidence rate, the signals from the two detectors are combined electronically in a coincidence circuit with a time window of 2 ns.

In a simplified picture, the generated polarization-entangled state is

$$|\Psi\rangle = \frac{1}{\sqrt{2}} \left( |H_1 V_2\rangle + e^{i\theta} |V_1 H_2\rangle \right), \quad (4.1)$$



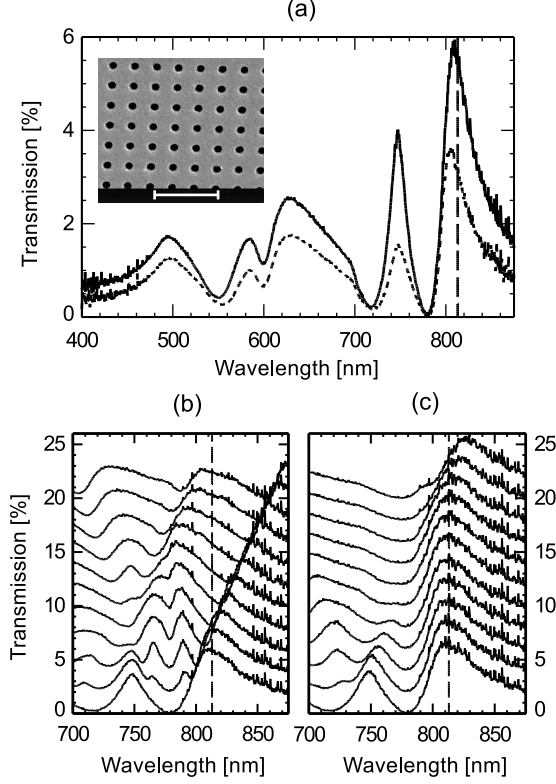


**Figure 4.1:** Wavelength-dependent transmission of the arrays used in the experiment. The dashed vertical line indicates the wavelength of 813 nm used in the entanglement experiment. (a), The transmission of the two arrays. Inset, scanning electron microscope picture of part of a typical hole array. Scale bar, 2  $\mu\text{m}$ . The hole arrays were produced at the Delft Institute of Micro-Electronics and Sub-micron Technology (DIMES) by first defining, with electron beam lithography, arrays of dielectric pillars on a 0.5-mm-thick glass substrate, subsequently evaporating the gold layer onto a 2-nm titanium bonding layer, and finally etching away the pillars to leave the array of air holes. (b), (c), Wavelength-dependent transmission of one of the hole arrays for various angles of incidence at a polarization orthogonal to the tilting axis (b) and along the tilting axis (c). In both graphs the lowest curve is measured with the probe beam at normal incidence, while consecutive curves are measured at increasing angles of incidence (one-degree steps) by tilting of the square hole array around a diagonal. These curves have been plotted with subsequent vertical offsets of 2% on the transmission scale. The resonance around 813 nm (dashed line) shows a complicated splitting for a polarization orthogonal to the tilting axis (b), whereas it is approximately stationary for a polarization along this axis (c).

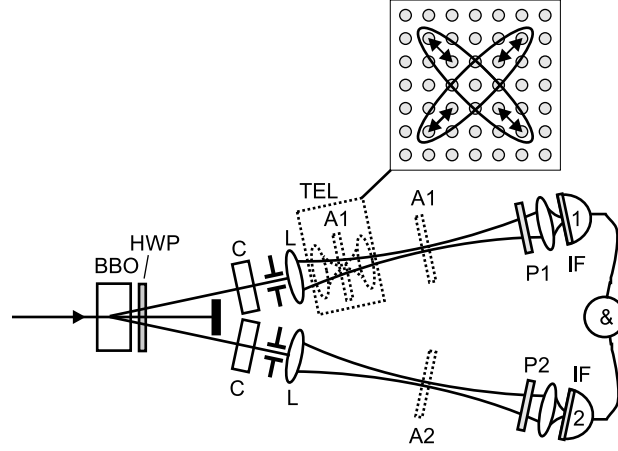


**Figure 4.2:** Experimental setup. A 240-mW continuous-wave krypton-ion laser beam at a wavelength of 406.7 nm is directed onto a 1-mm-thick BBO nonlinear crystal, where the beam diameter is  $\approx 0.50$  mm (full width at  $1/e^2$  points). Inside the nonlinear crystal, a small fraction of the pump photons is down-converted into twin photons at the doubled wavelength (813 nm); these are emitted along two intersecting cones. Polarization-entangled photon pairs are selected with pinholes at the crossings of these cones; the size of the pinholes (far-field diameter 5 mrad) was chosen as a compromise between high yield and good quantum entanglement. Lenses L of 40 cm focal length produce a one-to-one intermediate image of the pumped area, which is used in some experiments to accommodate the hole arrays A1 and A2. After passing through polarizers P1 and P2, the entangled twin photons are focused through interference filters IF (10-nm bandwidth centered at 813 nm) onto single-photon counting modules (Perkin Elmer SPCM-AQR-14). Beam walk-off is compensated by the standard quantum eraser comprising a half-wave plate HWP at  $45^\circ$  and compensating crystals C with a thickness equal to half of that of the generating crystal [20, 48]. The dotted objects are present only in some experiments; they show the hole arrays A1 and A2 at the image positions created by lenses L, or, alternatively, in the focus of the confocal telescope TEL (15 mm focal length lenses). Inset, schematic picture of the near field at the back of array A1 when this is positioned inside the telescope. The arrows indicate the polarization direction of the optical electric field; the center region is unpolarized.

where the state  $|H_1 V_2\rangle$  represents the simultaneous emission and propagation of an H-polarized photon in beam 1 and a V-polarized photon in beam 2. The H- and V-directions are defined by the orthogonal birefringent axes of the BBO ( $\beta$  barium borate) crystal generating the twin photons, and all spatial information is implicitly contained in the beam labelling. By tilting one of the compensating crystals (C in Fig. 4.2), the quantum phase  $\theta$  can be set. In the absence of the hole arrays, our setup produces typically  $3.2 \times 10^4$  coincidence counts per second, which is  $\approx 25\%$  of the single count rate. A measure for the purity of the quantum entangled state is the so-called visibility of the biphoton fringe [20, 48]. This visibility was typically  $V_{0^\circ} = 99.3\%$  and  $V_{45^\circ} = 97.0\%$  at polarization angles of  $0^\circ$  and  $45^\circ$ , respectively (see Table 4.1). The high value at  $45^\circ$  shows that the natural preference of the generating BBO crystal for its birefringent axes ( $0^\circ$  and  $90^\circ$ ) was almost completely removed in our

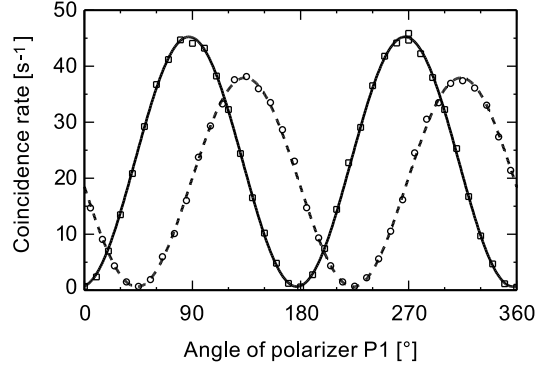


**Figure 4.3:** *Biphoton fringes. These fringes correspond to fourth-order quantum interference, and were measured with the two hole arrays in place, for P2 fixed at 0° (solid curve) and 45° (dashed curve), and P1 varying in steps of 10°.*

setup by the compensating crystals C, which act as quantum erasers.

Placement of the two hole arrays in the two beam lines leads naturally to a marked reduction of single and coincidence counts. Coincidence count rates are typically  $55 \text{ s}^{-1}$  at the optimum setting of the detecting polarizers, which is consistent with the transmissions of the arrays given above ( $3\% \times 5\% \times 3.2 \times 10^4 \text{ s}^{-1} \approx 50 \text{ s}^{-1}$ ). We again measured the purity of the entangled state, and found that the visibilities were now  $V_{0^\circ} = 97.1\%$  and  $V_{45^\circ} = 97.2\%$ , respectively. In Fig. 4.3 the corresponding fourth-order quantum interference fringes are shown for polarizer P2 fixed at  $0^\circ$  and  $45^\circ$ , respectively, and P1 varying in steps of  $10^\circ$ . These measurements show convincingly that the quantum entanglement almost completely survives the transition from photon to SP and back. As a further confirmation, we performed a measurement of the so-called S-parameter, as described in Chapter 3, on a singlet Bell state ( $\theta = \pi$  in Table 4.1). This experiment, which took 16 runs of 100 seconds each, gave a value of  $|S| = 2.71 \pm 0.02$ , which is a violation of the classical inequality ( $|S| \leq 2$ ; Ref. [49]) by 35 standard deviations.

Further experiments were done on a setup with only a single array in one of the beams. The results for this case look very similar to those for the experiment with two arrays; again the entanglement was practically unaffected (see Table 4.1). This is to be expected, as the two-photon wave function of Table 4.1 is perturbed by changes in either of its single-photon components; in principle, a single array could have removed all entanglement. The difference between the two single-array experiments (Table 4.1) is due to imperfections in array 2, which are also observable in its (single-photon) polarization-dependent transmission. As the measurements using only array 2 gave results very similar to the situation with both arrays in place, these imperfections must have caused the somewhat limited visibilities in the two-array experiment.

The most intriguing results of our single-array experiment are obtained when we focus one of the beam lines onto its hole array, using a confocal telescope (close to lens L) of two  $f = 15 \text{ mm}$  lenses symmetrically positioned around the array, as shown inside the large dotted rectangle in Fig. 4.2. Under these conditions, we observe a notable reduction of the degree of quantum entanglement: when the intra-telescope focus has a numerical aperture of 0.13, we

**Table 4.1:** *Biphoton fringe visibilities under various conditions*

Experiment	$R$ [ $s^{-1}$ ]	$V_{0^\circ}$	$V_{45^\circ}$
No arrays	32 k	99.3	97.0
Both arrays	55	97.1	97.2
Only array 1	1.6 k	99.4	97.1
Only array 2	1.0 k	97.5	96.8
Array 1, focussed	1.1 k	73	87

$R$ , measured coincidence count rate;  $V_{0^\circ}$  and  $V_{45^\circ}$ , measured visibility for one of the polarizers fixed at  $0^\circ$  and  $45^\circ$ , respectively.

observe visibilities of  $V_{0^\circ} = 73\%$  and  $V_{45^\circ} = 87\%$  (Table 4.1).

The observed reduction in visibility on focusing can be explained as a consequence of the non-local relation between the electronic excitation in the metal film and the incident optical field; SPs are not at all local, but instead propagate along the dielectric-metal interface at nearly the speed of light over distances of many optical wavelengths [13, 46, 47]. As a result of this propagation, the near-field distribution of the photons that are reradiated at the back of the hole array differs from the spatial profile of the “polarization-isotropic” incident photons. Because we use the  $(\pm 1, \pm 1)$  SP resonance (at 809 nm) we expect, for unpolarized incident light, a near-field pattern consisting of two orthogonal “ellipses” at the back of the hole array (Fig. 4.2 inset). The unpolarized overlap region of these ellipses correspond to the focused incident light, whereas the polarized “protuberances” introduce the possibility of distinguishing the polarization of the photons on the basis of their spatial near-field coordinates. This will then automatically remove part of the polarization entanglement, just as any which way information will do. Note that the observed reduction in visibility is much stronger for  $V_{0^\circ}$  than for  $V_{45^\circ}$ , contrary to what is generally found without using hole arrays [20, 48]. This observation is consistent with the fact that we excite SPs propagating in the “diagonal” ( $45^\circ$ ) directions.

The non-local nature of the electronic response is equivalent to an explicit wavevector dependence of the dielectric function (“spatial dispersion” [50]). The latter description highlights the far-field aspects of a non-local dielectric response, and is related by way of a Fourier transform to the near-field picture given above. A theory for the reduction of visibility due to this effect must intrinsically be a multi-mode theory because, after passage through the hole arrays, the spatial information within each beam should be accounted for. Discussion of such a theory is beyond the scope of this Letter, but qualitative arguments are easily found. When adopting a near-field point of view, the reduction of the visibility is expected to be significant when the propagation or coherence length  $l$  of the SP is comparable to the transverse coherence length of the focused incident beam. This is indeed the case for our experiment: on the basis of the spectral width of the transmission peak at 809 nm, we estimate  $l < 4 \mu\text{m}$ ; the number of holes covered by the propagating SPs is thus about 10. In comparison, the transverse coherence length of the light is  $\approx 4 \mu\text{m}$  (set by the 5-mrad far-field selection due to the pinholes; Fig. 4.2). We note that the SP propagation length is an order of magnitude smaller than the value  $l \approx 40 \mu\text{m}$  predicted for a smooth pure gold film [13]; we ascribe this difference to radiative decay due to the hole patterning, and to extra damping by the titanium

bonding layer.

From a general perspective, the observed conservation of quantum entanglement for the conversion from photon  $\rightarrow$  surface plasmon  $\rightarrow$  photon is a demonstration of the true quantum nature of SPs. All experiments on SPs so far have not probed their quantum nature, but only their wave nature through their semiclassical dispersion relation. We note that the true quantum nature of the photon was only established in 1977, in anti-bunching experiments [51, 52]. Furthermore, a simple estimate shows that SPs are very macroscopic, in the sense that they involve some  $10^{10}$  electrons. Our experiment proves that this macroscopic nature does not impede the quantum behaviour of SPs, because they can act as intermediates in transmitting entangled photons to yield the expected fourth-order interference. A theory for our experiments based only on locally induced surface currents is clearly inadequate. We stress this point because some recent theoretical models for one-dimensional gratings in thick metal films have questioned the role of SPs, emphasizing instead waveguide effects. Our arrays are apparently thin enough (thickness/period  $< 0.3$ ) for waveguide effects not to play an important role. This conclusion is supported by experiments in which the thickness of such a thin array has been varied [4].

By addressing the topic of plasmon-assisted transmission of quantum entangled photons, we have combined two fields of research, namely quantum information and nanostructured metal optics. We hope that our work will stimulate other studies of the transfer of entanglement to condensed-matter degrees of freedom.

## **Acknowledgements**

We thank A. van Zuuk and E. van der Drift for the production of the hole arrays. We thank G. Nienhuis for theoretical discussions.

#### 4. Plasmon-assisted transmission of entangled photons

## CHAPTER 5

---

### Nonreciprocal reflection of a subwavelength hole array

---

*We present measurements of the wavelength-dependent reflectivity of a subwavelength metal hole array on a glass substrate. We compare the observed resonant structures to those found in transmission and note a nonreciprocity under illumination from the air versus the glass side. This can be used to verify on which interface the surface plasmons are resonantly excited and to estimate the losses in the subwavelength channels.*

*E. Altewischer, M.P. van Exter, and J.P. Woerdman, Opt. Lett. 28, 1906-1908 (2003).*

Recently, subwavelength hole arrays in metal films have received a lot of attention [1, 4–6, 21, 53], as they show an unexpectedly large transmission compared to predictions of conventional diffraction theory [2]. This large transmission is attributed to the resonant excitation of surface plasmons (SPs) [13], which, in the standard model [1, 4], can reside on either interface [4]. In this model the in-plane momentum of the SPs is supplied by the projected component of the incident optical wave momentum plus a lattice component taken from the hole array. Quite surprisingly, the reflection properties of these nanostructures have not yet been reported, although they are essential for a complete description and understanding of the optical system; as we will show, they provide a tool to determine on which side of the metal film the resonances are localized. The transmission cannot give such information, as it does not change under reversal of the film due to the reciprocity theorem; however, reflection can be nonreciprocal if losses are incorporated in an asymmetric structure [54, 55]. We present here the first reflection spectra of a subwavelength hole array, measured in zeroth order and under normal incidence.

The hole array used in the experiment consists of a 200 nm thick gold film (much thicker than the optical skin depth of  $\approx 12$  nm) deposited on a 0.5 mm thick glass substrate, with a thin (2 nm) titanium bonding layer in between. A  $1 \times 1$  mm<sup>2</sup> array of cylindrical air holes arranged in a square grid was made in the gold film, by first defining an array of pillars by electron beam lithography, subsequently evaporating the metal onto the substrate, and finally removing the pillars. The hole diameter is 200 nm and the array period 700 nm, as determined from scanning electron-beam micrographs (error within 1%); the refractive index of the glass (Schott-type BK7) is 1.51 in the wavelength range 650–1100 nm. Note that the glass substrate provides for the necessary asymmetry to remove the wavelength degeneracy between resonances at both sides of the film [1, 4], so that losses, in principle, can break reflection reciprocity.

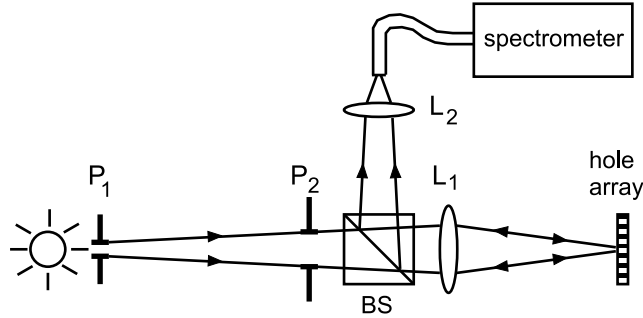


**Figure 5.1:** Experimental setup for reflection measurements, comprising an incandescent lamp as light source, two pinholes ( $P_1$  and  $P_2$ ), a beamsplitter (BS), two imaging lenses ( $L_1$  and  $L_2$ ), the hole array and a fiber connected to a grating spectrometer. The hole array was placed with either its glass-metal or its air-metal side facing the beam.

Figure 1 depicts the experimental setup; an incandescent lamp was used as light source. A combination of two pinholes and a lens serves to limit the spot size on the hole array to  $500 \mu\text{m}$ , with an associated numerical aperture (NA) of 0.01 rad. A beamsplitter redirects the reflected light onto a multi-mode fiber (core diameter  $200 \mu\text{m}$ ,  $\text{NA}=0.20$  rad) serving as input



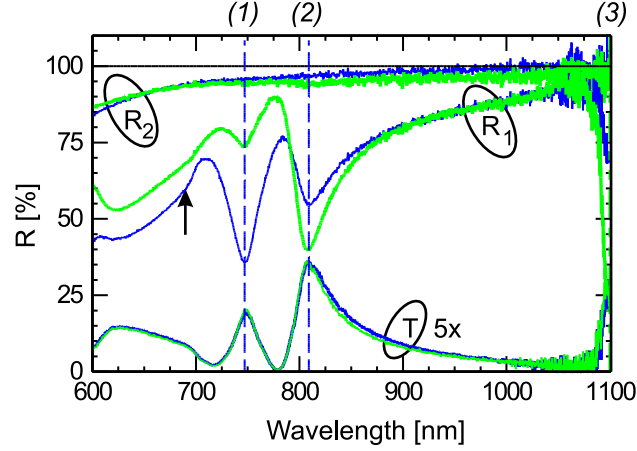


**Figure 5.2:** The curves  $R_1$  correspond to measured reflection spectra of the hole array. For comparison the corresponding reflection spectra of the neighbouring unperforated gold film are shown as the curves  $R_2$ . Also shown are corresponding transmission spectra  $T$ , of which the vertical scale has been multiplied by a factor of 5. In all spectra the black curves were obtained when illuminating the air side of the hole array and the gray curves when illuminating the glass side. The dashed vertical lines indicate the positions of the resonances, at wavelengths of: (1) 747 nm, (2) 810 nm and (3) just over 1100 nm. The arrow indicates a kink in the spectrum, due to the onset of first-order diffracted modes.

to a grating spectrometer with a CCD detector (Avantes Avaspec-2048, resolution 1.2 nm). An additional lens in front of the fiber allows us to capture all light, as it makes an image of only 100  $\mu\text{m}$  on the fiber-core facet, while staying well within the numerical aperture of the fiber.

Figure 2 shows the measured reflection spectrum of the hole array and the neighbouring unperforated gold film, illuminated under normal incidence from either the glass or the air side (see caption). These curves have been obtained by averaging over many individual measurements to increase the signal-to-noise ratio, which deteriorates above 1000 nm due to limited detector efficiency. As reference for the 100% level we have used a broadband silver mirror (New Focus 5103), of which the reflectivity was in turn calibrated against a dielectric mirror with  $R \geq 99\%$  (New Focus 5102) in the range 700–1050 nm. The estimated accuracy of the vertical reflectivity scale is better than 5% in absolute units and, of course, much better in relative units; this estimate is based on the reproducibility and alignment sensitivity. For comparison, we also show the measured *transmission* spectrum of the hole array, multiplied by a factor of 5.

The reflection spectra of the hole array show resonant structures quite similar to those observed in transmission. Three such structures are discernable at wavelengths of approximately 750, 810 and just over 1100 nm, which have been labelled as (1), (2) and (3) respectively in Fig. 5.2; unfortunately, structure (3) is at the end of our measurement range. The dotted vertical lines show that the structures are neatly aligned in all spectra. On the basis of the standard model mentioned above, peak (1) can be assigned to the resonant excitation, on the air-metal

interface, of the  $(\pm 1, 0)$  &  $(0, \pm 1)$  SPs, and peak (2) and (3) to the resonant excitation, on the glass-metal interface, of the  $(\pm 1, \pm 1)$  and the  $(\pm 1, 0)$  &  $(0, \pm 1)$  SPs, respectively. Typical amplitudes of these resonances are much larger in reflection than in transmission (the vertical scale of the transmission spectrum has been magnified 5 times). As an aside we note the slight kink in the spectra at a wavelength of 700 nm (see arrow in Fig. 5.2), which is precisely equal to the lattice period; this indicates the onset of first-order diffraction modes (both in reflection and transmission).

The key point to note in Fig. 5.2 is that there is a striking difference between the reflection spectra observed from the glass side (red) and the air side (blue); on the contrary, the transmission spectra do not show this asymmetry, in fact they overlap within the experimental accuracy. Theoretically, the transmission spectra should of course be equal on account of the reciprocity theorem. For the reflection spectra nonreciprocity *is* allowed and can be used to obtain additional information. Experimentally, we find that in the air-side reflection spectrum peak (1) is the most prominent, whereas in the glass-side reflection peaks (2) and (3) are stronger. This indicates that the resonances are dominantly localized at a specific interface and show up most prominently in the reflection spectrum taken under illumination from that side. Furthermore, the aforementioned observations agree with the assignment based on the standard model, thereby confirming its validity.

A quantitative analysis of the observed differences in reflection was performed as follows: for peak (2) we look specifically at the structure observed between 770 and 830 nm, which has a nearly identical shape in both spectra. The glass-side resonance ranges from 90% at 775 nm to 40% at 810 nm, while the air-side resonance ranges from 76% to 55%. The strength of the glass-side resonance, as quantified by the relative variations in reflectivity, is therefore roughly a factor  $50/21 = 2.4$  more than that of the air-side resonance. Similarly, for peak (3) around 1100 nm the reflectivities range from 97% to 23% for the glass side and from 100% to 70% for the air side, giving a factor of  $74/30 = 2.5$ , although the uncertainty is larger here since this peak is off-scale. For peak (1) the structures in the region between 710 and 770 nm match less well in shape. Therefore, we compare the average reflectivity of the two maxima to the minimum in between, which yields the following numbers: reflectivities of 85% to 74% for the glass side and 73% to 36% for the air side, giving a factor of  $11/37 = 1/3.4$  for the resonance strength as observed from either side.

The measured difference between the reflection dips observed in “frontside” and “back-side” illumination is naturally attributed to propagation loss in the cylindrical waveguides represented by the holes: the resonance at the interface opposite to the illuminated one can still be felt, but at the cost of a double pass through the subwavelength holes. In the absence of an exact theory, it seems likely that the observed peaks in reflection are dominated by the coherent interference between a resonant and a nonresonant reflection amplitude, as in the Fano-type description of hole-array transmission [53]. The observed factor of roughly 3 should then be interpreted as a roundtrip amplitude loss. This may be compared with recent transmission experiments on hole arrays with identical (200 nm) hole diameter and varying thicknesses, where an exponential intensity decay length of  $\approx 50$  nm was reported [21]. This would correspond to a roundtrip amplitude loss of  $\exp(4) \approx 55$ , i.e., a much larger value. This estimate might however be too naive, as the aforementioned experiments [21] show that the exponential dependence breaks down for films thinner than 300 nm, for as yet unknown reasons. Our results seem to confirm this breakdown.

In conclusion, we have presented the first reflection spectra of a subwavelength hole array. These exhibit strong features that resemble those found in transmission. On the basis of the asymmetry of the reflection under reversal of the array, we are able to identify the interface at which the SPs are dominantly excited; this is a powerful diagnostic tool to characterize a given hole array without needing a priori knowledge about its structure. A more quantitative analysis of the spectra suggests a break-down of the exponential field decay, that one would expect for waveguides below cut-off. This is consistent with experiments reported by others [21], but cannot yet be explained. The fact that there is no complete theory yet makes our measurements extra useful, as they provide a new piece of the puzzle.

## **Acknowledgements**

We thank A. van Zuuk and E. van der Drift at the Delft Institute of Micro-Electronics and Sub-micron Technology (DIMES) in Delft, the Netherlands, for the production of the hole arrays.

5. Nonreciprocal reflection of a subwavelength hole array

## CHAPTER 6

---

### Polarization analysis of propagating surface plasmons in a subwavelength hole array

---

*We present angle- and polarization-resolved measurements of the optical transmission of a subwavelength hole array. These results give a far-field visualization of the propagation of the excited surface plasmons and allow for a simple analysis of their polarization properties.*

*E. Altewischer, M.P. van Exter, and J.P. Woerdman, JOSA B **20**, 1927-1931 (2003).*

Metal films perforated with a periodic array of subwavelength holes have recently been shown to exhibit a much larger optical transmission than expected [1]. The reason for this is the presence of surface plasmons (SP's) on the metal interfaces, which couple to freely propagating light via the two-dimensional grating of the hole array. In a simple picture, the incident light gets through because it first excites SP's on the front side of the metal layer, which then couple through the holes to SP's on the back side, that finally reradiate in the form of light. Since its original discovery [1], this phenomenon has been studied in many theoretical and experimental papers [4, 5, 45, 56]. An aspect that has been underexposed up to now is the role of polarization in the transmission process. SP's are combined optical-electronic excitations that comprise a (longitudinal) electric field aligned with their propagation direction, which for a large part determines their coupling to the (input and output) optical field. In this paper we address experimentally the polarization properties of the transmission, both by varying the polarization of the light incident on the hole array and by analyzing the polarization of the output light.

The SP-assisted optical transmission through subwavelength hole arrays is usually described in a simple model, where the in-plane momentum of the SP's is supplied by the projected component of the incident optical wave momentum plus a lattice component that is taken from the hole array [4]. This lattice momentum can be used to label the SP resonances as  $(N_x, N_y)$ . When the surrounding media are not the same (air and glass, in our case, as discussed below), the observed transmission resonances are generally assumed to be dominated by SPs excited on either the one or the other surface.

Surface Plasmons have been extensively studied with near-field microscopy [46, 47, 57, 58], which allows a mapping of the optical field with subwavelength resolution. To study the SP propagation on metal hole arrays one has to excite them locally by limiting the incident beam size, i.e., by focussing the beam to a spot size of the order of the SP propagation length (still covering many holes of the array). Generally, a study of the SP propagation, which covers many optical wavelengths, does not require subwavelength resolution; we show in this article that, in fact, such a study can be done equally well in the optical *far field*. We describe a (polarization and angle-resolved) analysis of the optical far-field transmitted through a metal hole array illuminated with strongly focussed light. This analysis allows one to check the validity of the "single SP resonance" model mentioned above, and the mode assignment of the various transmission peaks.

The transmission spectrum of a subwavelength hole array depends on the angle of incidence, which co-determines the momentum of the excited SP's. A measurement of this angle dependence was used by Ghaemi *et al.* to determine SP dispersion curves [4] (i.e., the SP bandstructure); they used a *collimated* beam to measure the transmission spectrum over a large wavelength range for a set of fixed angles of incidence. In contrast, in this article we use a fixed wavelength and monitor the transmission of a *strongly focussed* beam incident along the  $z$ -axis at this specific wavelength. We measure in fact the transmission into the zeroth-order diffracted beam, as a function of the two far-field angles  $(\theta_x, \theta_y)$  (the  $z$ -axis is aligned with the surface normal). Contrary to near-field diagnostics, such a measurement can be performed in a single exposure. We illuminate the array with a strongly focussed beam in order to excite SP's locally, and use a subsequent Fourier transforming lens and a CCD to record the optical far field emitted by the array; this principle is further discussed below.

An input-output description of the transmission through the hole array is rather simple,

because it is a linear process and because the array can supply only multiples of the basic reciprocal lattice vectors. We take the opening angle  $\Delta\theta$  (FWHM) of the incident light small enough to avoid overlap and interference between possible scattering orders (typically  $\Delta\theta \approx 23^\circ$ ); i.e., any incident plane-wave component leads to an isolated zero-order output plane-wave component that makes the same angle with the surface normal. In this case the zero-order diffracted beam is simply given by

$$\tilde{E}_{out,i}(\theta_x, \theta_y; \lambda) = \sum_j \tilde{t}_{ij}(\theta_x, \theta_y; \lambda) \tilde{E}_{in,j}(\theta_x, \theta_y; \lambda), \quad (6.1)$$

where  $\tilde{E}_{out,i}$  is the far field at the backside of the hole array and  $\tilde{E}_{in,j}$  is the field incident at the frontside of the array, with  $i, j = x, y$  the two transverse coordinates in the paraxial approximation. Equation (1) gives a complete description of the far field behind the array; the transmission matrix  $\tilde{t}_{ij}(\theta_x, \theta_y; \lambda)$  specifies the amplitude and polarization relation between the input and output plane-wave components at wavelength  $\lambda$  and angles  $(\theta_x, \theta_y)$  with the array normal ( $z$  axis). The corresponding near-field relation is found by Fourier transforming Eq. (6.1), and is given by

$$E_{out,i}(x, y; \lambda) = \sum_j \int t_{ij}(x', y'; \lambda) E_{in,j}(x - x', y - y'; \lambda) dx' dy', \quad (6.2)$$

where the integration is over the area occupied by the hole array, and  $E_{out,i}$  and  $E_{in,j}$  are the near-field components at the array. By applying a standard Fourier theorem, the product of  $\tilde{t}$  and  $\tilde{E}$  in Eq. (6.1) has been changed into a convolution of the corresponding Fourier-transformed quantities in Eq. (6.2). The Green's tensor function  $t_{ij}(x', y'; \lambda)$  (the Fourier transform of  $\tilde{t}_{ij}$ ) now describes the (near-field) transmission properties of the array and thus contains both polarization and propagation effects.

For completeness, we note that Eq. (6.1) is not valid for diffraction by a *single* subwavelength hole; in order to have a plane wave at the output we need a (periodic) *array* of such holes. Even without the above analysis, it is obvious that far-field measurements on a single subwavelength hole would not provide useful information, contrary to near-field measurements.

Experimentally, the transform from near field to far field can be realized by putting the hole array in the focus of a telescope consisting of two positive lenses. The input lens of the telescope focusses the (collimated) beam to the desired spot size; the far field can be observed at the back focal plane of the output lens. It is important to note that, in this situation, the observed far-field pattern does not depend on the (longitudinal) position of the hole array with respect to the intratelescope focus of the incident beam. This follows trivially from the far-field description in Eq. (6.1), because propagation of the field from one transverse plane to another along the focussed beam does not change the angles of the plane-wave components present in the beam, so there is no (longitudinal) position dependence in Eq. (6.1). In the near-field picture, on the other hand, this invariance sounds somewhat surprising. If the array is moved out of the focus of the incident beam, the size of the optical field on the array will certainly change. On naive arguments one might expect the (transverse) SP propagation to be less important for larger illumination spots. The apparent paradox between near-field and far-field descriptions can be resolved, however, by noting that the phase of the optical

field is as important as its amplitude; the SP's are excited coherently and transport this phase information to positions where they decay radiatively (and thus contribute to the output field). When the hole array is positioned outside the optical focus, where the incident beam is relatively large but has a curved optical phase front, it is the transverse transport of the phase information by SP's that apparently produces the structure in the far field.

A far-field measurement as described above allows for a simple analysis of the polarization aspects of the transmission. For a square array and normal incidence (with plane-wave illumination) these are trivial: there is no polarization dependence of the transmission and the polarization of the output is the same as that of the input, i.e., the transmission is polarization isotropic. This is because the square symmetry of the array allows only excitation of frequency-degenerate sets of SP's, each having a well defined polarization; these polarizations sum up to the same polarization as that of the incident light, again due to the square symmetry. For instance, the set  $(\pm N, 0)$ , which is  $x$  polarized, is frequency degenerate with the set  $(0, \pm N)$ , which is  $y$  polarized. For normal incidence on a rectangular array this frequency degeneracy would disappear and the polarization properties would become anisotropic. Somewhat analogously, the same thing happens for non-normal incidence on a square array.

In the experiment, we measured the far field of the transmitted light of the hole array by putting it in the focus of a telescope, consisting of a confocal configuration of two lenses ( $L_1$ ) with 15-mm focal length each, as shown in Fig. 6.1. The telescope was illuminated by a linearly polarized laser beam from a Ti:sapphire-laser with a tunable wavelength. This beam was first focused through a 10- $\mu\text{m}$  pinhole (P) to produce a nearly plane wave, homogeneous illumination of the entrance pupil of the telescope, which was set by a 6-mm diaphragm (D). We estimate the spot diameter at the intratelescope focal plane as approximately 2 to 3  $\mu\text{m}$  (i.e., covering roughly 15 holes). The orientation of the input polarization was set with a half-wave-plate (HWP). A relay lens ( $L_2$ ; 10-cm focal length) was used to make a one-to-one image of the output telescope-lens on a CCD (Apogee), which therefore recorded the far-field transmission pattern of the array. This pattern was observed to be independent of the longitudinal position of the array relative to the focus, except from a trivial cut off of the angular size of the transmitted far field when the array is too much out of focus; this confirms the theoretical discussion given above.

The array that we have studied is a 1 mm  $\times$  1 mm hole array in a 200-nm-thick gold layer, which is attached to a 0.5 mm glass substrate by a 2-nm titanium bonding layer. The metal layer is perforated with a square grid of 200-nm diameter holes spaced with a 700-nm lattice constant. A typical transmission spectrum of the hole array for unfocused light (i.e., beam diameter  $\approx$  1 mm) at normal incidence is shown in Fig. 6.2 (solid curve); this spectrum was measured with an incandescent lamp in combination with a fibre-coupled grating spectrometer array. The peak transmission of the most prominent resonance, 6 % at 810 nm, is much larger than the value of 0.56 % expected from "classical" theory [2]. On the basis of the simple model described above [4], we associate the 810 nm resonance with the four  $(\pm 1, \pm 1)$  modes on the metal-glass interface, which are frequency degenerate at normal incidence. The measured transmission spectrum in the focused situation (i.e., spot diameter approximately 2 to 3  $\mu\text{m}$ ) is shown in Fig. 6.2 (dashed curve). The individual peaks are "smeared out" as compared to the full curve, due to the angle dependence of the transmission, i.e., the SP dispersion, in combination with the effective integration over the range of angles of incidence



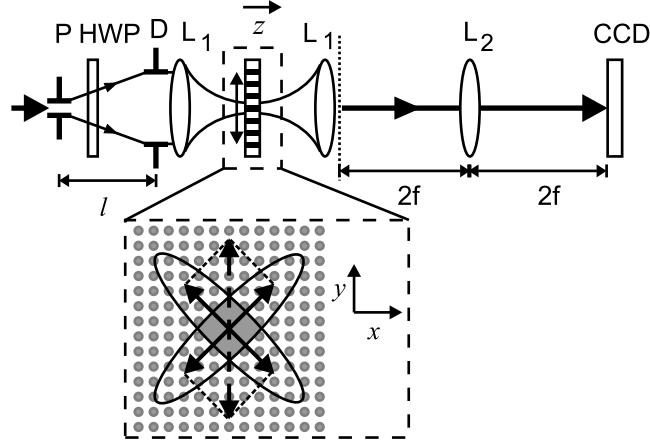


**Figure 6.1:** Light from a Ti:sapphire frequency-tunable laser is passed through a pin-hole  $P$  (diameter  $10\ \mu\text{m}$ , positioned at  $l = 40\ \text{cm}$ ), half-wave plate  $HWP$ , diaphragm  $D$  and a telescope consisting of two lenses  $L_1$  of  $15\text{-mm}$  focal length. The hole array, which is positioned in the center of the telescope, modifies the optical field profile through SP excitation and propagation in the transverse ( $xy$ ) plane (see arrow and inset). Relay lens  $L_2$  images the transmitted far field (dashed line) onto a CCD, which thus records the transmission in a single run. Inset: Schematic representation of the near field at the backside of the hole array for  $810\text{-nm}$  light. The incident optical electric field, polarized at  $90^\circ$  (dashed arrow), is decomposed into four resonant SP's (solid contour lines). These SP's propagate along, and are polarized at,  $+45^\circ / +225^\circ$  and  $-45^\circ / +135^\circ$  respectively (solid arrows). The shaded overlap region is polarized along the incident field. In the far field, narrow and wide dimensions are interchanged due to Fourier relations, but the polarization directions remain unchanged.

that is present in the focus.

Figure 3 shows the measured far-field pattern at a wavelength of  $810\ \text{nm}$ . Each of the four pictures was obtained for a different linear input polarization, (a)  $0^\circ$ , (b)  $90^\circ$ , (c)  $45^\circ$  and (d)  $-45^\circ$ , indicated by arrows in the pictures. The throughput intensity is measured without any further polarization analysis. In all images, interference rings of equal inclination are visible. These result from the glass substrate acting as a Fabry-Perot and producing interference for the plane-wave components at different angles present in the focus. When the hole array is removed the far field returns to almost uniform illumination [the intensity varies less than 25% across the field of view, as can be seen in the cross-section shown in Fig. 6.3(e)] so that Fig. 6.3(a) and (d) give a relatively good quantitative measure for the angle-dependent transmission  $T(\theta_x, \theta_y)$ . The pictures in Fig. 6.3 visualize the nature of the dominant SP resonances that are addressed at  $810\ \text{nm}$ . The prominent diagonal "lobes" are consistent with the  $(\pm 1, \pm 1)$  labelling. For incident light polarized along  $0^\circ$  (or  $90^\circ$ ) the lobes on *both* the diagonals are excited [Fig. 6.3(a) and (b)]. For  $+45^\circ$  input polarization angle only the lobes along *one* of the diagonals are excited [Fig. 6.3(c)], for  $-45^\circ$  the complementary ones [Fig. 6.3(d)]. This shows that the incident optical electric field is decomposed into components along the four resonant modes, thereby exciting either one or both diagonals

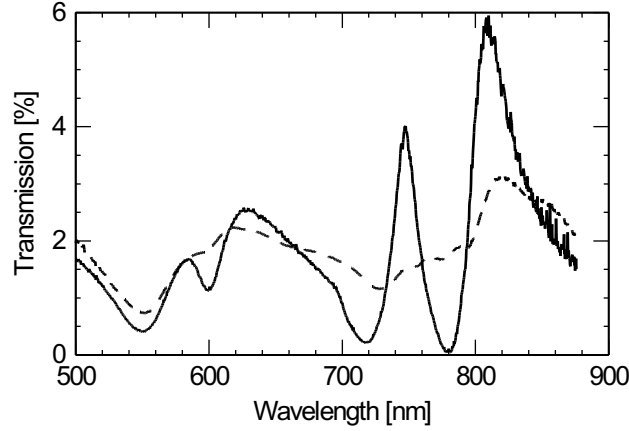


**Figure 6.2:** Wavelength-dependent transmission of the hole array used in the experiment, for unpolarized (white) light. The solid curve shows the transmission spectrum in the case of a normally incident plane wave as input. The dashed curve corresponds to a focused beam as input.

depending on the incident polarization angle. This is displayed schematically in the dashed inset in Fig. 6.1 for incident light of  $90^\circ$  polarization angle, where the incident field (dashed arrow) is decomposed into two equal components along the “diagonal” ( $\pm 1, \pm 1$ ) modes (solid arrows).

From the far-field measurements of Fig. 6.3 we can extract information about the near field at the backside of the array as long as we restrict ourselves to near-field structures larger than an optical wavelength. More specifically, from the measured transmission  $\tilde{t}_{ij}(\theta_x, \theta_y; \lambda)$ , we obtain information on the propagation direction and the mean free path of the excited SP’s (being several optical wavelengths large). Based on Fourier relations as those between Eqs. (6.1) and (6.2), a *compact* far field in a certain direction corresponds to a *wide* near field in that direction; such a wide near-field distribution in  $t_{ij}(x, y; \lambda)$  corresponds to SP propagation. This is evident in Fig. 6.3(c), where an input polarization of  $45^\circ$  gives a far field that is compact in the same direction but wide in the orthogonal direction. A rough quantitative estimate based on a  $3^\circ$  (FWHM) far field corresponds to a near-field propagation of only  $2 \mu\text{m}$ ; in this calculation it has been assumed that the SP’s propagate along one fixed axis, i.e., in one dimension. A more accurate two-dimensional description which takes into account the (slight) spread in the SP propagation direction (induced by focussing), would lead to a slightly larger propagation length [similar to the 20% larger far-field diffraction width of a circular aperture (two dimensional), as compared to a slit (one dimensional) of identical width [27]]. As the value for the propagation length is certainly much smaller than the theoretical value of  $40 \mu\text{m}$  expected for a smooth gold film at this wavelength [13], we note that SP scattering by the holes, (mainly) leading to radiation decay, must be very important. Our result is consistent with propagation lengths that can be deduced from other experiments [59].

In a second experiment, the polarization of the 810-nm mode was analyzed by putting a polarizer behind the hole array. Fig. 6.4(a) and (b) show the measured far fields for an

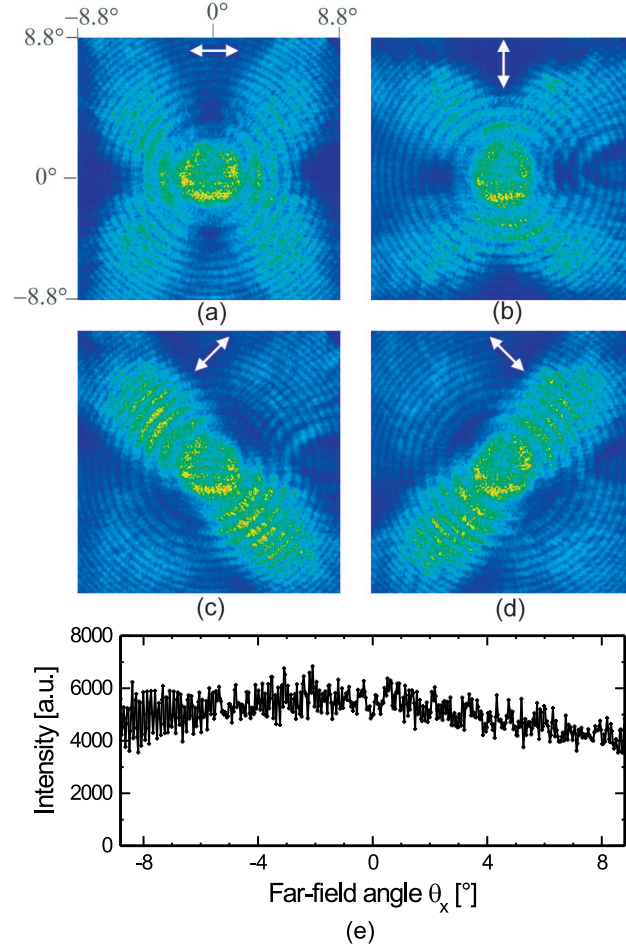


**Figure 6.3:** Far-field transmission of the hole array, at a wavelength of 810 nm. The CCD images span a  $17.6^\circ \times 17.6^\circ$  solid angle (the far-field angles are indicated by the numbers alongside the figures). The input polarization (white arrows) was set at (a)  $0^\circ$ , (b)  $90^\circ$ , (c)  $45^\circ$ , (d)  $-45^\circ$ . The color scales are different for each picture. A cross-section along  $\theta_y = 0$  of the far field recorded without array in the telescope (e) shows that the input illumination was nearly uniform.

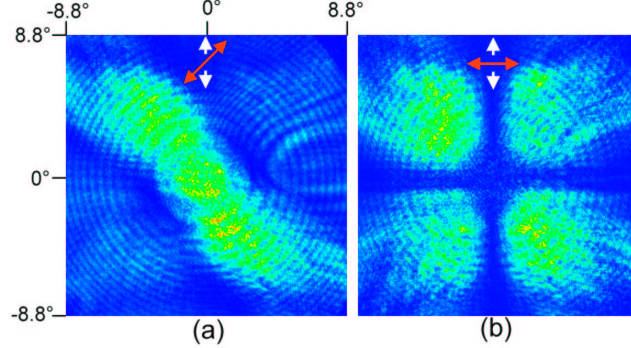


**Figure 6.4:** Polarization analysis of the far-field transmission of the hole array at 810 nm. The far-field angles are indicated by the numbers alongside the figures ( $17.6^\circ \times 17.6^\circ$  solid angle). The input polarization is  $90^\circ$  (white arrows). The polarizer in front of the CCD is oriented at (a)  $45^\circ$  and (b)  $0^\circ$  (red arrows).

input polarization of  $90^\circ$  (white broken arrows), which excite both  $+45^\circ$  and  $-45^\circ$  modes equally (see also the inset in Fig. 6.1). In the first picture [Fig. 6.4(a)] the analyzing polarizer was set at  $+45^\circ$  (red arrows). For this polarization, only the lobes corresponding to the (1,1) and (-1,-1) modes are visible. This demonstrates that the associated SP modes are polarized at  $+45^\circ$  and, at the same time, that the orthogonal (invisible) (-1,1) and (1,-1) modes are polarized at  $-45^\circ$  (for which the polarizer is at blocking angle). In both cases, the Fourier-transform argument tells us that the polarization is in the same direction as the SP propagation direction, as expected. The second picture [Fig. 6.4(b)], made with the analyzing polarizer at  $0^\circ$  (blocking angle to input polarization), shows no intensity in the central overlap region (corresponding to the telescope axis), whereas the outward lobes (corresponding to off-axis angles) do have intensity. This is consistent with the statement that the transmission in the central spot, which corresponds to angles of incidence close to zero, is polarization isotropic. In the inset in Fig. 6.1, this is illustrated (in the near field) by the shaded region, where both orthogonal polarization components are present and overlapping due to the finite width of the lobes (indicated by the solid contour lines). On the other hand, the outward lobes (outside the shaded region in Fig. 6.1) each have a unique polarization (indicated by arrows). In fact, the outward lobes behave quite similar to polarizers, as they transmit only the polarization component of the incident light aligned with their axis (at  $\pm 45^\circ$ ). In the situation of Fig. 6.4(b), where the hole array is effectively placed between two orthogonal polarizers (at  $0^\circ$  and  $90^\circ$ ), this means that the “lobe-polarizers” (at  $\pm 45^\circ$ ) are expected to transmit 1/4 of the incident intensity, due to simple projection arguments.

Some further comments on the far fields in Fig. 6.3 and Fig. 6.4 are as follows:

(i) A closer look at Fig. 6.3(a) and (b) reveals that these figures are not perfectly fourfold symmetric, but have some twofold symmetry admixed; this slight symmetry breaking is not visible for the “pure”lobes in Fig. 6.3(c) and (d), which are intrinsically twofold symmetric. Notice also the (modest) S-shape in Fig. 6.4(a).

(ii) A closer look at Fig. 6.4 shows slight symmetry breaking in the transmission values

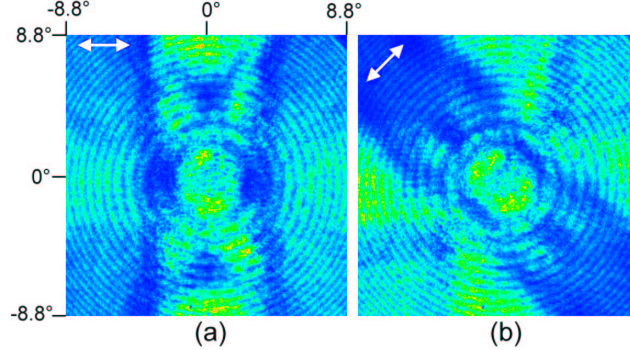


**Figure 6.5:** Far-field transmission of the hole array, at a wavelength of 750 nm. The far-field angles are indicated by the numbers alongside the figures ( $17.6^\circ \times 17.6^\circ$  solid angle). The input polarization (white arrows) was set at (a)  $0^\circ$  and (b)  $45^\circ$ . Note the presence of  $xy$ -oriented lobes, which is very prominent in (a), but also visible in (b). The color scales are different for each picture.

of the four outward lobes (ii): Off axis, i.e., in the lobes, typical transmissions for  $0^\circ$ -input polarization are 35% ( $\pm 5\%$ ) for  $0^\circ$ -output polarizer, and 15% ( $\pm 5\%$ ) for  $90^\circ$ -output polarizer. Note that these transmissions are normalized to the maximum (center) value in Fig. 6.4(a). These values differ significantly from the expected 25%, based on the assumption that the transmission process is mediated by the  $(\pm 1, \pm 1)$  modes only.

The observations (i,ii) mentioned above demonstrate that, for certain details, it is too simple to consider only a single set of SP's living on one side of the array, i.e., only the  $(\pm 1, \pm 1)$  metal-glass modes. Theoretically, one expects the strongest influence of the  $(\pm 1, 0)$  and  $(0, \pm 1)$  modes on the air-metal side (at  $\approx 750$  nm), as they are the nearest resonance. The coherent admixture of these modes would be consistent with the observations (i,ii).

On the basis of the SP-assisted transmission model, one expects that transmission resonances at different wavelengths have different far-field patterns and polarization properties. We have confirmed this by far-field measurements for the resonance at 750 nm, as shown in Fig. 6.5. The 750-nm resonance shows horizontal and vertical lobes [both in Fig. 6.5(a) and (b)], confirming the expected  $(\pm 1, 0)$  and  $(0, \pm 1)$  nature of the SP's at this frequency. However, for this wavelength the patterns are more complicated than those at 810 nm; note, for instance, the dark bands, which are oriented orthogonal to the input polarization in both Fig. 6.5(a) and (b). This complication is also visible in the more complex dispersion curves at this wavelength (not shown).

In conclusion, we have shown that polarization-dependent measurements of the far field are useful to analyze the optical properties of metal hole arrays. The reason that we can deduce useful information from the far field is simply that the SP propagation length is larger than the optical wavelength; our method does not (of course) give information on subwavelength scales. The far-field method is conceptually simple and is an important addition (if not substitute) to near field methods which are inherently more difficult to perform and interpret. We have shown that the polarization plays an important role, as it is related to SP propagation. In a way, SP modes act as polarizers that pass only the polarization component that is

aligned with their propagation directions. Our measurements show that the gross features of the transmission can be adequately explained by a “single SP resonance” model. The limitations of this simple model show up, however, indicating that more modes have to be taken into account for a realistic theoretical description of the transmission process.

## **Acknowledgements**

We thank A. van Zuuk and E. van der Drift at the Delft Institute of Micro-Electronics and Sub-micron Technology (DIMES) in Delft, The Netherlands, for the production of the hole arrays.

## CHAPTER 7

---

### Fano-type interference in the point spread function of nanohole arrays

---

*Measurement of the point-spread function of metal nanohole arrays by using microscopic imaging reveals two contributions. The first of these is due to propagating resonant surface plasmons and the second to nonresonant transmission through the holes. We observe a Fano-type interference between these contributions.*

*E. Altewischer, X. Ma, M.P. van Exter and J.P. Woerdman, accepted for publication in Opt. Lett.*

Subwavelength hole arrays in metal films show intriguing transmission resonances that are usually attributed to the resonant excitation of surface plasmons (SPs) propagating along the array surface [1,6,26]. The important role of SPs has been deduced, amongst others, from the polarization-dependent angular dispersion of these transmission resonances. The most direct proof yet is the imaging of the SPs as they propagate along the metal film. This imaging is generally done with scanning near-field optical microscopes (SNOM), which have sub-wavelength resolution [60,61]. We use a simpler approach, namely, conventional (“far-field”) microscopic imaging, equivalent to a point-spread function measurement. Being diffraction-limited, microscopic imaging does not allow single-hole resolution. This is not a problem however when studying SP propagation, because they propagate over many optical wavelengths. Furthermore, conventional imaging gives less ambiguous results and an excellent signal-to-noise ratio.

A similar imaging technique was demonstrated very recently by Tetz et al. [62]. In contrast to their approach our technique is not only sensitive to the propagating SPs, but also allows the observation of a direct (nonresonant) transmission, the presence of which was already inferred from the asymmetric Fano-type line shapes in transmission spectra [12,53]. By comparing the imaging results with a simple model, based on damped two-dimensional Huygens spherical wavelets, we are able to quantify both the relative amplitude and the relative phase of this important term. We also observe a Fano-type interference with the transmission carried by the propagating SPs.

We use a simple two-channel Huygens model to describe the spatially resolved optical transmission of our nanohole arrays [63]. In the “direct” channel each hole transmits a fixed fraction of the incident optical field. In the “indirect” channel, however, the input and output profile can be very different. Because the holes are much smaller than the optical wavelength, we treat them as discrete points. Each hole acts as a dipole emitter of SPs, which propagate as damped two-dimensional waves along the array surface and can subsequently be coupled out as photons at any hole they encounter. In certain directions, determined by the SP wavelength and the lattice spacing and symmetry, constructive interference will give rise to SP resonances. As a result, the output profile will contain “exponentially” decaying tails in the direction of these resonantly excited SPs [64]. We stress that the SP modes are not put in by hand, but appear naturally as resonances in the summation.

In our Huygens model the output field  $E^{\text{out}}$  is given by a discrete convolution, i.e., a sum over all lattice points  $\vec{\rho}$ , of the propagator  $G(\vec{\rho})$  and the input field  $E^{\text{in}}$ :

$$E_i^{\text{out}}(\vec{\rho}') = \sum_j \sum_{\vec{\rho}} G_{ij}(\vec{\rho}) E_j^{\text{in}}(\vec{\rho}' - \vec{\rho}) \quad (7.1)$$

$$G_{ij}(\vec{\rho}) \propto \tilde{\sigma} \delta(\vec{\rho}) \delta_{ij} + (1 - \delta(\vec{\rho})) \frac{[\hat{\rho} \otimes \hat{\rho}]_{ij}}{\sqrt{\ell}} \exp(-\ell/L_{\text{SP}}) \exp(ik_{\text{SP}}\ell), \quad (7.2)$$

where  $\ell = |\vec{\rho}|$  is the distance between excitation point and radiation point,  $\hat{\rho} = \vec{\rho}/|\vec{\rho}|$  is the propagation direction,  $\delta(\vec{\rho})$  is the discrete Dirac delta function ( $\delta(\vec{\rho}) = 1$  only at  $\vec{\rho} = 0$ ) and  $\delta_{ij}$  is the Kronecker delta; the factor  $(1 - \delta(\vec{\rho}))$  expresses that an SP cannot be coupled out at the hole it is created at (no “self-coupling” of SPs). This model contains three variables: i) the complex-valued  $\tilde{\sigma}$ , which specifies the relative amplitude and phase of both transmission



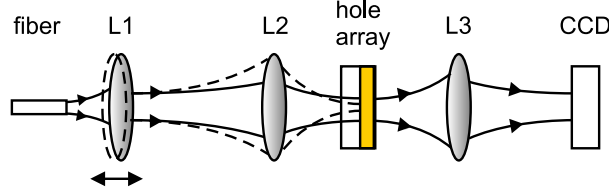


**Figure 7.1:** Experimental setup in which the hole array, positioned with its glass side oriented towards the input beam, is illuminated with a tightly focussed beam. The position-resolved transmission is obtained through direct imaging onto a CCD.

channels, ii) the SP decay length  $L_{\text{SP}}$ , and iii) the optical frequency  $\omega$ , expressed in terms of the SP momentum  $k_{\text{SP}} = n_{\text{eff}}\omega/c$  for propagation at a speed of  $c/n_{\text{eff}}$ . The subscripts  $i, j$  label the two polarizations orthogonal to the surface normal. The direct channel is polarization isotropic, since the holes in our arrays are circular. The indirect channel, however, contains a polarization projection factor  $[\hat{\rho} \otimes \hat{\rho}]_{ij}$ , which accounts for the projection of the input field on the longitudinal field component of the SPs (oriented along the propagation direction  $\hat{\rho}$ ). The factor  $1/\sqrt{\ell}$  takes care of energy conservation in the two-dimensional plane. This factor becomes visible only for propagation lengths that are sufficiently large compared with the excitation spot size, where beam spreading becomes important.

Our nanohole array was fabricated with e-beam lithography and consisted of a 200-nm thick gold film on a 0.5-mm thick glass plate with a 2-nm thick titanium bonding layer in between [65]. The holes of 200-nm diameter were spaced in a square lattice with lattice period  $a = 700$  nm. We address the  $(\pm 1, \pm 1)$  mode at the glass-metal interface, which has a transmission peak at 810 nm (see Chapter 6). Figure 7.1 shows the optical beam line which starts with a laser beam at 810 nm that is mode-cleaned by a fiber. Two microscope objectives allow us to adjust the size of the focus on the hole array, which is positioned with its glass side towards the beam. A third objective projects a magnified image of the back of the array onto a CCD. To minimize (spherical) aberrations great care was taken in selecting the illumination objective L2 (40 $\times$ , NA = 0.6 with adjustable glass correction) and the imaging objective L3 (50 $\times$ , NA = 0.6), both with long working distance.

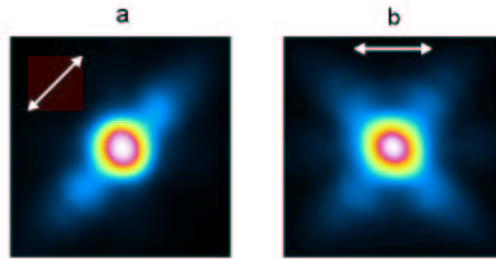


**Figure 7.2:** Two output profiles of a square hole array excited with a Gaussian input profile with spot radius  $w = 1.6 \mu\text{m}$  (image size is  $15 \times 15 \mu\text{m}^2$ ). The input polarizations are oriented along the arrows.

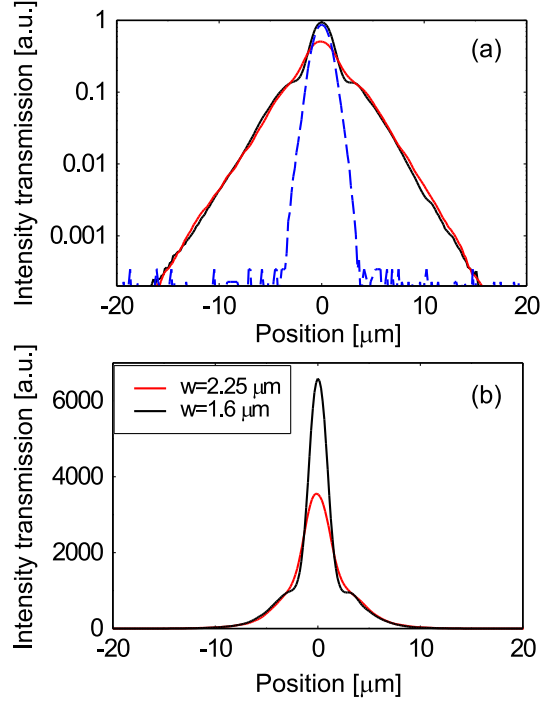


**Figure 7.3:** Cross-sections of the output profile along the SP propagation direction (diagonals of the square array) for excitation with “diagonal” polarization. The corresponding spot sizes of the input beam are  $w = 1.6$  (dark curve) and  $2.3 \mu\text{m}$  (gray curve), respectively. For reference the ( $w = 1.6 \mu\text{m}$ ) input profile measured through the bare glass plate is also shown (dashed curve). (a) Logarithmic scale. (b) Linear scale.

Typical output profiles for our square array with circular holes are shown in Fig. 7.2. The structure of the profiles depends on the size of the input beam waist (see below). The optical polarization plays a special role: it allows one to selectively excite certain SP modes. This is illustrated in Fig. 7.2(a) where the input polarization is along one array diagonal, exciting only the resonant SPs propagating in this direction. In Fig. 7.2(b) the input polarization is horizontal, thereby exciting the resonant SPs propagating along both diagonal directions.

Cross sections along one diagonal of the output profiles are shown in Fig. 7.3 for two different illumination beam radii  $w = 1.6$  and  $2.3 \mu\text{m}$ , respectively. The curves are normalized to the total input power and the input polarization was set as in Fig. 7.2(a). In Fig. 7.3(a) (logarithmic scale) a cross section of the smallest input beam ( $w = 1.6 \mu\text{m}$ ) is also included, which shows that the input is nicely Gaussian. The obtained images of the hole array transmission contain speckle, presumably caused by irregularities and surface defects in the hole array. To remove this speckle, we average over 100 different transverse array positions in the focal plane. As is visible in Fig. 7.3, this gives high-quality measurements with smooth curves and a dynamic range of more than four orders of magnitude. We experimentally checked that the averaged image of the transmission is independent of the longitudinal position of the hole array with respect to the focus (see Chapter 6). An out-of-focus array position in fact has the

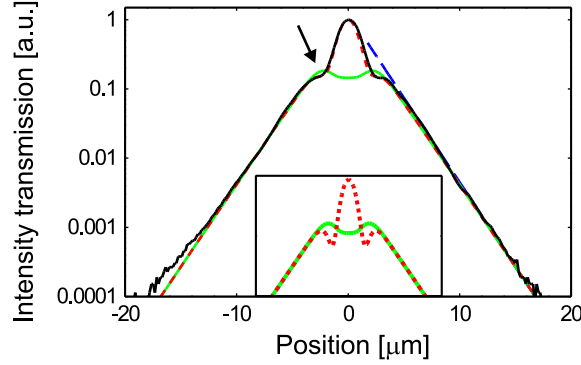


**Figure 7.4:** The measured cross-section at  $w = 1.6 \mu\text{m}$  (identical to the dark solid curve in Fig. 7.3) and three fits. The dashed dark line on the right is a simple exponential fit. The gray solid and gray dashed curves are results of the Huygens model, with  $\tilde{\sigma} = 0$  and  $\tilde{\sigma} = 4.9 \times \exp(-1.2i)$ , respectively. The inset shows two theoretical curves with  $\tilde{\sigma} = 0$  (solid) and  $\tilde{\sigma} = 4.9 \times \exp(-1.6i)$  (dashed) demonstrating the Fano-type interference more clearly.

advantage that the speckle is “averaged out” even more because the input beam covers more holes than in the focus; however, in order to maintain conceptual simplicity, we did not use this trick.

The two channels can be recognized immediately: the central part of the figure, resembling the input profile, originates from the direct channel, whereas the exponentially decaying tails show the SP propagation in the indirect channel. The changing of the input beam waist has two effects: it changes the peak power originating from the direct contribution and it changes the way the two channels interfere. The first effect is seen more clearly in Fig. 7.3(b) (with a linear scale), where there is a factor 1.9 difference between the transmitted peak intensities for the two input beam waists. The second effect produces the “dips” in the curve for  $w = 1.6 \mu\text{m}$ ; these are not present in the curve for  $w = 2.3 \mu\text{m}$ .

The relatively large peak transmission for the direct channel seems surprising, because the opposite is true in transmission spectra, where the SP resonances are much stronger than the direct transmission. This surprise disappears when the spatially integrated output power is considered. Because the direct contribution is localized to the excitation spot, and the SP-mediated contribution is spread out and diluted over a much larger area because of SP propagation, the spatially integrated SP part still dominates the total transmission. This is in agreement with published optical far-field measurements where the direct channel was hardly observable (see Chapter 6).

To further explore the interference between the two channels, we compare the experimental cross-section at  $w = 1.6 \mu\text{m}$  (taken from Fig. 7.3) with three fits in Fig. 7.4. A simple exponential fit of the wings (shown here for the right-hand wing only) gives an average SP propagation length of  $L_{\text{SP}} = 1.9 \pm 0.1 \mu\text{m}$ . The two other curves in the main panel of Fig. 7.4 show simulated results from the full Huygens model, where the gray dashed curve is the best fit to the experimental data with  $|\tilde{\sigma}| = 4.9 \pm 0.7$  and  $\arg(\tilde{\sigma}) = -1.2 \pm 0.2$ , and the gray solid curve has  $\tilde{\sigma} = 0$ ; both use the value for  $L_{\text{SP}}$  determined above and are calculated at the

resonance  $k_{sp} = 2\pi\sqrt{2}/a$ . The absence of a contribution for  $\ell = 0$  in the indirect channel causes the lower transmission at the position 0. The differences between the gray dashed and solid curves at the position indicated by the arrow in Fig. 7.4, are caused by a Fano-type interference effect: when both channels are active, interference between the two gives a lower intensity at the mentioned positions than when only the indirect channel contributes. The interference is best observable at the arrow positions where the two channels are approximately equally strong. The exact shape of the curve at these points depends strongly on the value of  $\arg(\tilde{\sigma})$ , as can be seen from the inset in Fig. 7.4 with  $\arg(\tilde{\sigma}) = -1.6$ , where prominent “dips” appear. The curve shape can thus be used to estimate this phase.

A comparison of a measured transmission spectrum for plane-wave illumination with the theoretical spectrum calculated on the basis of the Huygens model, requires a value of  $\arg(\tilde{\sigma}) = -0.7$  rad to get a good fit. The deviation from the value of  $\arg(\tilde{\sigma}) = -1.2$  rad given above, can be due to a slightly “out-of-focus” position of one of the lenses, causing a wave-front curvature with an associated additional phase difference. Another reason might be a small detuning of  $k_{sp}$  from resonance, for which the model is rather sensitive.

In conclusion, we have shown that direct imaging of the transmission of nanohole arrays can provide valuable insights into their transmission mechanism. A simple Huygens model including Fano-type interference is able to explain the measured data quite well.

## Acknowledgement

We thank A. van Zuuk and E. van der Drift at the Delft Institute of Micro-Electronics and Sub-micron Technology (DIMES) in Delft, the Netherlands, and P. F. A. Alkemade at the Kavli Institute for Nanoscience, Delft, the Netherlands, for producing the hole array samples.

## CHAPTER 8

---

### Polarization tomography of metallic nanohole arrays

---

*We report polarization tomography experiments on metallic nanohole arrays with square and hexagonal symmetry. As a main result we find that a fully polarized input beam is partly depolarized after transmission through a nanohole array. This loss of polarization coherence is found to be anisotropic; i.e., it depends on the polarization state of the input beam. The depolarization is ascribed to a combination of two factors: (i) the nonlocal response of the array as a result of surface plasmon propagation and (ii) the nonplane-wave nature of a practical input beam.*

*E. Altewischer, C. Genet, M.P. van Exter, J.P. Woerdman, P.F.A. Alkemade, A. van Zuuk, and E.W.J.M. van der Drift, Opt. Lett. **30**, 90-92 (2005).*

Currently there is much interest in the optical properties of thin metal films perforated with arrays of subwavelength holes, or nanohole arrays. The optical transmission of these arrays shows a strongly peaked spectrum with anomalously large transmission peak values; this is usually ascribed to resonant excitation of propagating surface electromagnetic waves or surface plasmons (SPs) [1, 4, 13]. In this Letter we focus on the polarization properties of the anomalous transmission and show that these are strongly influenced by the propagating nature of the SPs.

So far, polarization properties of nanohole arrays have been studied in a limited context: a beam with a given uniform state of polarization ( $\text{SOP}_{in}$ ) is transformed, by an anisotropic array or an isotropic array with nonspherical holes, in a different uniform state of output polarization ( $\text{SOP}_{out}$ ) [9, 66, 67]. This corresponds to a mapping of the Poincaré sphere onto itself; for instance, a rectangular array or a square array with elliptical holes acts as a birefringent and (or) dichroic element that may convert a linear SOP into an elliptical SOP, conserving polarization coherence. In the present Letter we focus instead on cases where the *degree* of polarization (DOP) is reduced,  $\text{DOP}_{out} < \text{DOP}_{in}$ , corresponding to a reduction in radius and, in general, a deformation of the Poincaré sphere [68, 69]. To underline this point we have chosen for our experiments square and hexagonal arrays, i.e., arrays that, for symmetry reasons [70], cannot modify the SOP for plane-wave illumination at normal incidence. As we will show, depolarization occurs when two (quite common) conditions are simultaneously fulfilled: (i) the response of the array is nonlocal because of SP propagation, and (ii) the input beam is not a plane wave [but e.g. a Gaussian beam, with a finite numerical aperture (NA)].

In general, depolarization occurs when an optical system acts nonuniformly on polarization within the (spatial or temporal) bandwidth of the incident wave, thereby coupling polarization to other degrees of freedom. Experimentally, a study of depolarization requires a measurement of the Mueller matrix by a tomographic method [68, 69]. Here we report such polarization-tomography experiments on nanohole arrays and interpret the results in the context of SP propagation.

We start by recapitulating the essence of our theoretical model [70]. The input and output optical fields of the array are related via a nonlocal linear response as  $\vec{E}_{out}(\vec{r}, \omega) = \int t(\vec{r} - \vec{r}', \omega) \vec{E}_{in}(\vec{r}', \omega) d\vec{r}'$ . In the far-field, or Fourier domain, this is equivalent to  $\vec{E}_{out}(\vec{k}_t, \omega) = t(\vec{k}_t, \omega) \vec{E}_{in}(\vec{k}_t, \omega)$ , where  $\vec{k}_t$  is the transverse wavevector component; the output  $\vec{k}_t$  is equal to the input  $\vec{k}_t$  for the zeroth-order transmission. If the nonlocal response depends on polarization, the four elements of the  $2 \times 2$  transmission tensor  $t(\vec{k}_t, \omega)$  will exhibit a different angular dependence and the output field  $\vec{E}_{out}(\vec{k}_t, \omega)$  will have a spatially dependent polarization even for a polarization-pure input field, see Chapter 6. After spatial integration, this transmission process can be captured in the simple relation  $S_{out} = MS_{in}$ , which relates the input and output Stokes vectors through the  $4 \times 4$  Mueller matrix  $M$ . For ideal square and hexagonal arrays the Mueller matrix has been predicted to be diagonal (no mixing of Stokes parameters) [70]. For hexagonal arrays, the additional symmetry relation  $M_{11} = M_{22}$  holds.

The magnitudes of the diagonal elements  $M_{00}$ ,  $M_{11}$ ,  $M_{22}$  and  $M_{33}$  depend on the dimensionless product of the SP propagation length and the wave-vector spread of the input beam,  $\ell_{SP} \Delta k_t$ . A full theoretical description thereof would require a microscopic model; however, from physical considerations it can be seen that an appreciable deviation of  $M_{ii}/M_{00}$  from 1 requires  $\ell_{SP} \Delta k_t > 1$ . In any case there will be no depolarization if either there are no propa-

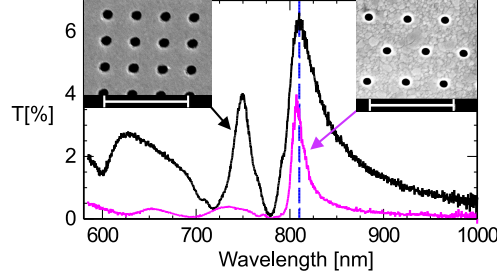


**Figure 8.1:** Transmission spectra of nanohole arrays under almost plane-wave illumination at normal incidence for the square and hexagonal array. The dashed vertical line indicates the resonance wavelength of 810 nm used in the experiments. The insets show scanning electron-beam micrographs of the arrays, with 2- $\mu\text{m}$  scale bars.

gating waves ( $\ell_{SP} = 0$ ) or there is plane-wave illumination ( $\Delta k_t = 0$ ); both propagation and a wave-vector spread are necessary. This statement holds for hole arrays of any symmetry (i.e., not only for the square and hexagonal arrays used in our experiment).

To measure the Mueller matrices we use a linearly polarized titanium:sapphire laser at a wavelength of 810 nm, which is the approximate resonance wavelength of the hole arrays (see Fig. 8.1), to illuminate the input lens of a symmetric telescope. After transmission through a hole array positioned at the focus of the telescope, the light is imaged onto a photodiode. The SOP of the incident light is set by a rotatable quarter- or half-wave plate in front of the first lens. The Stokes parameters at the output are measured with a rotatable quarter-wave plate and a polarizer positioned in front of the photodiode. The polarization isotropy of all optical components was checked by measuring the Mueller matrices of the setup in the absence of hole arrays. These matrices were practically equal to the identity matrix, with individual elements deviating by not more than 0.02 (typically 0.008).

Our arrays were fabricated in Au films on glass substrates. We used a square array made with electron-beam lithography, with a lattice spacing of 700 nm and a nominal hole diameter of 200 nm, and a hexagonal array made with ion-beam milling, with a lattice spacing of 886 nm and a nominal hole diameter of 200 nm. Transmission spectra of both arrays under almost plane-wave illumination at normal incidence are shown in Fig. 8.1. Both arrays show a resonance wavelength of 810 nm; the polarization experiments were performed at this wavelength. These resonances correspond to SPs propagating in the  $(\pm 1, \pm 1)$  direction at the metal-glass interface for the square array, and the (six-fold degenerate)  $(1, 0, 0)$  direction at the metal-air interface for the hexagonal array (the labeling is with respect to the reciprocal lattice vectors) [71]. The linewidths are 40 nm and 25 nm for the square and hexagonal arrays, respectively, from which we estimate  $\ell_{SP} \approx 2\mu\text{m}$  and  $\ell_{SP} \approx 4\mu\text{m}$ , respectively [61]. The difference in  $\ell_{SP}$  values is probably caused by both the different array structures and the different resonant surfaces (less damping on the air-metal interface than on the glass-metal interface).

We have characterized the arrays with almost plane-wave illumination (numerical aperture of  $\text{NA} = 0.01$  or  $\Delta k_t \approx 0.08\mu\text{m}^{-1}$ ) and focussed illumination (over a range up to  $\text{NA} \approx 0.15$  or  $\Delta k_t \approx 1.2\mu\text{m}^{-1}$ ). Figure 2 shows the dependence of the diagonal elements of the Mueller matrix on the NA of the incident light for both arrays. The figure shows that, for

**Table 8.1:** Mueller matrices measured under four different conditions. Normalization constants (absolute intensity transmission for unpolarized light) of the matrices are 1.4% (hexagonal NA 0.01), 0.47% (hexagonal NA 0.10), 7.1% (square NA 0.01) and 2.2% (square NA 0.15).

Measurement	Mueller matrix M
Square array NA = 0.01 $\ell_{sp}\Delta k_t \approx 0.2$	$\begin{bmatrix} \boxed{1.00} & 0.00 & -0.02 & 0.00 \\ -0.02 & \boxed{1.01} & -0.01 & 0.00 \\ 0.00 & 0.00 & \boxed{1.01} & -0.01 \\ 0.00 & 0.00 & 0.02 & \boxed{0.99} \end{bmatrix}$
Square array NA = 0.15 $\ell_{sp}\Delta k_t \approx 2$	$\begin{bmatrix} \boxed{1.00} & 0.01 & -0.02 & 0.01 \\ 0.01 & \boxed{0.55} & -0.04 & -0.03 \\ -0.04 & 0.02 & \boxed{0.84} & 0.01 \\ -0.01 & 0.01 & 0.01 & \boxed{0.41} \end{bmatrix}$
Hexagonal array NA = 0.01 $\ell_{sp}\Delta k_t \approx 0.3$	$\begin{bmatrix} \boxed{1.00} & 0.06 & -0.14 & 0.00 \\ 0.04 & \boxed{1.00} & 0.00 & -0.07 \\ -0.12 & 0.01 & \boxed{1.01} & -0.03 \\ 0.00 & \boxed{0.06} & 0.02 & \boxed{0.97} \end{bmatrix}$
Hexagonal array NA = 0.10 $\ell_{sp}\Delta k_t \approx 3$	$\begin{bmatrix} \boxed{1.00} & 0.03 & -0.11 & 0.00 \\ 0.02 & \boxed{0.78} & 0.00 & -0.08 \\ -0.13 & 0.01 & \boxed{0.78} & 0.00 \\ 0.00 & \boxed{0.06} & 0.02 & \boxed{0.51} \end{bmatrix}$

the case of almost plane-wave illumination (NA  $\approx 0$ ), the  $M_{ii}$  values are close to 1 for both arrays. There is no depolarization, as  $\Delta k_t \approx 0$ . However, for increasing wavevector spread, or decreasing spot size on the array, the depolarizing effect of the arrays quickly increases. Furthermore, the depolarization is clearly anisotropic, i.e., the amount of depolarization depends on the input SOP, because the  $M_{ii}$  are not all equal. For the hexagonal array the depolarization sets in faster with increasing NA than for the square array, because of the smaller resonance linewidth (larger  $\ell_{sp}$ ) of the hexagonal array.

The effect of the different array symmetries on the curve shapes are prominent. For the square array [Fig. 8.2(a)], the observed inequality  $M_{22} > M_{11}$  shows that there is less depolarization for an input polarization along either of the array diagonals than for a polarization along the main axes. This observation is consistent with the  $(\pm 1, \pm 1)$ -propagation directions of the resonantly excited SPs on the metal-glass interface; as SPs are mainly longitudinally polarized, they preserve polarization along their propagation direction. However, the deviation of  $M_{22}$  from 1 indicates that the  $(\pm 1, \pm 1)$  SPs are not the only SPs involved in the transmission process; other (nonresonant) SPs on both surfaces apparently contribute,



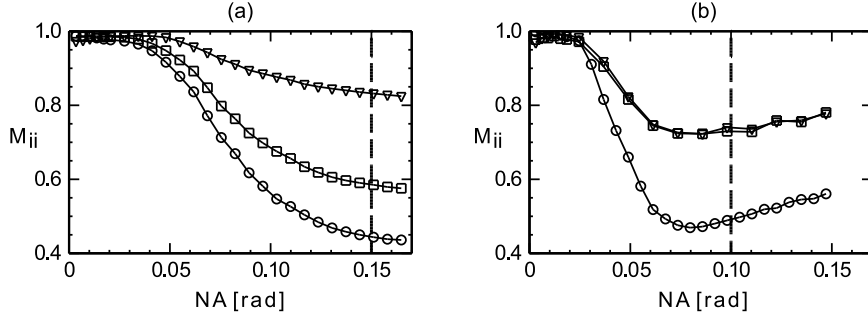


**Figure 8.2:** Diagonal elements  $M_{ii}$  of the Mueller matrix, normalized to  $M_{00}$ , as a function of the NA of the incident light beam on the (a) square and (b) hexagonal hole array. Squares,  $M_{11}$ ; triangles,  $M_{22}$ ; circles,  $M_{33}$ ; dashed vertical lines indicate the NAs at which the full Mueller matrices were measured (see Table 8.1).

see Chapter 6. For the hexagonal array [Fig. 8.2(b)] the theoretical equality  $M_{11} = M_{22}$  also holds quite well. For both arrays,  $M_{33}$  is the smallest diagonal element. This shows that depolarization is most dramatic for circularly polarized light, a case that, to our knowledge, has not been studied before. We note that  $M_{33} \approx M_{11} + M_{22} - 1$  for both arrays; this follows from an extension of the symmetry-based theory used here by explicit modeling of SP propagation (see Chapter 9).

The full Mueller matrices for both arrays are shown in Table 8.1. The diagonal elements (marked with boxes in the table) conform to the discussion given above. The off-diagonal elements of a perfectly symmetric square or hexagonal array should theoretically be zero. For our square array they are indeed relatively small and do not show any systematic behavior. For the hexagonal array, however, these elements are much larger, both for plane-wave and focussed illumination. Furthermore, the off-diagonal elements have a clear pattern and similar values in both cases, where the odd off-diagonal elements  $M_{02}$ ,  $M_{20}$ ,  $M_{13}$  and  $M_{31}$  (underlined in the Table 8.1) are substantially larger than the others. This pattern was checked to be present also for an intermediate NA of 0.03. The pattern is compatible with a birefringent and (or) a dichroic  $45^\circ$  axis, which is apparently due to array errors, such as a spatially variant lattice spacing or ellipticity of the holes. These errors could be created by alignment errors or even intrinsic imperfections in the ion-beam optics (astigmatism and deflection errors). Our work shows that polarization tomography provides for sensitive diagnostics of array symmetry imperfections.

From a general perspective, Mueller tomography is a purely phenomenological tool to characterize the polarization behavior of optical systems. Still, it can give new insight into the physical mechanisms active in hole arrays, in our case SP propagation. It would, for instance, be interesting to perform Mueller tomography on metal hole arrays in the (sub)millimeter-wave regime, as SPs propagate much farther in this part of the spectrum, which is expected to increase the depolarization. Another area of interest is the connection between classical polarization properties and entanglement degradation.

In conclusion, we have demonstrated surprising consequences of SP propagation for the polarization behavior of nanohole arrays. The nonlocality of the array response forms an essential ingredient of the physics of these intriguing devices.

8. Polarization tomography of metallic nanohole arrays

## CHAPTER 9

---

### Analytic model of optical depolarization in square and hexagonal nanohole arrays

---

*We present a simple analytic model, based on surface plasmon propagation, that explains the depolarization induced by metal hole arrays illuminated with linearly and circularly polarized light of varying numerical aperture. Arrays with square and hexagonal lattices of circular holes are compared. We relate this model to experimental data.*

*E. Altewischer, M.P. van Exter and J.P. Woerdman, accepted for publication in J. Opt. Soc. Am. B.*

## 9.1 Introduction

Some years ago, the optical transmission of thin metal films perforated with arrays of sub-wavelength holes, or nanohole arrays [1, 4, 6], has been shown to have a strongly peaked spectrum with anomalously large transmission peak values. This phenomenon is usually ascribed to the resonant excitation of propagating surface electromagnetic waves or surface plasmons (SPs) [13]. Recently, a number of papers have studied the polarization properties of arrays of noncircular holes [9, 67, 72], but we limit ourselves here to the case of circular holes. The polarization properties of square and hexagonal arrays of circular holes are trivial for plane-wave illumination at normal incidence because the input and output state of polarization (SOP) are equal (see Chapter 8). For a plane wave at nonnormal incidence, the output SOP can be different from the input SOP, but it will still be a pure state. Only in a focussed light beam, consisting of many plane waves at different angles of incidence, will the output polarization not be pure anymore. A spatially uniform input SOP will generally be transformed into a spatially varying output polarization, which translates into a depolarization of the beam considered as a whole. The purpose of this paper is to introduce a simple model that relates depolarization to hole array symmetry and SP propagation and compare the predictions of our model to published measurements (see Chapter 8).

In general, depolarization, or a loss of polarization coherence, occurs when an optical system couples polarization to spatial or temporal degrees of freedom, within the spatial or temporal bandwidth of an incident wave [68]. The most convenient theoretical tool to describe depolarization is the Mueller matrix  $[M_{ij}]$  [68, 69], where we use the notation  $M_i \equiv M_{ii}$  for the diagonal elements. This real-valued  $4 \times 4$  matrix couples input and output Stokes vectors  $[S_j]$  ( $j = 0, 1, 2, 3$ ), which represent (spatial and time) averages of the optical polarization. The Mueller formalism is thus capable of handling partially polarized or incoherent waves. Conversely, the also widely used Jones formalism is applicable only to coherent and spatially uniformly polarized light [68, 69].

In nanohole arrays, depolarization is induced by SP propagation. SPs propagate along well-defined directions, determined by momentum conservation in the array surface plane. They have well-defined polarizations along these propagation directions, where the polarization is determined by the longitudinal component of the SP electric field [13]. A sketch of the depolarizing process is shown in Fig. 9.1, where SP propagation transforms a spatially uniform linear-polarized input beam into a spatially more extended output beam with nonuniform polarization. The diagonal “lobes” that point in the propagation directions of the resonantly excited SPs are polarized accordingly (indicated by the arrows in Fig. 9.1). This near-field description can equivalently, but mathematically more conveniently (see Chapter 6 and 8), be translated into the far field. This can be done through the angle and polarization dependence of the array transmission tensor  $t(\vec{\theta})$ , which relates the input optical field to the output field. It follows from Fourier-transform arguments that depolarization becomes observable if the product of the transverse [73] wavevector spread  $\Delta k_{tr}$  of the incident light and SP propagation length  $\ell_{SP}$  is of the order of 1 or larger (see Chapter 8). So far, an analytical model for this depolarization has been lacking; this is what we aim for in the present paper.

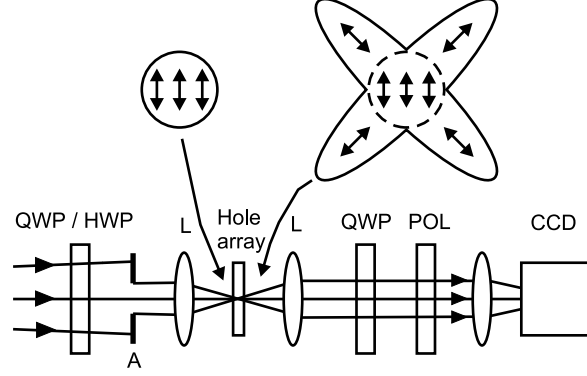


**Figure 9.1:** Experimental setup used to measure the Mueller matrix of the hole arrays. The incident polarization state is set by a quarter-wave plate (QWP) or half-wave plate (HWP); the output polarization state is measured with a combination of a QWP, polarizer (POL), and CCD. Lenses L form a symmetric telescope, with the hole array placed in its focus; an aperture (A) sets the maximum numerical aperture (opening angle  $\theta_A$ ) of the illumination. The two figures at the top contain sketches of the field profiles and local polarization (arrows) in transverse planes just in front of and behind a square hole array in which diagonal SP modes are excited. The incident circular field profile is distorted by the SP propagation to a shape with lobes in the propagation directions. The incident uniform vertical polarization is thus changed by the array to a nonuniform polarization distribution.

## 9.2 Model

A theoretical description of the depolarization properties of square and hexagonal hole arrays is simplified considerably by symmetry arguments. Under rotationally symmetric focusing, the Mueller matrix of a perfect square lattice of circular holes has been shown to be diagonal, with generally all  $M_i$  different [70]. For hexagonal lattices of circular holes, the Mueller matrix is diagonal as well, with an additional symmetry restriction in the form of the relation  $M_1 = M_2$ . For special cases, further relations between the  $M_i$  functions can be derived. In this paper we will do so by introducing an analytical model based upon two basic approximations, which we will apply in consecutive order. The first approximation is that we assume that the optical transmission of the hole array is carried by a single set of (SP) modes, which are frequency-degenerate for plane-wave illumination at normal incidence. This single-resonance approximation therefore assumes that the resonant SP wavevectors all have the same lengths and can be written, for instance for a square array, as  $\vec{k}_{SP} = (2\pi/a)(\pm m, \pm n)$  and  $(2\pi/a)(\pm n, \pm m)$  [1]. The integers  $n$  and  $m$  label the distance from the origin to a point  $|\vec{k}_{SP}|$  away on the reciprocal lattice of the hole array, with a real-lattice spacing  $a$ . After some initial calculations, we will introduce our second approximation, the Lorentzian-shape approximation. This assumes that the angular and frequency dependence of the amplitude transmission function are related in a simple way, both dependencies giving Lorentzian shapes around resonance.

In the single-resonance approximation, the transmission tensor  $t(\vec{\theta})$  evaluated at the SP resonance frequency can be written as

$$t(\vec{\theta}) = \sum_k f_k(\vec{\theta}) \vec{e}_k \otimes \vec{e}_k^T, \quad (9.1)$$

where the summation index  $k = \{0, \pm 1, \pm 2, \dots\}$ . The vector  $\vec{\theta} = (\theta_x, \theta_y)$  specifies the two components of the angle of incidence,  $\vec{e}_k^T$  is the transpose of the (normalized) SP propagation direction  $\vec{e}_k$  (i.e.,  $\vec{e}_k \parallel \vec{k}_{SP,k}$ ) and  $\otimes$  denotes the direct product. The summation is over pairs of counterpropagating SPs, because this allows us to easily implement symmetry relations. The scalar functions  $f_k(\vec{\theta})$  quantify the amplitude transmission that can be attributed to the  $k$ -th SP pair out of the considered set. The product  $\vec{e}_k \otimes \vec{e}_k^T$  describes the polarization properties that are determined by projection on  $\vec{e}_k$ , pointing in the propagation direction of the  $k$ -th SP pair. Note that Eq. (9.1) is also valid in the presence of a polarization-isotropic contribution to the transmission, as expected for the nonresonant or Bethe-type [2] transmission through the hole array, which we use in Section 9.4.

The rotational symmetry of the hole array is reflected in simple relations between the various  $f_k(\vec{\theta})$ 's and  $\vec{e}_k$ 's, which are taken in the direction of the reciprocal lattice vectors. To describe the lowest-order modes it is sufficient to assume, apart from the single-resonance condition, that we deal with either two SP pairs (fourfold frequency degenerate) for a square array or three SP pairs (sixfold frequency degenerate) for a hexagonal array. In this case, the elements  $M_i$  of the Mueller matrix can be expressed as linear combinations of two functions only. These functions quantify the integrated squared amplitude of a single SP pair and the overlap between neighbouring SP pairs, respectively, and are given by the real-valued expressions

$$A_{s,h} \equiv \int |f_k(\vec{\theta})|^2 d\theta_x d\theta_y, \quad (9.2a)$$

$$B_{s,h} \equiv \int f_k(\vec{\theta}) f_\ell^*(\vec{\theta}) d\theta_x d\theta_y. \quad (9.2b)$$

The integrals run over the angular range of illumination (assumed rotationally symmetric around the origin [74]),  $k$  and  $\ell$  label neighboring SP pairs, and the subscripts  $s$  and  $h$  label the array symmetry. If the illumination is nonuniform within the angular range but still obeys the lattice symmetry, the integrand should be multiplied by the input intensity profile  $I(\vec{\theta})$ .

Under the single-resonance condition described above, the Mueller matrix of a square array obeys the additional relations  $M_0 = M_1 = A_s$  and  $M_2 = M_3 = B_s$ , where the  $x$  axis is taken along an  $\vec{e}_k$  direction. The degree of polarization (DOP) for a polarization-pure input state, with  $S_0 = S_i = 1$  and  $S_j = 0$  for  $i \neq j$ , is  $\Pi_i \equiv \sqrt{\sum_m (M_{m0} + M_{mi})^2} / (M_{00} + M_{0i})$ . For our diagonal Mueller matrix  $\Pi_i = M_i / M_0$ , making  $\Pi_1 = 1$  and  $\Pi_2 = \Pi_3 = B_s / A_s$ . The explanation for the absence of depolarization for  $S_1 = \pm 1$  (pure  $x$ - or  $y$ -polarized) injection is simple: An optical transmission that is carried by only two orthogonal pairs of SP modes does not lead to depolarization if the incident polarization is orthogonal to the eigenpolarization of one pair. In this case, only the SP pair aligned with the input polarization can be excited, which then sets the (pure) output polarization. Only under this condition will polarization

dephasing be absent; in all other hole arrays, dephasing will be an unavoidable consequence of SP propagation.

For a hexagonal array the nonorthogonality between the eigenvectors  $\vec{e}_k$  leads to the slightly more complicated relations  $M_0 = (6A_h + 3B_h)/4$  and  $M_1 = M_2 = (3A_h + 6B_h)/4$ , which yield  $\Pi_1 = \Pi_2 = (A_h + 2B_h)/(2A_h + B_h)$ . The depolarization of circularly polarized input is governed by  $M_3 = 9B_h/4$  and  $\Pi_3 = 3B_h/(2A_h + B_h)$ . The relation  $\Pi_1 = \Pi_2 = (1 + \Pi_3)/2$  shows that the depolarization of linear-polarized light is half as strong as that of circularly polarized light:  $1 - \Pi_1 = 1 - \Pi_2 = (1 - \Pi_3)/2$ . For linearly polarized input, the DOP behind the hexagonal hole array is always at least 50%, because of the selective excitation and subsequent reradiation of the SP modes that are best aligned within the set of three pairs (see also the discussion of Fig. 9.3 below).

To obtain analytic expressions for  $A$  and  $B$ , we now impose the Lorentzian approximation mentioned above. First, we use the fact that there is a one-to-one correspondence between the angle and frequency dependence of the optical transmission. The SP dispersion relations [1,4] show that paraxial angle tuning in the SP direction  $\vec{e}_k$  leads to a linear shift of the resonance frequency:

$$\omega_{res,k}(\vec{\theta}) = \omega_0 / \{1 - \sin(\theta_k)/n_{eff}\} \approx \omega_0(1 + \theta_k/n_{eff}). \quad (9.3)$$

In this equation we took  $\theta_k = \vec{\theta} \cdot \vec{e}_k$  as the projected angle and introduced the SP resonance frequency for normal incidence  $\omega_0$  and the effective-refractive index  $n_{eff} = \sqrt{\epsilon/(\epsilon + 1)} (\approx 1$  for an air-metal boundary). Angle tuning in the direction orthogonal to  $\vec{e}_k$  over an angle  $\theta_\perp$  produces only minor spectral shifts of order  $\theta_\perp^2$ , which have been neglected. Second, the amplitude transmission spectrum at normal incidence is approximated by a (complex-valued) Lorentzian of the form

$$t(\omega) \propto 1/(\omega - \omega_0 + i\Delta\omega), \quad (9.4)$$

where  $\omega$  is the optical frequency and  $\Delta\omega$  is the spectral width of the transmission resonance. Experimentally obtained hole-array spectra usually show somewhat different lineshapes, but Lorentzians are a good starting point and keep the model manageable analytically. Finally, by combining Eqs. (9.3) and (9.4) we can write the angle-dependent amplitude transmission as

$$t(\vec{\theta}, \omega) \propto \sum_k \frac{1}{\omega - \omega_{res,k}(\vec{\theta}) + i\Delta\omega} = \sum_{pairs} f_k(\vec{\theta}), \quad (9.5)$$

where the last equation holds at the SP resonance frequency ( $\omega = \omega_0$ ) and  $f_k(\vec{\theta})$  is the function introduced in Eq. (9.1), summed over counterpropagating pairs with  $\vec{e}_k = -\vec{e}_\ell$ . When evaluated on resonance the SP pair transmission function is a (real-valued) Lorentzian:

$$f_k(\vec{\theta}) = C \left[ \frac{1}{\left(\frac{\theta_k}{\Delta\theta} + i\right) \Delta\omega} + \frac{1}{\left(-\frac{\theta_k}{\Delta\theta} + i\right) \Delta\omega} \right] = C \frac{\Delta\theta^2}{\theta_k^2 + \Delta\theta^2}, \quad (9.6)$$

with  $\Delta\theta \equiv n_{eff}\Delta\omega/\omega_0$ . Equation (9.6) is Fourier related to an electric field on the array that decays exponentially in the SP propagation direction. Using  $\theta = k_\parallel/k_0$ , the Fourier transform of a profile  $t(x) \propto \exp(-|x|/2\ell_{SP})$  becomes equal to Eq. (9.6) if we take  $\Delta\theta = \lambda_0/4\pi\ell_{SP}$ .

Apart from interference, Eqs. (9.1) and (9.6) predict that the overall angle-dependent intensity transmission  $|t(\tilde{\theta})|^2$  will look like two or three stripes that cross at  $90^\circ$  or  $60^\circ$  angles for the square and hexagonal array, respectively. Such patterns have indeed been observed experimentally: For the square array we refer to Chapter 6; for the hexagonal array we refer to Fig. 9.3, which will be discussed in more detail in Section 9.3.

With the proposed Lorentzian transmission model, a simple substitution in Eqs. (9.2) yields  $A$  and  $B$  as a function of the normalized opening angle  $\Theta \equiv \theta_A/\Delta\theta$  of a circular uniform input (aperture  $A$  in Fig. 9.1). The resulting expressions

$$A_s = A_h = \frac{\pi\Theta^2}{\sqrt{1+\Theta^2}} \quad (9.7a)$$

$$B_s = 2\pi \arctan\left(\frac{\Theta^2}{2\sqrt{1+\Theta^2}}\right), \quad (9.7b)$$

$$B_h = (4\pi/\sqrt{3}) \arctan\left(\frac{\sqrt{3}\Theta^2}{4\sqrt{1+\Theta^2}}\right), \quad (9.7c)$$

allow us to calculate both the  $M_i$ 's and the degrees of polarization  $\Pi_i$  as a function of the normalized opening angle  $\Theta$ .

The calculated DOPs  $\Pi_i$  ( $i=1,2,3$ ) for a square array, following from our model, are shown in Fig. 9.2(a). Note that  $\Pi_1 = 1$  and  $\Pi_2 = \Pi_3$  in this case, as stated above. The corresponding DOPs for a hexagonal array are shown in Fig. 9.2(b). In this case  $M_1 = M_2$  and  $M_1 + M_2 = 1 + M_3$ . In the limit of a very small opening angle, the DOP remains high for both square and hexagonal arrays, because  $\Pi_i \approx 1 - O(\Theta^4)$ . At large opening angles  $\Theta \gg 1$ , we expect  $\Pi_{3,s} \approx \pi/\Theta$  and  $\Pi_{3,h} \approx \pi\sqrt{3}/\Theta$  for the square and hexagonal arrays, respectively. The hexagonal array has a large  $\Theta$  limit of  $M_1 = M_2 \rightarrow 0.5$ , which is a consequence of the relation  $M_1 + M_2 - 1 = M_3$ . However, as our model is strictly paraxial, these large-angle limits are not expected to be very meaningful.

### 9.3 Comparison with experiment

We checked the validity of our model by a comparison with measured Mueller matrices of a square and a hexagonal hole array, as reported in Chapter 8. Recapitulating briefly, both arrays were made in 200 nm thick smooth Au films on a glass substrate. The square array was made with electron-beam lithography, with a lattice spacing of 700 nm and nominal hole diameter of 200 nm. The hexagonal array was made with ion-beam milling, with a lattice spacing of 886 nm and nominal hole diameter of 200 nm. Both arrays exhibit a transmission maximum around a wavelength of 810 nm, which for the square array is identified as a  $(\pm 1, \pm 1)$ -SP resonance on the glass-metal interface and for the hexagonal array as the lowest-order resonance on the air-metal interface. Note that in the following we continue to take the  $x$  direction (corresponding to  $S_1 = 1$ ) along one of the SP propagation directions, i.e., along one of the diagonals for the square array.

The experimental setup used to measure the diagonal Mueller elements is shown in Fig. 9.1. A linearly polarized Ti:Sapphire laser beam at a wavelength of 810 nm is passed



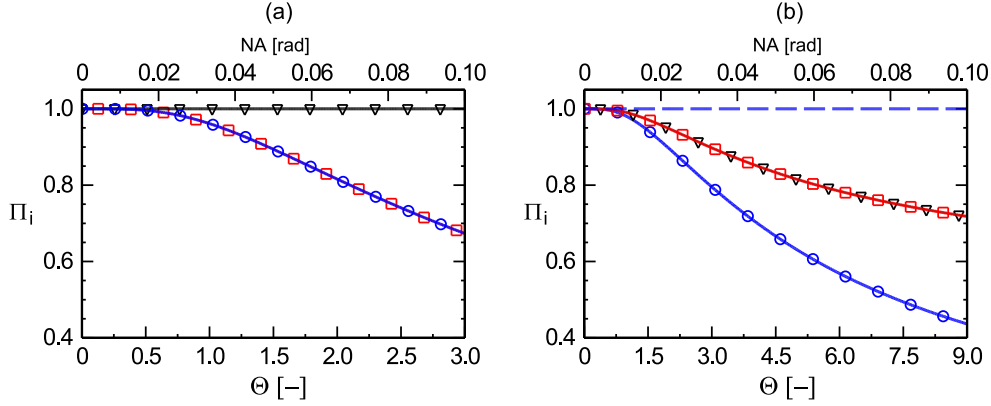


**Figure 9.2:** Theoretical DOP  $\Pi_i$  behind the (a) square and (b) hexagonal hole array as a function of the dimensionless quantity  $\Theta$  (lower scale) and the NA of the incident coherent light (upper scale), calculated with the Lorentz model; the multiplication factors relating the two scales are  $\Delta\theta = 1/30$  (square) and  $\Delta\theta = 1/90$  (hexagonal). Triangles are used for  $\Pi_1$ , squares for  $\Pi_2$ , and circles for  $\Pi_3$ .

through a  $10\ \mu\text{m}$  mode-cleaning pinhole (not shown), to homogeneously illuminate the input lens (L) of a symmetric telescope. After transmission through a hole array, positioned at the focus of the telescope, the light is imaged onto a CCD with a relay lens; the CCD is situated in the far field of the array. The SOP of the incident light is set by a rotatable quarter-wave or half-wave plate in front of the first lens. The Stokes parameters at the output are measured with a rotatable quarter-wave plate and polarizer positioned in front of the CCD. The obtained CCD images are further processed by summing the pixel intensities within circular regions of increasing radii centered on the telescope axis to yield plots of Stokes parameter values as a function of numerical aperture (NA). The hardware aperture (A in Fig. 9.1) is used to calibrate the NA scale. We performed a check of this method, by measuring intensity versus the NA both with hardware and software aperturing; these agreed well, indicating that lens aberrations can be neglected.

To illustrate the previously discussed depolarization mechanism, a measured far-field transmission pattern of the hexagonal array is shown in Fig. 9.3 for array illumination with horizontally oriented linearly polarized light and circularly polarized light. Figure 9.3(a) shows that a horizontal input polarization (indicated by the arrow in the inset) does not excite the SP pair that propagates in the vertical direction, but does excite the two remaining SP pairs. The lobe that is absent in Fig. 9.3(a) as compared to Fig. 9.3(b) is compact in the vertical direction, which by Fourier relations corresponds to a wide near-field distribution in this direction because of SP propagation. In other words, the high-intensity regions (lobes) in the far field are oriented orthogonal to the input polarization, which is indicated by the arrows around the edges of Fig. 9.3. Figure 9.3(b) shows that a circularly polarized input produces an equal distribution over all three excitable SP pairs, whereas a linearly polarized input can excite at most two pairs equally. After angular integration, this implies that  $M_1 = M_2$  should be larger than  $M_3$  for the hexagonal array, which is in agreement with the model prediction  $M_1 + M_2 - 1 = M_3$ . Note, that similar far-field patterns of the square array are discussed in

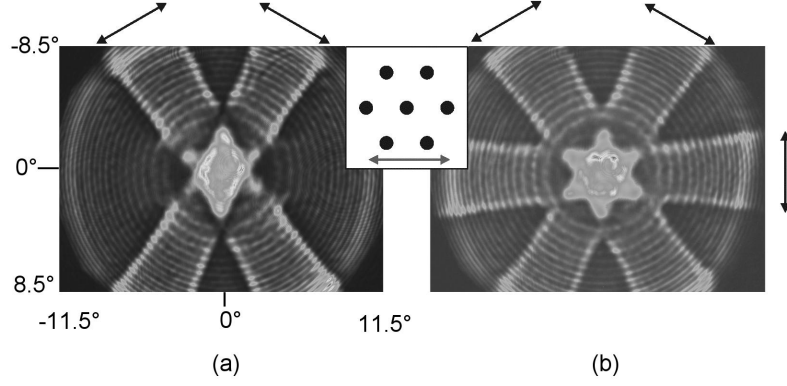


**Figure 9.3:** Measured far-field transmission of the hexagonal hole array for illumination with (a) horizontally oriented linear-polarized light (as indicated by the arrow in the inset) and (b) circularly polarized light. The pictures span  $23^\circ \times 17^\circ$  each. The inset shows the orientation of the array (lattice spacing 886 nm). The (predominant) polarization of the output lobes is indicated by the arrows around the figure edges.

#### Chapter 6.

Measurements of the DOPs of the hexagonal array are shown in Fig. 9.4(b) (from Chapter 8). As expected, the two linear input polarizations give the same output DOP, i.e.,  $\Pi_1 = \Pi_2$ . The predicted relation  $\Pi_3 = \Pi_1 + \Pi_2 - 1$  also holds very well. The agreement between the measurements and the predictions of our model (Fig. 9.2) is, however, not so good. This may be because of the slightly off-resonant illumination ( $\omega \neq \omega_0$ ) of the array, whereas the model is strictly valid only on resonance. An additional complication is that, probably because of production errors, the hexagonal array is not perfectly symmetric, as indicated by nonzero off-diagonal elements of the measured Mueller matrix (see Chapter 8). By fitting the model result to the measured curve, we estimate  $\ell_{SP} \approx 6 \pm 3 \mu\text{m}$  from the parameter  $\Delta\theta = \lambda_0 / (4\pi\ell_{SP})$ , where the large error bar is an indication for the limited quality of the fit.

The measured DOPs  $\Pi_i$  ( $i=1,2,3$ ) of the square hole array are shown in Fig. 9.4(a) (also from Chapter 8). The general shape of  $\Pi_2$  and  $\Pi_3$  is in reasonable agreement with the model results, and the observation  $\Pi_1 > \Pi_2, \Pi_3$  confirms the prediction that the depolarization should be smallest for input polarizations along the dominant SP propagation directions. However, the observations that  $\Pi_1 \neq 1$  and decreases for increasing NA, and that  $\Pi_2 \neq \Pi_3$ , shows that the single-resonance assumption does not hold well for our square array; although the glass-metal and air-metal interface play a different role in the transmission process (resonant versus nonresonant) the influence of the latter on the transmission apparently cannot be neglected. Fitting of  $\Delta\theta$ , similar to above, gives  $\ell_{SP} \approx 2 \pm 1 \mu\text{m}$  for the square array. Interestingly, the relation  $\Pi_3 = \Pi_1 + \Pi_2 - 1$  seems to hold for the square array as well, which indicates that this relation may be more generally valid than the model from which it was obtained.

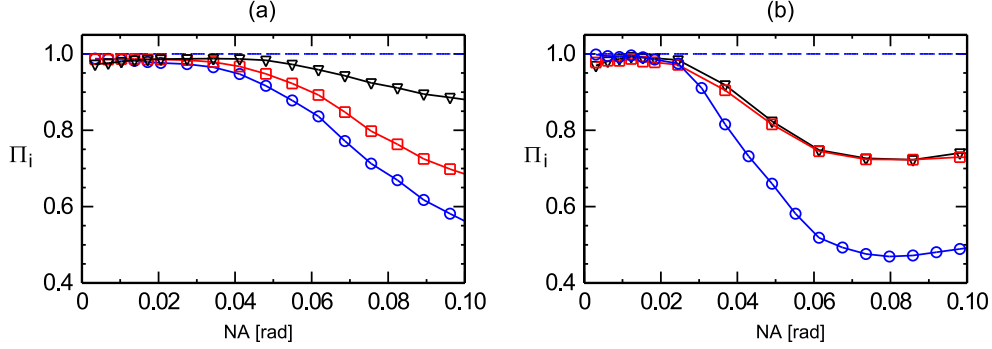


**Figure 9.4:** Measured DOP  $\Pi_i$  behind the (a) square and (b) hexagonal hole array as a function of the NA of the incident coherent light. Triangles are used for  $\Pi_1$ , squares for  $\Pi_2$  and circles for  $\Pi_3$ . Note that, for the square array,  $\Pi_1$  corresponds to a polarization along the array diagonals, i.e., the SP propagation directions; in Chapter 8 we used a different convention.

## 9.4 Model extensions

It is relatively easy to extend our model by incorporating more realistic resonant lineshapes as well as off-resonant excitation. This extension can in principle increase the accuracy of the model, but has the disadvantage that one loses the simple connection between SP propagation length and spectral and angular widths of the SP resonance. One good candidate for describing experimentally obtained spectra, is the Fano-type lineshape, which arises from interference between the resonant SP-mediated transmission and a nonresonant Bethe-type transmission [12, 53]. On the basis of a general Fano-type spectral line we can write the hole-array transmission function for the  $k$ -th SP pair [see Eq. (9.6)] as

$$f_k(\vec{\theta}, \omega) = C \left\{ 1 + \frac{\alpha + i\beta}{2} \left[ \frac{1}{\delta\omega - \left(\frac{\theta_k}{\Delta\theta}\right) + i} + \frac{1}{\delta\omega + \left(\frac{\theta_k}{\Delta\theta}\right) + i} \right] \right\}. \quad (9.8)$$

This function has three dimensionless parameters: The real and imaginary part  $\alpha$  and  $\beta$  of the Fano parameter determining the relative strength of resonant and nonresonant terms, and the relative frequency detuning  $\delta\omega \equiv (\omega - \omega_0)/\Delta\omega$ . In this description we have written the non-resonant term as a constant term of magnitude unity (i.e., 1). Note that we can easily regain Eq. (9.6) by inserting  $\delta\omega = 0$  and taking the limit  $\alpha \rightarrow \infty$  (to let the resonant term dominate). The accuracy of this description with regard to spectral data can be seen in Fig. 9.5. Here the measured transmission spectrum of our hexagonal array, for illumination with a nearly plane wave at normal incidence, is shown (black curve) together with a theoretical fit (gray curve), based on Eq. (9.9) with  $\theta_k = 0$ . The fit is of the shape  $C [(\lambda - a)^2 + b^2] / [(\lambda - c)^2 + d^2]$ , with the zero position  $a = 766.3$  nm,  $b = 0 (< 10^{-4})$  nm, the peak position  $c = 806.7$  nm and the half-width at half-maximum point  $d = 7.1$  nm. From these values we infer  $\alpha = -6.1$ ,  $\beta = -1$  (as a direct consequence of  $b = 0$ ), and  $\omega_0 = 2\pi c/806\text{nm} = 2.34 \times 10^{15}$  Hz. Note,

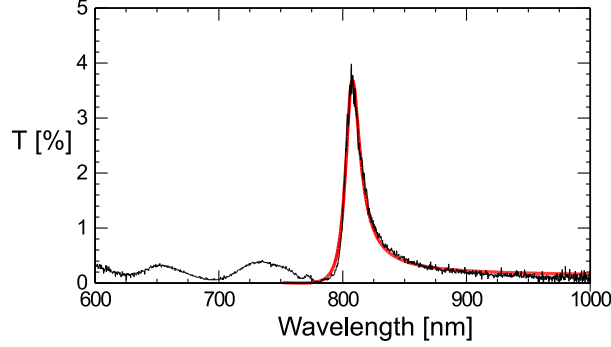


**Figure 9.5:** Measured transmission of the hexagonal hole array for illumination with an approximately plane wave at normal incidence (black). Also shown is a theoretical fit based upon a Fano-type model (gray).

that the restriction  $\beta = -1$  is already contained in the original Fano model [11].

To calculate the DOP as a function of the opening angle of the input light in this extended model, one can follow the recipe given above for the Lorentzian case. The integrals become more difficult, but remain analytically solvable. As the resulting expressions are quite lengthy, we will not list them here but discuss only two striking aspects. First, the DOP curves in this Fano-type description have a completely different asymptotic behavior, tending back to 1 for large opening angles. The reason is that the nonresonant contribution, which is polarization isotropic in our case (spherical holes), starts to dominate at large angles of incidence. Second, in the small-angle regime, the differences between the Fano-type and the simple Lorentzian model are relatively small for resonant ( $\delta\omega = 0$ ) excitation. For off-resonance excitation, however, the depolarization curves can deviate considerably.

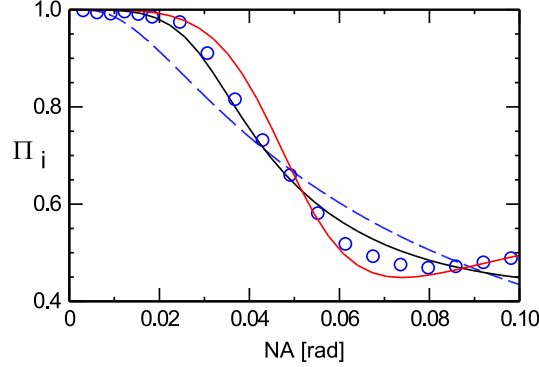


**Figure 9.6:** Measured DOP of the hexagonal hole array (circles) compared with the best fit obtained from the Lorentz model (dashed curve) and two theoretical fits based upon the Fano-type model: The dark solid curve belongs to values in agreement with the spectral fit of Fig. 9.5 with  $\alpha = -6.1$ ,  $\delta\omega = 2.50$  and  $\Delta\theta = 0.012$ ; the light solid curve corresponds to  $\alpha = -0.98$ ,  $\delta\omega = 1.02$  and  $\Delta\theta = 0.14$ .

Figure 9.6 shows how the experimental data for the hexagonal array compare with a fit

based on the Lorentzian model (dashed curve) and two fits based on the extended Fano-type model (solid curves). For the square array, fits of similar quality were obtained (not shown). Although the Fano model is clearly able to produce a better fit, both at large and at small NAs, the precise values needed for the best fit are somewhat unrealistic. The dark solid fit curve is based on the (realistic) Fano parameter deduced from the transmission spectrum, but needs a somewhat large detuning  $\delta \omega = 2.5$ , whereas the light solid curve fits better, but is based on  $\alpha = -0.98$ ,  $\beta = -1$  and  $\delta \omega = 1.02$ . The remaining deviations between model and experiment are most probably caused by a breakdown of the single resonance condition that formed the basis of Eq. (9.1). Deviations are expected if SP resonances on both interfaces are important or if other SP modes on the same interface, with different resonance wavelengths than those of the resonant set, are excited sufficiently.

## 9.5 Conclusion

We have described an analytic model for depolarization in metal hole arrays that is based on symmetry arguments and the additional assumption of a single Lorentzian SP resonance. Our polarization measurements confirm the overall expected depolarization features predicted by the model. At a more detailed level, a generalization to the Fano-type resonant structure was studied. The single-resonance assumption is both the strength and the weakness of our model. Its strength is that it allows for simple analytic expressions for the amount of depolarization. Its weakness is that its use is restricted to hole arrays in which only one set of SP modes dominates the optical transmission in a specific frequency range.

## Acknowledgements

We thank A. Aiello for his help with the computations; A. van Zuuk and E. van der Drift at the Delft Institute of Micro-Electronics and Sub-micron Technology (DIMES) in Delft, the Netherlands, and P. F. A. Alkemade at the Kavli Institute for Nanoscience, Delft, the Netherlands, for producing the hole array samples.

9. Analytic model of optical depolarization in square and hexagonal nanohole arrays

## CHAPTER 10

---

### Quantum decoherence versus classical depolarization in nanohole arrays

---

*We present a theoretical model of the quantum decoherence experienced by a pair of polarization-entangled photons, after one of them is sent through a nanohole array, and compare this with the classical depolarization experienced by light with a fixed polarization when this is sent through the same array. We discuss the conditions under which the quantum visibility and the classical degree of polarization are the same. Experimental verification is performed with arrays of square and hexagonal symmetry.*

*E. Altewischer, M.P. van Exter and J.P. Woerdman, accepted for publication in Phys. Rev. A.*

## 10.1 Introduction

Since the first experiment that demonstrated the extraordinary transmission of metal nanohole arrays [1], a number of studies have stressed the importance of the optical polarization and its relation to surface plasmon (SP) propagation [9, 13, 66, 67]. These issues show up most prominently if the array is illuminated with a strongly focused beam, since in this case the coupling of the SP propagation to the incident polarization leads to spatial nonuniformities. In a previous experiment the hole-array transmission was probed with single photons out of polarization-entangled photon pairs (see Chapter 4), i.e., with pairs where the polarization of each photon is *undetermined*, but quantum correlated to the other photon in the pair. This experiment showed that the entanglement could be fully transferred to the excited SPs for plane-wave illumination, but that quantum decoherence occurred for focused illumination (where the focal spot is still covering many holes).

In this paper we address the question how this observed quantum decoherence is related to the classical depolarization experienced by light with a *fully determined* polarization that passes through the nanohole array in an identical configuration. This distinction between *undetermined* and *determined* lies at the heart of quantum measurement theory and the interpretation of the projection postulate. Although a theoretical description of the quantum experiment has already been given in Ref. [75], we consider that description too complicated for practical use. Furthermore, there are several subtleties involved that took us some time to resolve experimentally. We will discuss the conditions under which both the classical depolarization and the quantum decoherence can be simply expressed in the angle- and polarization-dependent transmission (“transfer function”) of the hole array. Note that this description in terms of a transfer function does not depend on the details of the transmission process and is completely general in that respect. We present data for both the classical and the quantum experiments and compare these, for square as well as for hexagonal arrays. Special attention is given to an averaging procedure that allows one to remove spurious effects of linear anisotropies in practical hole arrays (see Appendix).

## 10.2 Theoretical comparison of classical depolarization and quantum decoherence

We start our theoretical description of classical depolarization by recapitulating the transmission properties of a hole array in the paraxial limit. Restricting ourselves to the zeroth-order diffraction, these properties can be fully captured in a  $2 \times 2$  transfer matrix  $t(\vec{\theta}, \omega)$ , which relates the optical input field at angle of incidence  $\vec{\theta}$  and frequency  $\omega$  to the output field at the same angle and frequency:

$$\vec{E}_{out}(\vec{\theta}, \omega) = t(\vec{\theta}, \omega) \vec{E}_{in}(\vec{\theta}, \omega). \quad (10.1)$$

Depolarization can occur when an array is illuminated with a wide-angle beam and the transfer matrix also shows a combined angular and polarization dependence, producing different output polarizations for the same input polarization at different angles of incidence. This process can be fully quantified by measuring the  $(4 \times 4)$  Mueller matrix, which relates the spatially averaged input to output polarizations via Stokes vectors [68, 69].



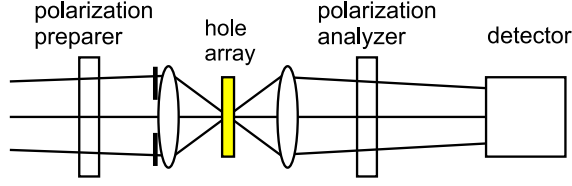


**Figure 10.1:** The setup used for the classical polarization experiment, with the source a Ti:sapphire laser at 813 nm wavelength (on the left, not shown). The input polarization state is prepared by a combination of polarizer and half-wave plate, and analyzed with a polarizer. The hole array is centered inside the confocal one-to-one telescope.

For perfectly square and hexagonal hole arrays the Mueller matrix is diagonal [70], with elements  $M_{ii}$  ( $i = 0, 1, 2, 3$ ), and it suffices to express the depolarization by the three numbers  $\Pi_i \equiv M_{ii}/M_{00}$ . These quantities are equal to the degree of polarization (DOP) [68, 69] of the output light of the array for linear input polarization along  $0^\circ$  (corresponding to  $i = 1$ ) and  $45^\circ$  ( $i = 2$ ), and circular input polarization  $\sigma^+$  ( $i = 3$ ), respectively;  $M_{00}$  is the transmitted power for unpolarized input light. In practice, off-diagonal elements of the Mueller matrix cannot always be neglected due to array imperfections (see Chapter 8). However, even in this case, the  $\Pi_i$  remain useful to characterize the polarization behavior of such arrays, provided that the off-diagonal elements are small compared to the diagonal elements. The  $\Pi_i$  are approximately equal to the average of the DOPs of the output light of the array for input polarizations corresponding to  $i$  and to its orthogonal direction, respectively (see Appendix); therefore we can use the term DOP for  $\Pi_i$  also in the case of slightly nonperfect arrays.

The degrees of polarization  $\Pi_i$  can be determined experimentally with the setup shown in Fig. 10.1. Here a hole array is illuminated with light of a given spectral and angular bandwidth, where the latter is set by a lens, with focal length  $f$ , plus a diaphragm. To determine the DOP, we use an averaging procedure conforming to the discussion above, where for each  $i$  two input polarizations are prepared, one corresponding to  $i$  and one to its orthogonal direction. Subsequently, for each input polarization, the power of the output beam  $P_{\parallel}$  and  $P_{\perp}$  is measured for settings of the analyzer parallel and perpendicular to the preparer, respectively. The  $\Pi_i$  is then computed from

$$\Pi_i = \frac{P_{\parallel}^{av} - P_{\perp}^{av}}{P_{\parallel}^{av} + P_{\perp}^{av}}, \quad (10.2)$$

where each quantity is the average over the two orthogonal input polarizations. In this paper, we will concentrate on two specific choices for the input polarization, namely  $0^\circ$  and  $45^\circ$ . By expressing the optical fields in terms of Stokes parameters and using the fact that the incident field is transformed by the hole array via

$$E(\vec{\theta}, \omega)\vec{e}_H \rightarrow t_{HH}(\vec{\theta}, \omega)E(\vec{\theta}, \omega)\vec{e}_H + t_{VH}(\vec{\theta}, \omega)E(\vec{\theta}, \omega)\vec{e}_V, \quad (10.3)$$

one can express the degree of polarization  $\Pi$  in terms of the input field and the elements of

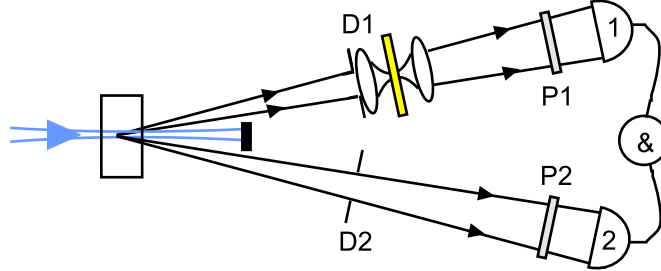


**Figure 10.2:** The SPDC setup used in the quantum experiment, with the source a non-linear BBO crystal plus the standard compensation scheme of half-wave plate and compensating crystals (not shown in detail). The hole arrays are placed inside the confocal telescope in one of the beams.

the transmission matrix  $t$  as:

$$\Pi_{0^\circ} = \frac{\langle\langle (|t_{HH}|^2 - |t_{VH}|^2 + |t_{VV}|^2 - |t_{HV}|^2) |E|^2 \rangle\rangle}{\langle\langle (|t_{HH}|^2 + |t_{VH}|^2 + |t_{VV}|^2 + |t_{HV}|^2) |E|^2 \rangle\rangle} \quad (10.4a)$$

$$\Pi_{45^\circ} = \frac{\langle\langle 2\text{Re}\{t_{HH}t_{VV}^* + t_{VH}t_{HV}^*\} |E|^2 \rangle\rangle}{\langle\langle (|t_{HH}|^2 + |t_{VH}|^2 + |t_{VV}|^2 + |t_{HV}|^2) |E|^2 \rangle\rangle}. \quad (10.4b)$$

Here the double brackets denote the integration over all angles and frequencies contained in the beam, and the input intensity  $|E|^2$  should have identical angular and spectral distributions for each of the four measurements.

Although Eqs. (10.4a) and (10.4b) are strictly valid, their relation to the experimental configuration of Fig. 10.1 is straightforward only if the illumination has sufficient spatial coherence. This is a valid assumption if the illumination of the telescope-input lens has a negligible wave-vector spread; alternatively, this assumption can be formulated in terms of the size of the focus inside the telescope: this has to be much smaller than the beam size on the telescope lenses, as can be seen from ray-optics arguments. Under this condition the internal angle  $\vec{\theta}$  inside the telescope can be mapped one-to-one to the transverse position  $\vec{r}$  on the input lens via  $\vec{\theta} = -\vec{r}/f$ . Assuming this makes our description much simpler than that of Ref. [75]; we consider the angle-dependent transmission of the hole array  $t(\vec{\theta}, \omega)$ , which in Ref. [75] is denoted by  $\mathbb{F}(\vec{q}_2)$ , to be the only physically relevant quantity.

The quantum decoherence experienced by polarization-entangled photons depends on the biphoton state or amplitude function, just as the classical depolarization depends on the (one-photon) field  $E$ . Most descriptions of polarization-entangled photons start from the biphoton state:

$$|\psi\rangle = \frac{1}{\sqrt{2}} (|H_1 V_2\rangle + e^{i\alpha} |V_1 H_2\rangle), \quad (10.5)$$

where the two photons, with horizontal and vertical polarizations, travel along directions labeled by 1 and 2. For instance, in the standard type-II spontaneous parametric down conversion (SPDC) setup, as shown in Fig. 10.2, a nonlinear crystal is able to convert an incident pump photon to two orthogonally polarized photons at the double wavelength, which are emitted along two intersecting cones. At the exact crossings of these cones the polarization

of the individual photons is undetermined, and Eq. (10.5) correctly describes the polarization properties of the biphoton state if the spatial and frequency selection is sufficiently narrow. In an experiment, this state can only be produced approximately, because the photons can also be labeled by their frequency and wave vector. Both of these have to be taken into account because a practical detector will measure a finite part of the crossings, set by the apertures in Fig. 10.2, within a finite frequency window. In this case, the paraxially exact SPDC state behind the apertures at the ring crossings can be written as:

$$|\psi\rangle = \int d\vec{q}_1 d\vec{q}_2 d\omega_1 d\omega_2 [\Phi_{HV}(\vec{q}_1, \omega_1; \vec{q}_2, \omega_2) |H, \vec{q}_1, \omega_1; V, \vec{q}_2, \omega_2\rangle + \Phi_{VH}(\vec{q}_1, \omega_1; \vec{q}_2, \omega_2) |V, \vec{q}_1, \omega_1; H, \vec{q}_2, \omega_2\rangle], \quad (10.6)$$

showing explicitly the wave vector  $\vec{q}$  and frequency  $\omega$  dependent (two-photon) amplitude functions  $\Phi_{ij}$  ( $i, j = H, V$ ) for each of the two-photon combinations [30]. The integration is over the angular area contained in the apertures and the frequency window of the detectors.

A simple experimental measure for the degree of entanglement can be obtained from the two-photon fringe visibility:

$$V_{\phi_1} \equiv \frac{R_{Max}^{av} - R_{Min}^{av}}{R_{Max}^{av} + R_{Min}^{av}}, \quad (10.7)$$

which can take values between 0 and 1. It is measured in the setup of Fig. 10.2 by setting the transmission axis of one of the polarizers at the appropriate  $\phi_1$  and  $\phi_1 + \pi/2$ , respectively, and measuring in each case the maximum and minimum coincidence rates  $R_{max}$  and  $R_{min}$  at the corresponding settings of the second polarizer. By defining the visibility  $V$  in terms of the coincidence rates  $R_{av}$  averaged over the two input settings the visibility becomes more robust against imperfections of the hole array that will be considered below, in a manner analogous to the discussion above for the DOP  $\Pi_i$ .

For a type-II SPDC source, producing the state  $|\psi\rangle$  of Eq. (10.6), the visibility in the linear polarization basis oriented at  $0^\circ$  with respect to the crystal axes (along H and V) is always 1 because there is no interference between  $\Phi_{HV}$  and  $\Phi_{VH}$  in this case. The visibility along  $45^\circ$  however is given by

$$V_{45^\circ} = \frac{\langle\langle 2\text{Re}(\Phi_{HV}\Phi_{VH}^*) \rangle\rangle}{\langle\langle |\Phi_{HV}|^2 + |\Phi_{VH}|^2 \rangle\rangle}, \quad (10.8)$$

where the brackets denote the integration over  $\vec{q}$  and  $\omega$ . Therefore the source produces perfectly polarization-entangled photons ( $V_{45^\circ} = 1$ ) only if  $\Phi_{HV}$  and  $\Phi_{VH}$  are identical within the considered angular and frequency bandwidths. This is the case for either an infinitely thin crystal or a properly corrected thick crystal [20], followed by detection within sufficiently small angular and frequency windows. Note that the overlap integral of  $\Phi_{HV}$  and  $\Phi_{VH}$  in the numerator has the shape of a coherence function, so that two perfectly entangled photons can be considered to be mutually fully coherent (within the considered angular and spectral bandwidths). This two-photon coherence is independent of the one-photon coherence of each of the beams separately; in fact, the one-photon properties of a SPDC source are indistinguishable from those of a thermal source with identical bandwidths [76].

By putting a hole array (with transmission matrix  $t$ ) at the focus of a confocal telescope in beam 1 of the SPDC setup (see Fig. 10.2) the SPDC state is changed in the following way:

$$\int d\vec{q}_{1,2} d\omega_{1,2} \Phi_{HV} |H, \vec{q}_1, \omega_1; V, \vec{q}_2, \omega_2\rangle \longrightarrow \int d\vec{q}_{1,2} d\omega_{1,2} \Phi_{HV} \times \left\{ t_{HH}(\vec{\theta}_1, \omega_1) |H, \vec{q}_1, \omega_1; V, \vec{q}_2, \omega_2\rangle + t_{VH}(\vec{\theta}_1, \omega_1) |V, \vec{q}_1, \omega_1; V, \vec{q}_2, \omega_2\rangle \right\}, \quad (10.9)$$

and analogously for the  $|VH\rangle$  term. We again assume “sufficient spatial coherence” and, additionally, that the telescope input lens is in the far field of the source. This allows us to relate the angle inside the telescope  $\vec{\theta}$  to the transverse momentum of the photon  $\vec{q}$  as  $\vec{\theta}_1 = -L\vec{q}_1/(fk)$ , where  $L \gg f$  is the distance from the input lens to the source and  $k = 2\pi/\lambda$ . Because the hole array can create additional  $|HH\rangle$  and  $|VV\rangle$  terms, the visibilities observed behind the hole array (see Fig. 10.2) are given by

$$V_{0^\circ} = \frac{\langle\langle (|t_{HH}|^2 - |t_{VH}|^2) |\Phi_{HV}|^2 + (|t_{VV}|^2 - |t_{HV}|^2) |\Phi_{VH}|^2 \rangle\rangle}{\langle\langle (|t_{HH}|^2 + |t_{VH}|^2) |\Phi_{HV}|^2 + (|t_{VV}|^2 + |t_{HV}|^2) |\Phi_{VH}|^2 \rangle\rangle} \quad (10.10a)$$

$$V_{45^\circ} = \frac{\langle\langle 2\text{Re}\{\Phi_{HV}\Phi_{VH}^*(t_{HH}t_{VV}^* + t_{VH}t_{HV}^*)\} \rangle\rangle}{\langle\langle (|t_{HH}|^2 + |t_{VH}|^2) |\Phi_{HV}|^2 + (|t_{VV}|^2 + |t_{HV}|^2) |\Phi_{VH}|^2 \rangle\rangle}. \quad (10.10b)$$

If we now compare Eqs. (10.4a), (10.4b), (10.10a) and (10.10b), we see that for perfectly entangled photons, i.e.,  $\Phi_{HV} = \Phi_{VH} = \Phi$ , the input one-photon distribution  $|E|^2$  in the classical experiment and the two-photon distribution  $|\Phi|^2$  in the quantum experiment play the same role, i.e.,  $\Pi_i = V_i$  if  $|E|^2 = |\Phi|^2$ . We repeat that the identity  $\Pi_i = V_i$  is only valid under the following additional restrictions: (i) The input angular distribution  $|E|^2$  should be identical for all input polarizations in the classical measurements, (ii) the entangled-photon source should be of high quality, i.e.,  $\Phi_{HV} \approx \Phi_{VH}$ , and (iii) the telescope should be a perfect (double) Fourier transformer.

### 10.3 Experimental comparison of classical depolarization and quantum decoherence

For an experimental verification of the theoretical expectations given above, we have used two different hole arrays, one with a square and one with a hexagonal hole patterning. Both consisted of a 200 nm-thick gold layer on a 0.5 mm-thick glass substrate with a 2 nm-thick bonding layer (of either titanium or chromium) in between. The square array was made with electron-beam lithography and had a lattice spacing of 700 nm and a nominal hole diameter of 200 nm. The hexagonal array was made with ion-beam milling and had a lattice spacing of 886 nm with again a nominal hole diameter of 200 nm. Figure 10.3 shows measured transmission spectra of the square array (black curve) and the hexagonal array (gray curve). At the experimental wavelength of 813 nm the resonant modes can be assigned to the glass-metal  $(\pm 1, \pm 1)$  and the air-metal  $(1, 0, 0)$ ,  $(0, 1, 0)$ , and  $(0, 0, 1)$  modes for the square and hexagonal array, respectively. The insets in Fig. 10.4 show scanning electron microscope pictures of the two arrays.

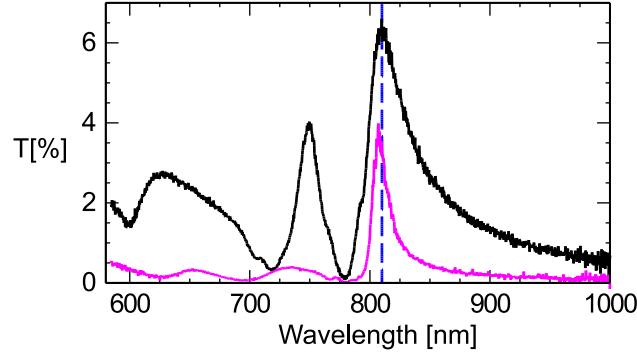


**Figure 10.3:** Transmission spectra under almost plane-wave illumination at normal incidence for the square (black curve) and hexagonal array (gray curve). The dashed vertical line indicates the resonance wavelength of 813 nm used in the experiments.

The classical depolarization induced by the hole arrays was measured with the setup shown in Fig. 10.1. A Ti:sapphire laser beam (wavelength 813 nm) is weakly focused on a 10- $\mu\text{m}$  diameter pinhole which is positioned at 50 cm in front of a 15-mm focal length lens; the pinhole diffracts the beam enough to produce a nearly plane-wave illumination of the lens. A diaphragm in front of the lens sets the maximum opening angle of the light impinging on the hole array, which is positioned at the focal plane. The transmitted light is recollimated by an identical 15 mm-focal length lens. The far field of the hole-array transmission is then imaged onto a CCD by a relay lens, making the positions on the CCD correspond to angles in the array illumination. The input polarization state is prepared by a combination of polarizer and half-wave plate in front of the first lens. A polarizer behind the second lens constitutes the polarization analyzer. To determine the total power within a given opening angle of the output (and input) beam the intensities per pixel of the CCD image were summed within a circle of corresponding radius. We checked that this software procedure gave the same result as setting the input-beam opening angle with the diaphragm, thus showing that lens aberrations are negligible. Further details of the experimental setup are given in Chapter 8.

The measured DOP curves ( $\Pi_i$  versus opening angle) for the square (a) and hexagonal (b) array are marked with solid symbols and solid lines in Fig. 10.4. These results are discussed in Chapter 8. Circles denote measurements with input polarization along  $0^\circ$  (gray arrows in inset) and squares with input polarization along  $45^\circ$  (black arrows). For the square array, the decrease in  $\Pi_{0^\circ}$  upon increasing the numerical aperture [27] (NA) is stronger than that of  $\Pi_{45^\circ}$ , because of the  $(\pm 1, \pm 1)$  propagation directions of the resonant SPs on this array (see Chapter 8). For the hexagonal array the equality  $\Pi_{0^\circ} = \Pi_{45^\circ}$  holds, as expected from general symmetry arguments [70]. The faster decrease of both  $\Pi$ 's of the hexagonal array as compared to the square array is caused by the smaller resonance linewidth and therefore larger SP lifetime of the hexagonal array (see Fig. 10.3 and Chapter 8). A more detailed analysis of the measured  $\Pi_i$ 's and a comparison with a Fano-type model is discussed in Chapter 9.

The quantum decoherence was measured with the setup shown in Fig. 10.2 (see Chapter 4). A BBO crystal is pumped by a continuous-wave Kr-ion laser beam (wavelength 406.7 nm) in a type-II SPDC scheme. The down-converted photons at the ring crossings

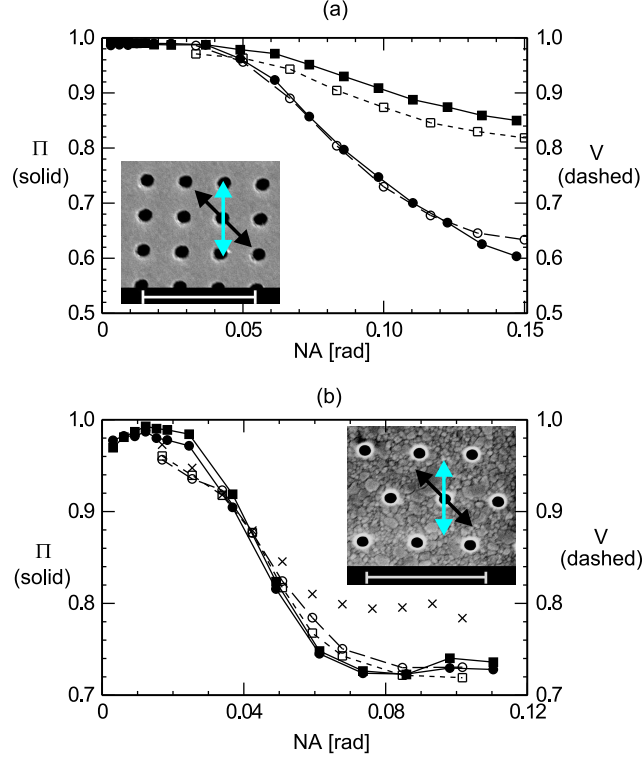


**Figure 10.4:** Measured degree of polarization  $\Pi_i$  (solid lines and symbols) and two-photon visibility  $V_i$  (dashed lines and open symbols) for (a) the square and (b) the hexagonal array. In both figures the polarization bases are  $0^\circ$  (circles) and  $45^\circ$  (squares). The insets show scanning electron microscope pictures of the arrays (scale bar  $2 \mu\text{m}$ ) with arrows indicating the incident polarizations of  $0^\circ$  (light) and  $45^\circ$  (dark). The crosses in (b) are measured with a smaller SPDC aperture in beam 2 (4 mm diameter, equivalent to  $\text{NA} \approx 0.068$  at the array position).

are selected by two variable-aperture diaphragms D1 and D2 and further frequency selection was applied by two 10 nm full-width-half-maximum frequency filters centered at the degenerate-frequency point of 813 nm. After passing through polarizers P1 and P2, the photons are detected with APD's. The rate of coincidences is determined with an AND gate (2 ns time window) coupled to a counter. To compensate for birefringence-related walk-off effects we used the standard compensator comprising a half-wave plate and two BBO crystals, each having half the thickness of the generating crystal [20]. Finally, the hole array was positioned at the focus of a one-to-one telescope, with the first lens positioned directly behind the diaphragm D1. For the square and the hexagonal array two 15-mm and 30-mm focal length lenses were used, respectively; the weaker lenses were used to obtain more accurate data at low NA values. In the absence of hole arrays we regularly obtained coincidence count rates of  $40 \times 10^3 \text{ s}^{-1}$  with  $V_{0^\circ} = 99.6\%$  and  $V_{45^\circ} = 96.0\%$  for a setting of the diaphragm D1 at 4.0 mm and diaphragm D2 at 8.0 mm diameter. Note that even for an empty telescope,

on the basis of Eq. (10.6) we expect a slight decrease of  $V_{45^\circ}$  with increasing NA, because  $\Phi_{HV} \neq \Phi_{VH}$ . This is confirmed by measurements: from fully closed (1 mm diameter) to fully open (6 mm) lens apertures we obtain count rates of 2 to  $110 \times 10^3 \text{ s}^{-1}$  and  $V_{45^\circ} = 98.4\%$  to 91.2%, whereas  $V_{0^\circ}$  was constant at 99.6%. From this perspective, the spectral detection bandwidth plays a similar role as the angular aperture width; the 10 nm filters were found to be sufficiently narrow as compared to both the spectral width of the SPDC source and the linewidth of the transmission spectra of both arrays.

The measured quantum visibility curves ( $V_i$  versus NA) are shown with dashed symbols and dashed lines in Fig. 10.4, to enable direct comparison with the classical depolarization. An input polarization of  $0^\circ$  is denoted by circles and  $45^\circ$  by squares. Note that the visibility axis has the same scale as the DOP axis. By comparing the two sets of curves in Figs. 10.4(a) and 10.4(b) we see that there is a good agreement between the visibility  $V_i$  and DOP  $\Pi_i$ , which confirms the theoretical discussion given above. The consistently slightly lower value of  $V_{45^\circ}$  as compared to  $\Pi_{45^\circ}$  for the square array is probably caused by the limited quality of the source ( $V_{45^\circ} < 1$ ). The slight deviation of the small-NA points for the hexagonal array might be caused by a slight misalignment of the telescope axis c.q. array surface normal with respect to the center of diaphragm D1. Note that in both the classical and the quantum measurements the previously discussed averaging procedure in the measurements of  $\Pi_i$  and  $V_i$  was applied because our hexagonal array was not of perfect symmetry (see Chapter 8).

To illustrate a case where the quantum and classical results seem to differ due to a violation of the restrictions discussed earlier, the crosses in Fig. 10.4(b) show a measurement of  $V_{45^\circ}$  that was made with diaphragm D2 set at a diameter of 4 mm (equivalent to  $\text{NA} \approx 68 \text{ mrad}$ ). Compared to the previously discussed measurement (with D2 at 8 mm diameter), the crossed  $\Pi$  points start to deviate at an NA of approximately 50 mrad and become constant at approximately 70 mrad. Mathematically, the size of the aperture D2 determines the integration range in Eqs. (10.10); a smaller integration range leads to a larger visibility. A more conceptual explanation can be given in terms of the Klyshko picture [77]: a photon starting at detector 2 and travelling back along beam 2 is diffracted by diaphragm D2 and, after reflection on the pump-spot mirror, no longer provides for a uniform illumination of the aperture of the lens in beam 1.

## 10.4 Conclusions

In conclusion, we have reported an experimental comparison between the classical depolarization and the quantum decoherence induced by subwavelength metal hole arrays of square and hexagonal symmetry. We find that there is an identity relation between two suitable measures of these effects, for ideally prepared input sources. This identity relation can theoretically be completely expressed in the hole array transmission tensor. Deviations show up if the input sources are not polarization isotropic or have insufficient spatial coherence.

## Acknowledgement

We thank A. van Zuuk and E. van der Drift at the Delft Institute of Micro-Electronics and Sub-micron Technology (DIMES) in Delft, the Netherlands, and P. F. A. Alkemade at the

Kavli Institute for Nanoscience, Delft, the Netherlands, for producing the hole array samples.

## Appendix

### 10.A Degree of polarization for nonperfect arrays

To be able to characterize the depolarization induced by square and hexagonal arrays which have some (slight) symmetry deformations, we extend the definition of the degree of polarization (DOP) as follows. In the simplest case, we can define a measure for the depolarization of a system in terms of the Stokes vector of the output light:

$$\Pi_i \equiv \left( \frac{S_i}{S_0} \right)_{out} = \frac{P_{\parallel} - P_{\perp}}{P_{\parallel} + P_{\perp}}, \quad (10.11)$$

for a fully polarized input  $S_{in} = (1, \delta_{i1}, \delta_{i2}, \delta_{i3})$  ( $i = 1, 2, 3$ ). The  $\Pi_i$  so-defined are only equal to the DOP of the output light if the output Stokes vector contains the same two zero components as the input Stokes vector, i.e., if the medium can be described by a diagonal Mueller matrix.

A more generally useable measure for depolarization can be defined by symmetrizing  $\Pi_i$  with respect to the input Stokes vectors:

$$\Pi_i^{av} \equiv \frac{S_i^+ - S_i^-}{S_0^+ + S_0^-} = \frac{P_{\parallel}^+ + P_{\parallel}^- - (P_{\perp}^+ + P_{\perp}^-)}{P_{\parallel}^+ + P_{\perp}^+ + P_{\parallel}^- + P_{\perp}^-} = \frac{M_{ii}}{M_{00}}, \quad (10.12)$$

where  $S_i^{\pm} \equiv S_i^{out}$  for  $S^{in} = (1, \pm\delta_{i1}, \pm\delta_{i2}, \pm\delta_{i3})$ . This expression is exactly equal to the respective diagonal Mueller-matrix element  $M_{ii}$ , normalized to  $M_{00}$ , as indicated by the last equality in Eq. (10.12). If the nondiagonal elements of the Mueller matrix are small compared to the diagonal elements,  $\Pi_i^{av}$  is also approximately equal to the average of the DOP's of the output light for both input Stokes vectors. This follows from a Taylor expansion of the DOP's via

$$\begin{aligned} \frac{DOP^+ + DOP^-}{2} &= \frac{1}{2} \left( \frac{\sqrt{(M_{10} + M_{1i})^2 + (M_{20} + M_{2i})^2 + (M_{30} + M_{3i})^2}}{M_{00} + M_{0i}} \right. \\ &\quad \left. + \frac{\sqrt{(M_{10} - M_{1i})^2 + (M_{20} - M_{2i})^2 + (M_{30} - M_{3i})^2}}{M_{00} - M_{0i}} \right) \\ &\approx \frac{M_{ii}}{M_{00}} \left( 1 + \frac{\sum_{j \neq i}^{j \neq 0} M_{j0}^2 + M_{ji}^2}{2M_{ii}^2} - \frac{M_{0i}M_{i0}}{M_{00}M_{ii}} + \frac{M_{0i}^2}{M_{00}^2} \right). \end{aligned} \quad (10.13)$$

The  $DOP^+$  and  $DOP^-$  are each sensitive to first-order in the relative strength of the off-diagonal elements  $M_{ij}$ . However, as the respective first-order terms differ in sign, the averaging removes these terms to leave only terms of second-order and higher. The final expression is accurate for  $M_{ij} \ll M_{ii}$  (for  $i \neq j$ ) (Note,  $M_{00} \geq M_{ii}$  always). In the main text we will use  $\Pi^{av}$  only, and drop the “av” superscript label.



---

## Bibliography

---

- [1] T.W. Ebbesen, H.J. Lezec, H.F. Ghaemi, T. Thio & P.A. Wolff, "Extraordinary optical transmission through sub-wavelength hole arrays," *Nature* **391**, 667-669 (1998).
- [2] H. A. Bethe, "Theory of diffraction by small holes," *Phys. Rev.* **66**, 163-182 (1944).
- [3] C.J. Bouwkamp, "Diffraction theory," *Rep. Prog. Phys.* **17**, 35-100 (1954).
- [4] H.F. Ghaemi, T. Thio, D.E. Grupp, T.W. Ebbesen & H. Lezec, "Surface plasmons enhance optical transmission through subwavelength holes," *Phys. Rev. B* **58**, 6779-6782 (1998).
- [5] L. Martin-Moreno, F.J. Garcia-Vidal, H.J. Lezec, K.M. Pellerin, T. Thio, J.B. Pendry & T.W. Ebbesen, "Theory of extraordinary optical transmission through subwavelength hole arrays," *Phys. Rev. Lett.* **86**, 1114-1117 (2001).
- [6] E. Popov, M. Nevière, S. Enoch & R. Reinisch, "Theory of light transmission through subwavelength periodic hole arrays," *Phys. Rev B* **62**, 16100-16108 (2000).
- [7] Q. Cao and P. Lalanne, "Negative role of surface plasmons in the transmission of metallic gratings with very narrow slits," *Phys. Rev. Lett.* **88**, 057403 (2002).
- [8] H.F. Schouten, T.D. Visser, G. Gbur, D. Lenstra and H. Blok, "Connection between phase singularities and the radiation pattern of a slit in a metal plate," *Phys. Rev. Lett.* **93**, 173901 (2004); "Creation and annihilation of phase singularities near a sub-wavelength slit," *Opt. Exp.* **11**, 371-380 (2003).
- [9] K.J.K. Koerkamp, S. Enoch, F.B. Segerink, N.F. van Hulst, L. Kuipers, "Strong influence of hole shape on extraordinary transmission through periodic arrays of subwavelength holes," *Phys. Rev. Lett.* **92**, 183901 (2004).
- [10] H.J. Lezec and T. Thio, "Diffracted evanescent wave model for enhanced and suppressed optical transmission through subwavelength hole arrays," *Opt. Expr.* **12**, 3629-3651 (2004).
- [11] U. Fano, "Effects of configuration interaction on intensities and phase shifts," *Phys. Rev.* **124**, 1866-1878 (1961).
- [12] C. Genet, M.P. van Exter, and J.P. Woerdman, "Fano-type interpretation of red shifts and red tails in hole array transmission spectra," *Opt. Commun.* **225**, 331-336 (2003).

## Bibliography

- [13] H. Raether, *Surface Plasmons* (Springer, Berlin, 1988).
- [14] A. Einstein, B. Podolsky and N. Rosen, “Can Quantum-Mechanical Description of Physical Reality Be Considered Complete?”, *Phys. Rev.* **47**, 777-780, (1935).
- [15] P. Benioff, “The computer as a physical system - a microscopic quantum-mechanical hamiltonian model of computers as represented by turing-machines,” *J. Stat. Phys.* **22**, 563-591 (1980).
- [16] R.P. Feynman, “Quantum mechanical computers,” *J. Opt. Soc. Am. B* **1**, 464-464 (1984); *Optics News* **11**, 11-20 (1985); *Found. Phys.* **16**, 507-531 (1986).
- [17] H.K. Lo, T. Spiller and S. Popescu, *Introduction to quantum computation and information* (World Scientific, 2001).
- [18] Z.Y. Ou and L. Mandel, “Violation of Bell’s inequality and classical probability in a two-photon correlation experiment,” *Phys. Rev. Lett.* **61**, 50-53 (1988).
- [19] J.G. Rarity and P.R. Tapster, “Experimental violation of Bell’s inequality based on phase and momentum,” *Phys. Rev. Lett.* **64**, 2495-2498 (1990).
- [20] P.G. Kwiat, K. Mattle, H. Weinfurter, A. Zeilinger, A.V. Sergienko, Y.H. Shih, “New high-intensity source of polarization-entangled photon pairs,” *Phys. Rev. Lett.* **75**, 4337-4341 (1995).
- [21] A. Degiron, H.J. Lezec, W.L. Barnes & T.W. Ebbesen, “Effects of hole depth on enhanced light transmission through subwavelength hole arrays,” *Appl. Phys. Lett.* **81**, 4327-4329 (2002).
- [22] We have here chosen to define  $\hat{\omega} = \omega + i\Delta\omega$  as a complex frequency, and  $k_{sp}$  as a purely real quantity, to simplify notation. We could equally well have taken the reverse choice, because both amount to the same thing: damping of the SPs as they propagate along the metal-dielectric interface.
- [23] E.D. Palik, *Handbook of Optical Constants of Solids I* (Academic Press, SanDiego, 1985).
- [24] P.B. Johnson and R.W. Christy, “Optical Constants of the Noble Metals,” *Phys. Rev. B* **6**, 4370-4379 (1972).
- [25] K. L. van der Molen, F. B. Segerink, N. F. van Hulst and L. Kuipers, “Influence of hole size on the extraordinary transmission through subwavelength hole arrays,” *Appl. Phys. Lett.* **85**, 4316-4318 (2004).
- [26] C. Ropers, D.J. Park, G. Stibenz, G. Steinmeyer, J. Kim, D.S. Kim, C. Lienau, “Femtosecond light transmission and subradiant damping in plasmonic crystals,” *Phys. Rev. Lett.* **94**, 113901 (2005).
- [27] M. Born & E. Wolf. *Principles of Optics* (Pergamon, Oxford, 1980).
- [28] N. Bloembergen, “Nonlinear optics and spectroscopy,” *Rev. Mod. Phys.* **54**, 685-695 (1982).
- [29] C. Kurtsiefer, M. Oberparleiter, and H. Weinfurter, “High-efficiency entangled photon pair collection in type-II parametric fluorescence,” *Phys. Rev. A* **64**, 023802 [4 pages] (2001).
- [30] M.H. Rubin, D.N. Klyshko, Y.H. Shih, and A.V. Sergienko, “Theory of two-photon entanglement in type-II optical parametric down-conversion,” *Phys. Rev. A* **50**, 5122-5133 (1994).

- [31] M. Atatüre, A. V. Sergienko, B.E.A. Saleh, and M.C. Teich, “Dispersion-Independent High-Visibility Quantum Interference in Ultrafast Parametric Down-Conversion,” *Phys. Rev. Lett.* **84**, 618-621 (2000).
- [32] M.H. Rubin, “Transverse correlation in optical spontaneous parametric down-conversion,” *Phys. Rev. A* **54**, 5349-5360 (1996).
- [33] B.E.A. Saleh, A. Joobeur, and M.C. Teich, “Spatial effects in two- and four-beam interference of partially entangled biphotons,” *Phys. Rev. A* **57**, 3991-4003 (1998).
- [34] Some authors define the biphoton-amplitude function as  $A(\vec{r}_1, t_1; \vec{r}_2, t_2)$  [30]. This near-field form of the biphoton amplitude function  $A$  is simply related to our far-field definition through a Fourier transform.
- [35] W.K. Wootters, “Entanglement of Formation of an Arbitrary State of Two Qubits,” *Phys. Rev. Lett.* **80**, 2245-2248 (1998).
- [36] J.S. Bell, “On the Einstein-Podolsky-Rosen Paradox,” *Physics* **1**, 195-200, (1964).
- [37] J.F. Clauser and M.A. Horne, “Experimental consequences of objective local theories,” *Phys. Rev. D* **10**, 526-535 (1974).
- [38] A. Garuccio and V.A. Rapisarda, “Bell inequalities and the four-coincidence experiment,” *Nuovo Cimento Soc. Ital. Fis., A* **65**, 269-297 (1981).
- [39] In the first equality, the visibilities  $V_{0^\circ}$  and  $V_{45^\circ}$  are now slightly redefined as the “average” over  $0^\circ$  and  $90^\circ$ , and  $45^\circ$  and  $-45^\circ$ , respectively, as in Chapter 10. For instance,  $V_{0^\circ, \text{avg}} = [R_{\max}(0^\circ) - R_{\min}(0^\circ) + R_{\max}(90^\circ) - R_{\min}(90^\circ)] / [R_{\max}(0^\circ) + R_{\min}(0^\circ) + R_{\max}(90^\circ) + R_{\min}(90^\circ)]$ , where the setting of the first polarizer is indicated only.
- [40] The effective bandwidth of the two filters  $T_1$  and  $T_2$  used for this measurement was slightly smaller at 3 nm, because their central transmission wavelength was shifted by roughly 1 nm with respect to the double pump wavelength, which narrows  $\mathcal{T}(\delta\omega_1) \equiv T_1(\Omega + \delta\omega_1)T_2(\Omega - \delta\omega_1)$ . Note, that these filters were later replaced by more correctly centered ones.
- [41] V.G. Dmitriev, G.G. Gurzadyan and D.N. Nikogosyan, *Handbook of nonlinear crystals; Springer Series in Optical Sciences Vol. 64* (Springer-Verlag, Berlin, 1991).
- [42] P.S.K. Lee, M.P. van Exter, J.P. Woerdman, “Increased polarization-entangled photon flux via thinner crystals,” *Phys. Rev. A* **70**, 043818 (2004) [4 pages].
- [43] D.M. Greenberger, M.A. Horne & A. Zeilinger, “Multiparticle interferometry and the superposition principle,” *Physics Today*, 22-29 (August 1993).
- [44] D. Bouwmeester, J.W. Pan, K. Mattle, M. Eibl, H. Weinfurter & A. Zeilinger, “Experimental quantum teleportation,” *Nature* **390**, 575-579 (1997).
- [45] D.E. Grupp, H.J. Lezec, T.W. Ebbesen, K.M. Pellerin & T. Thio, “Crucial role of metal surface in enhanced transmission through subwavelength apertures,” *Appl. Phys. Lett.* **77**, 1569-1571 (2000).
- [46] B. Hecht, H. Bielefeldt, L. Novotny, Y. Inouye & D.W. Pohl, “Local excitation, scattering, and interference of surface plasmons,” *Phys. Rev. Lett.* **77**, 1889-1892 (1996).
- [47] C. Sönnichsen, A.C. Duch, G. Steininger, M. Koch, G. von Plessen, J. Feldmann, “Launching surface plasmons into nanoholes in metal films,” *Appl. Phys. Lett.* **77**, 140-142 (2000).
- [48] C. Kurtsiefer, M. Oberparleiter & H. Weinfurter, “High efficiency entangled photon pair collection in type II parametric fluorescence,” *Phys. Rev. A* **64**, 023802 (2001) [4 pages].

## Bibliography

- [49] J.F. Clauser, M.A. Horne, A. Shimony & R.A. Holt, "Proposed experiment to test local hidden-variable theories," *Phys. Rev. Lett.* **23**, 880-884 (1969).
- [50] L.D. Landau, E.M. Lifshitz & L.P. Pitaevskii, *Electrodynamics of Continuous Media*, (Pergamon, Oxford, 1984, 2nd edition).
- [51] Y.J. Lu & Z.Y. Ou, "Observation of nonclassical photon statistics due to quantum interference," *Phys. Rev. Lett.* **88**, 023601 (2002) [4 pages].
- [52] H.J. Kimble, M. Dagenais & L. Mandel, "Photon antibunching in resonance fluorescence," *Phys. Rev. Lett.* **39**, 691-695 (1977).
- [53] M. Sarrazin, J.-P. Vigneron & J.-M. Vigoureux, "Role of Wood anomalies in optical properties of thin metallic films with a bidimensional array of subwavelength holes," *Phys. Rev. B* **67**, 085415 (2003) [8 pages].
- [54] G.D. Monteath, *Applications of the Electromagnetic Reciprocity Principle* (Pergamon, Oxford, 1973).
- [55] H.A. Macleod, *Thin-film Optical Filters* (Hilger, London, 1969), p. 24.
- [56] L. Salomon, F. Grillot, A.V. Zayats & F. de Fornel, "Near-field distribution of optical transmission of periodic subwavelength holes in a metal film," *Phys. Rev. Lett.* **86**, 1110-1113 (2001).
- [57] P. Dawson, B.A.F. Puygranier & J-P. Goudonnet, "Surface plasmon polariton propagation length: a direct comparison using photon scanning tunneling microscopy and attenuated total reflection," *Phys. Rev. B* **63**, 205410 (2001) [10 pages].
- [58] F.I. Baida, D. van Labeke, A. Bouhelier, T. Huser & D. W. Pohl, "Propagation and diffraction of locally excited surface plasmons," *J. Opt. Soc. Am. A* **18**, 1552-1561 (2001).
- [59] H.J. Lezec, A. Degiron, E. Devaux, R.A. Linke, L. Martin-Moreno, F.J. Garcia-Vidal & T.W. Ebbesen, "Beaming light from a subwavelength aperture," *Science* **297**, 820-822 (2002).
- [60] H. Ditlbacher, J.R. Krenn, G. Schider, A. Leitner, F.R. Aussenegg, "Two-dimensional optics with surface plasmon polaritons," *Appl. Phys. Lett.* **81**, 1762-1764 (2002).
- [61] D.S. Kim, S. C. Hohng, V. Malyarchuk, Y. C. Yoon, Y. H. Ahn, K. J. Yee, J. W. Park, J. Kim, Q. H. Park, C. Lienau, "Microscopic origin of surface-plasmon radiation in plasmonic band-gap nanostructures," *Phys. Rev. Lett.* **91**, 143901 (2003).
- [62] K.A. Tetz, R. Rokitski, M. Nezhad, Y. Fainman, "Excitation and direct imaging of surface plasmon polariton modes in a two-dimensional grating," *Appl. Phys. Lett.* **86**, 111110 (2005) [3 pages].
- [63] C. Genet, M.P. van Exter and J.P. Woerdman, "Huygens description of resonance phenomena in subwavelength hole arrays," *J. Opt. Soc. Am. A* **22**, 998-1002.
- [64] D. Egorov, B.S. Dennis, G. Blumberg, M.I. Haftel, "Two-dimensional control of surface plasmons and directional beaming from arrays of subwavelength apertures," *Phys. Rev. B* **70**, 033404 (2004) [4 pages].
- [65] Note, that our gold film is much thicker than the one used in Ref. [62] and, unlike theirs, is surely optically thick while still thin compared to the optical wavelength.
- [66] J. Elliott, I.I. Smolyaninov, N.I. Zheludev, A.V. Zayats, "Polarization control of optical transmission of a periodic array of elliptical nanoholes in a metal film," *Opt. Lett.* **29**, 1414-1416 (2004).

- [67] R. Gordon, A.G. Brolo, A. McKinnon, A. Rajora, B. Leathem, K.L. Kavanagh, “Strong polarization in the optical transmission through elliptical nanohole arrays,” *Phys. Rev. Lett.* **92**, 037401 (2004). Unfortunately, the authors employ the word depolarization in an improper way, using it to describe a change of a spatially-*uniform* SOP into another spatially *uniform* SOP.
- [68] R.M.A. Azzam and N.M. Bashara, *Ellipsometry and Polarized Light* (North-Holland, Amsterdam, 1987).
- [69] F. Le Roy-Brehonnet and B. Le Jeune, “Utilization of Mueller matrix formalism to obtain optical targets depolarization and polarization properties,” *Prog. Quant. Electr.* **21**, 109-151 (1997).
- [70] C. Genet, E. Altewischer, M.P. van Exter, and J.P. Woerdman, “Optical depolarization induced by arrays of subwavelength metal holes,” *Phys. Rev. B* **71**, 033409 (2005) [4 pages]. **20**, 1927-1931 (2003).
- [71] T. Thio, H.F. Ghaemi, H.J. Lezec, P.A. Wolff, T.W. Ebbesen, “Surface-plasmon-enhanced transmission through hole arrays in Cr films,” *J. Opt. Soc. Am. B* **16**, 1743-1748 (1999).
- [72] M. Sarrazin, J.P. Vigneron, “Polarization effects in metallic films perforated with a bidimensional array of subwavelength rectangular holes,” *Opt. Comm.* **240**, 89-97 (2004).
- [73] Here, “transverse” is used to indicate the direction orthogonal to the array surface normal.
- [74] The imaginary part of  $B$  vanishes for any integration region which is mirror symmetric in the origin.
- [75] E. Moreno, F.J. Garcia-Vidal, D. Erni, J.I. Cirac, L. Martin-Moreno, “Theory of Plasmon-Assisted Transmission of Entangled Photons,” *Phys. Rev. Lett.* **92**, 236801 (2004).
- [76] D.N. Klyshko, *Photons and Non Linear Optics* (Gordon and Breach, New York, 1980).
- [77] D.N. Klyshko, D. N. Klyshko, “Effect of focusing on photon correlation in parametric light scattering,” *Zh. Eksp. Teor. Fiz.* **94**, 82-90 (1988), [*Sov. Phys. JETP* **67**, 1131-1135 (1988)].

## *Bibliography*

---

## List of publications

---

- *Experimental observation of wave chaos in a conventional optical resonator*, J. Dingjan, E. Altewischer, M.P. van Exter, and J.P. Woerdman, Phys. Rev. Lett. **88**, 064101 (2002).
- *Plasmon-assisted transmission of entangled photons*, E. Altewischer, M.P. van Exter, and J.P. Woerdman, Nature **418**, 304-306 (2002).
- *Polarization analysis of propagating surface plasmons in a subwavelength hole array*, E. Altewischer, M.P. van Exter, and J.P. Woerdman, JOSA B **20**, 1927-1931 (2003).
- *Nonreciprocal reflection of a subwavelength hole array*, E. Altewischer, M.P. van Exter, and J.P. Woerdman, Opt. Lett. **28**, 1906-1908 (2003).
- *Polarization tomography of metallic nanohole arrays*, E. Altewischer, C. Genet, M.P. van Exter, J.P. Woerdman, P.F.A. Alkemade, A. van Zuuk, and E.W.J.M. van der Drift, Opt. Lett. **30**, 90-92 (2005).
- *Optical depolarization induced by arrays of subwavelength metal holes*, C. Genet, E. Altewischer, M.P. van Exter, and J.P. Woerdman, Phys. Rev. B **71**, 033409 (2005).
- *Analytical model of optical depolarization in square and hexagonal nanohole arrays*, E. Altewischer, M.P. van Exter and J.P. Woerdman, J. Opt. Soc. Am. B **22**, 1731-1736 (2005).
- *Quantum decoherence versus classical depolarization in nanohole arrays*, E. Altewischer, M.P. van Exter and J.P. Woerdman, accepted for publication in Phys. Rev. A.
- *Fano-type interference in the point-spread function of nanohole arrays*, E. Altewischer, X. Ma, M.P. van Exter and J.P. Woerdman, accepted for publication in Opt. Lett.

List of publications



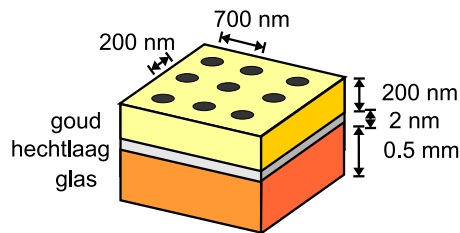
### Licht als golfverschijnsel

In de meeste situaties die we in het dagelijks leven tegenkomen kan licht worden beschouwd als een golfverschijnsel, vergelijkbaar met golven in water. Een belangrijke eigenschap van golven is de golflengte. Bij watergolven, bijvoorbeeld aan het oppervlak van de zee, is de golflengte zichtbaar als de afstand tussen de toppen van twee naastgelegen golfjes (typisch loopt deze van een paar cm tot tientallen m). De golflengte van licht bepaalt welke kleur het licht heeft. Blauw licht heeft een kleine golflengte ( $0.4\ \mu\text{m}$ ) en rood licht een grotere ( $0.6$  tot  $0.8\ \mu\text{m}$ ; ter vergelijking, de dikte van een haar is ongeveer  $50\ \mu\text{m}$ ).

Een andere belangrijke eigenschap van het soort golven waartoe licht behoort (de zogenaamde transversale golven) is de polarisatie. Dit is de richting waarin de golf op en neer gaat en deze staat voor transversale golven altijd loodrecht op de richting waarin de golf beweegt. Voor golven aan het oppervlak van de zee is de polarisatierichting de verticale richting, want het water beweegt omhoog en omlaag terwijl de golf zich voortbeweegt langs het wateroppervlak naar het strand toe. Bij licht kan de polarisatie in alle richtingen loodrecht op de voortbewegingsrichting staan. Door gebruik te maken van materialen die geen licht doorlaten als de polarisatie langs een specifieke richting staat, kunnen we laten zien dat licht inderdaad gepolariseerd kan zijn. Als we een stukje van dit "polariserend" materiaal, of "polarisator", in een bundel gepolariseerd licht zetten en het vervolgens draaien om een as parallel aan de lichtbundel, zien we bij een bepaalde stand van de polarisator het licht erachter volkomen uitdoven; We hebben daarmee de polarisatierichting van het licht bepaald. Van dit licht-uitdovende effect van polarisatoren wordt gebruik gemaakt in polaroid zonnebrillen, waarin polariserend materiaal verwerkt is zodanig dat de schittering van zonlicht (in water bijvoorbeeld) weggehaald wordt; deze schitteringen bestaan namelijk altijd uit licht dat voorname-lijk langs het aardoppervlak (horizontaal) gepolariseerd is, terwijl de rest van het licht niet deze "voorkeurspolarisatie" heeft.

In de optica, de tak van de natuurkunde die licht bestudeert, is bekend dat er "problemen" optreden als voorwerpen kleiner worden dan de golflengte van licht. Een voorbeeld is dat

## Samenvatting



**Figuur 1:** Een dwarsdoorsnede van een “gatenrooster”: een patroon van zeer kleine gaatjes in een dunne metaallaag. De afmetingen en materialen van de gatenroosters die door ons zijn bestudeerd zijn in de figuur aangegeven.

zulke kleine voorwerpen niet meer scherp waargenomen kunnen worden met gewone optische microscopen; er moeten daarvoor in de plaats andersoortige microscopen (electronen microscopen) gebruikt worden. Een ander voorbeeld is dat er nauwelijks meer licht door een gaatje komt als de diameter van dat gaatje klein is ten opzichte van de golflengte van het licht. Van dit laatste effect wordt handig gebruik gemaakt in magnetrons, waar de doorzichtige magnetrondeur bedekt wordt door een electrisch-geleidend gaas van vierkante gaatjes. Het “licht” (zogenaamde microgolven, niet zichtbaar) waarmee de gerechten binnen in de oven worden opgewarmd heeft een te grote golflengte (tot zelfs enkele cm) en komt niet door de gaatjes heen, zodat je veilig voor de magnetron kunt staan. Daarentegen heeft het licht van het lampje binnenin een veel kleinere golflengte en komt wel door de deur heen, zodat je toch de gerechten in de magnetron van buitenaf door de deur kunt zien.

## **Rasterpatronen van zeer kleine gaatjes in metaallaagjes**

In 1998 ontdekte Thomas Ebbesen dat als je patronen van kleine gaatjes in een dunne laag metaal maakt, zoals geschetst in Figuur 1, er (bij bepaalde kleuren) veel meer licht doorheen komt dan je zou kunnen verwachten op basis van het magnetrongeval. In sommige gevallen komt er zelfs meer licht doorheen dan er direct op de gaatjes valt. De verklaring hiervoor is dat het metaal zelf een actieve rol speelt bij het doorlaten van licht: het werkt als een soort “gootsteen” waarbij het licht dat op het metaal valt langs het metaaloppervlak stroomt en zo door de gaatjes gestuwd wordt. Het licht dat als het ware “gevangen” is op het metaaloppervlak heeft net iets andere eigenschappen dan het licht dat in de vrije ruimte (de lucht) beweegt, en heeft daarom een speciale naam gekregen: oppervlakteplasmon. Deze naam geeft aan dat om een *oppervlaktegolf* gaat, die zich voortbeweegt langs het grensvlak van een diëlectricum (bijvoorbeeld lucht) en een metaal, en dat deze gekoppeld is aan een ladingsgolf in het *electronenplasma* (elektrisch geladen gas) in het metaal.

In de Hoofdstukken 2 en 5 tot en met 9 van dit proefschrift bestuderen we de optische eigenschappen van gatenroosters en de rol van oppervlakteplasmonen hierin. We beschrijven hierin onder andere twee methoden om gatenroosters te maken en een aantal methoden om de eigenschappen van gatenroosters te meten. Door te kijken naar hoe verschillende gatenroosters de polarisatie van invallend licht veranderen als het er aan de andere kant weer uitkomt, kunnen we het aandeel van de oppervlakteplasmonen in de optische eigenschappen van de gatenroosters vergelijken met de bijdrage van de gaten zelf.

## Licht als deeltjesverschijnsel

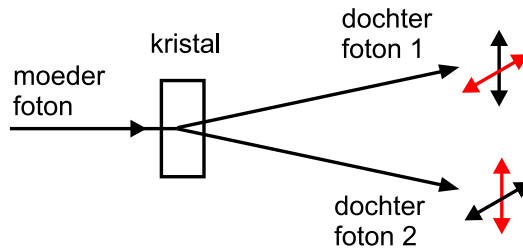
Als licht heel erg zwak is kunnen we het niet meer goed beschrijven met het hierboven besproken golfbeeld. Als we namelijk proberen dit zwakke licht te detecteren zullen we merken dat we steeds “pulsjes” waarnemen en niet langer een continu op en neer golvende energiestroom. De genoemde pulsjes zijn kleine pakketjes energie, waarvan de energie-inhoud enkel afhangt van de golflengte en die enkel als geheel kunnen worden waargenomen (ze kunnen niet gesplitst worden in nog kleinere pakketjes). Het is alsof de detector deeltjes invangt, net zoals een “tennisballen telmachine” die elke keer als hij een tennisbal invangt een tellertje met 1 verhoogt. Vandaar dat de genoemde energiepakketjes ook wel lichtdeeltjes of fotonen worden genoemd. De natuurkundige theorie die deze deeltjes beschrijft heet de “quantummechanica” (quantum is Latijn voor hoeveelheid en wordt hier gebruikt om het energiepakketje aan te duiden).

## Quantumverstrengeling en quantumcomputers

Een speciale voorspelling die de quantummechanica doet is het bestaan van “verstrengeling” van de eigenschappen van twee deeltjes. Door deze verstrengeling is het mogelijk om te weten wat een bepaalde eigenschap is van het ene deeltje door slechts aan het *andere* deeltje een meting van dezelfde eigenschap te verrichten. Dus zonder aan het eerste deeltje iets te meten weet je meteen zijn eigenschappen, en dit onafhankelijk van de afstand tussen de twee deeltjes! Dit was door Albert Einstein reden om bezwaar te hebben tegen de quantummechanica; hij noemde de beïnvloeding van de eigenschappen van het tweede deeltje door meting aan het eerste deeltje “spookachtige beïnvloeding op afstand”. Niettemin is in de laatste 25 jaar in een aantal verschillende experimenten aangetoond dat deze verstrengeling wel degelijk bestaat.

Een gevolg van het bestaan van verstrengeling is dat het mogelijk is, in ieder geval in theorie, om een computer te maken die met behulp van verstrengelde systemen volgens een quantummechanische rekenmethode kan rekenen. Deze zogenaamde “quantumcomputer” zou voor bepaalde toepassingen, onder andere het breken van codes (cryptografie), veel sneller kunnen zijn dan de huidige computers. Er zijn al demonstratie-experimenten geweest waarin met kleine getallen (een paar bits) gerekend is volgens de quantummethode. Voor het maken van een echte quantumcomputer, waarin gewerkt zou kunnen worden met grote getallen, is het waarschijnlijk nodig om verstrengelde systemen in een vaste stof te maken, zoals de halfgeleider materialen waarvan de chips in de huidige computers gemaakt worden. Op dit moment zijn die vaste stof systemen er nog niet of nauwelijks, en wordt voor een groot deel gebruik gemaakt van licht (fotonen) als drager van verstrengeling. Een groot voordeel van licht is dat het ideaal is om over grote afstanden informatie mee te versturen. Het is echter niet mogelijk om quantumberekeningen alleen met licht te doen, daarvoor is (ook) materie nodig.

Een veelgebruikte methode om verstrengelde fotonen te maken is de zogenaamde “spontaneous parametric downconversion”; deze methode bestuderen we in Hoofdstuk 3. In deze methode wordt een speciaal kristal gebruikt dat in staat is om een invallend “moederfoton” op te splitsen in twee “dochterfotonen”, zoals geschetst in Figuur 2. De dochterfotonen zijn



**Figuur 2:** Het principe achter “spontaneous parametric downconversion”: een moederfoton wordt gesplitst in twee dochterfotonen in een speciaal kristal (een zogenaamd niet-lineair kristal). De twee fotonen zijn verstrengeld met betrekking tot hun polarisatie. Eén mogelijke polarisatie van de fotonen wordt aangegeven door de lichte pijltjes, een andere door de donkere (rechts); de polarisaties van de twee fotonen staan in beide gevallen loodrecht op elkaar.

verstrengeld in polarisatie, voor de juiste combinatie van hun golflengtes en voortbewegings-richtingen. Deze polarisatieverstrengeling houdt in dat de polarisatie van een enkel foton elke richting kan hebben, deze richting is volledig onbepaald, maar dat de polarisaties van de twee fotonen wel altijd loodrecht op elkaar staan.

## Quantumverstrengeling en oppervlakteplasmonen

Wij hebben onderzocht of het mogelijk is om oppervlakteplasmonen te gebruiken als dragers van verstrengeling. Als dit zo zou zijn, dan zijn oppervlakteplasmonen mogelijk te gebruiken in een quantumcomputer. Het voordeel van oppervlakteplasmonen boven fotonen in dit opzicht is dat de oppervlakteplasmonen in het metaal “gevangen” zijn en zo een stap in de richting van een vaste-stof quantumcomputerchip vertegenwoordigen.

Om te onderzoeken hoe oppervlakteplasmonen de verstrengeling tussen fotonen beïnvloeden hebben we de hierboven besproken gatenroosters gezet in het pad van één foton uit een paar verstrengelde fotonen, en gekeken of de verstrengeling behouden bleef achter het gatenrooster. De resultaten hiervan zijn dat verstrengeling enkel behouden is onder bepaalde condities: als het niet mogelijk is om op de een of andere manier informatie te halen over de polarisatie van de invallende fotonen uit de bewegingsrichtingen van de oppervlakteplasmonen op het gatenrooster, dan is de verstrengeling volledig behouden. Zou je hiertoe echter wel in staat zijn *in principe*, zonder dat je dit daadwerkelijk hoeft te meten (!), dan gaat de verstrengeling (gedeeltelijk) verloren. Deze resultaten zijn uiteengezet in Hoofdstuk 4 en een theoretische verklaring voor het gevonden gedrag wordt gegeven in Hoofdstuk 10, waarbij de link wordt gelegd met de metingen van de optische eigenschappen van gatenroosters van Hoofdstukken 6 en 8.

---

## Curriculum vitæ

---

Erwin Altewischer werd op 5 april 1975 geboren in Leiden. In 1993 behaalde hij zijn VWO diploma op het Agnes College in dezelfde plaats. Na een jaar Klassiek Piano gestudeerd te hebben aan het Koninklijk Conservatorium te Den Haag, en vervolgens twee jaar Muziekwetenschappen aan de Universiteit Utrecht (Propedeuse 1995), besloot hij Natuurkunde te gaan studeren in Leiden. Tijdens zijn studie werkte hij driekwart jaar als vervangend docent Natuurkunde op het Aquino College te Leiden. In 2001 haalde hij zijn doctoraal (cum laude), met als afstudeerproject golf-chaos in optische resonatoren gebaseerd op standaard optische elementen, onder leiding van dr. M. P. van Exter en prof. dr. J. P. Woerdman.

Inmiddels geënthousiasmeerd van het natuurkundig onderzoek, trad Erwin in 2001 in dienst van de Stichting Fundamenteel Onderzoek der Materie (FOM) als onderzoeker in opleiding, om onderzoek te verrichten in de groep ‘Quantum Optics & Quantum Information’, weer onder leiding van van Exter en Woerdman. Het onderwerp betrof de verstrengeling van de polarisatievrijheidsgraden van fotonen en plasmonen, alsmede de optische eigenschappen van dunne metaallagen met daarin roosters van gaten met diameters kleiner dan de golflengte van licht. Dit proefschrift bevat de resultaten van dit onderzoek.

Curriculum vitæ

---

## Nawoord

---

Dit proefschrift zou niet compleet zijn, zonder een woord van dank voor een aantal mensen die bij de vervaardiging ervan onmisbaar zijn geweest. Met betrekking tot het Fijnmechanische gedeelte van het experiment waren dat met name Koos Benning en Ewie de Kuiper, die een groot aantal houders voor allerhande optiek vervaardigden en altijd beschikbaar waren voor vakkundig advies. Het elektronische gedeelte was in de zeer capabele handen van Arno van Amersfoort, René Overgaw en Leendert Prevo, die ook menig probleem op computergebied wisten te verhelpen. Administratieve en allerhande andere zaken waren altijd toevertrouwd aan Anneke Aschoff, Henriëtte van Leeuwen en Daniëlle van Raaij. Tot ons verdriet ontviel Anneke ons in het laatste jaar van mijn promotie, veel te vroeg.

Al gedurende mijn eerste jaar, en tot het eind van mijn promotie, kon ik beschikken over de assistentie van een aantal studenten gedurende hun stages, te weten Kasper Brink, Sylvio Koller, Yung-Chin Oei en Xiaosong Ma, die met hun aanwezigheid en hulp het experimentele werk verlichtten.

Natuurlijk kan ik niet mijn collega's overslaan die ervoor zorgden dat ik steeds weer opnieuw met plezier op het lab kwam: naast de wetenschappelijke staf, de promovendi Steven van de Berg, Yngve Lien, Hayk Haroutyunyan, Jos Dingjan, Sumant Oemrawsingh, Jorrit Visser, Javier Loaiza, Thijs Klaassen, Peter Lee, Nikolay Kuzmin, Graciana Puentes en Eduard Driessen, en de post-docs Sergio Dutra, Andrea Aiello, Cyriaque Genet en Dirk Voigt.

Kleurrijk werd mijn werktijd (en daarnaast mijn vrije tijd natuurlijk) ook door mijn vrienden, teveel om hier op te noemen. En tenslotte, was ook de onvoorwaardelijke steun van mijn broer Werner en mijn ouders voor mij onmisbaar.

